



AFRL-RX-WP-TR-2019-0013

**MICROSTRUCTURE-BASED SIMULATIONS TO
IDENTIFY FAILURE MECHANISMS IN ADDITIVELY
MANUFACTURED METALLIC COMPONENTS**

Matthew R. Begley

University of California, Santa Barbara

02 DECEMBER 2018

Final Report

**DISTRIBUTION STATEMENT A. Approved for public release:
Distribution is unlimited.**

**AIR FORCE RESEARCH LABORATORY
MATERIALS AND MANUFACTURING DIRECTORATE
WRIGHT-PATTERSON AIR FORCE BASE, OH 45433-7750
AIR FORCE MATERIEL COMMAND
UNITED STATES AIR FORCE**

NOTICE AND SIGNATURE PAGE

Using Government drawings, specifications, or other data included in this document for any purpose other than Government procurement does not in any way obligate the U.S. Government. The fact that the Government formulated or supplied the drawings, specifications, or other data does not license the holder or any other person or corporation; or convey any rights or permission to manufacture, use, or sell any patented invention that may relate to them.

This report is the result of contracted fundamental research deemed exempt from public affairs security and policy review in accordance with SAF/AQR memorandum dated 10 Dec 08 and AFRL/CA policy clarification memorandum dated 16 Jan 09. This report is available to the general public, including foreign nationals. Copies may be obtained from the Defense Technical Information Center (DTIC) (<http://www.dtic.mil>)

AFRL-RX-WP-TR-2019-0013 HAS BEEN REVIEWED AND IS APPROVED FOR PUBLICATION IN ACCORDANCE WITH ASSIGNED DISTRIBUTION STATEMENT.

//SIGNATURE//
WILLIAM MUSINSKI
Work Unit Manager
Materials Branch
Structural Materials Division

//SIGNATURE//
DANIEL EVANS
Branch Chief
Materials Branch
Structural Materials Division

//SIGNATURE//
AMBER DAVIS
Deputy Division Chief
Structural Materials Division
Materials and Manufacturing Directorate

This report is published in the interest of scientific and technical information exchange, and its publication does not constitute the Government's approval or disapproval of its ideas or findings.

REPORT DOCUMENTATION PAGE

Form Approved
OMB No. 0704-0188

The public reporting burden for this collection of information is estimated to average 1 hour per response, including the time for reviewing instructions, searching existing data sources, gathering and maintaining the data needed, and completing and reviewing the collection of information. Send comments regarding this burden estimate or any other aspect of this collection of information, including suggestions for reducing this burden, to Department of Defense, Washington Headquarters Services, Directorate for Information Operations and Reports (0704-0188), 1215 Jefferson Davis Highway, Suite 1204, Arlington, VA 22202-4302. Respondents should be aware that notwithstanding any other provision of law, no person shall be subject to any penalty for failing to comply with a collection of information if it does not display a currently valid OMB control number. **PLEASE DO NOT RETURN YOUR FORM TO THE ABOVE ADDRESS.**

1. REPORT DATE (DD-MM-YY) 02 December 2018			2. REPORT TYPE Final			3. DATES COVERED (From - To) 02 November 2015– 02 November 2018		
4. TITLE AND SUBTITLE MICROSTRUCTURE-BASED SIMULATIONS TO IDENTIFY FAILURE MECHANISMS IN ADDITIVELY MANUFACTURED METALLIC COMPONENTS					5a. CONTRACT NUMBER FA8650-16-1-5232			
					5b. GRANT NUMBER			
					5c. PROGRAM ELEMENT NUMBER 63112F			
6. AUTHOR(S) Matthew Begley					5d. PROJECT NUMBER 3946			
					5e. TASK NUMBER			
					5f. WORK UNIT NUMBER X13S			
7. PERFORMING ORGANIZATION NAME(S) AND ADDRESS(ES) University Of California, Santa Barbara Office Of Research 3227 Cheadle Hall Santa Barbara CA 93106-0001					8. PERFORMING ORGANIZATION REPORT NUMBER			
9. SPONSORING/MONITORING AGENCY NAME(S) AND ADDRESS(ES) Air Force Research Laboratory Materials and Manufacturing Directorate Wright-Patterson Air Force Base, OH 45433-7750 Air Force Materiel Command United States Air Force					10. SPONSORING/MONITORING AGENCY ACRONYM(S) AFRL/RXCM			
					11. SPONSORING/MONITORING AGENCY REPORT NUMBER(S) AFRL-RX-WP-TR-2019-0013			
12. DISTRIBUTION/AVAILABILITY STATEMENT DISTRIBUTION STATEMENT A. Approved for public release: Distribution is unlimited.								
13. SUPPLEMENTARY NOTES Report contains color.								
14. ABSTRACT (Maximum 200 words) A combined experimental- and simulation-based approach for electron beam melted Ti-6Al-4V strut-based structures was used to identify printing-related features that impact response and to develop highly-efficient, low-dimension models that can incorporate such features. Testing and modelling were completed for sub-elements of a complex lattice (“primitives”), consisting of struts, strut intersections (or ‘nodes’) and cells consisting of multiple nodes. Mechanical testing and characterization illustrated that strut size, shape and mechanical response depend on the orientation of the strut relative to the build direction. Testing of node primitives and cells revealed that the truss structures were generally more compliant and weaker than expected from elementary truss models; conversely, they exhibit greater load-carrying capacity beyond peak loads. Beam-based models were adapted to account for the plastic localization near defects and within nodes by using additional beam elements. Fully resolved two-dimensional FEA of strut intersections illustrated that the transition from node yielding to widespread strut yielding is controlled by the spread of plastic zones across the node. This behavior can be captured using beam elements that form a ‘box’ whose corners connect to strut axes. Fully resolved 2D FEA and beam-based models were used to represent structures with multiple nodes and defects.								
15. SUBJECT TERMS Electron beam melted, Ti-6Al-4V, additive manufacturing, lattice structures, finite element analysis, mechanical properties								
16. SECURITY CLASSIFICATION OF:			17. LIMITATION OF ABSTRACT: SAR	18. NUMBER OF PAGES 83	19a. NAME OF RESPONSIBLE PERSON (Monitor) William Musinski 19b. TELEPHONE NUMBER (Include Area Code) (937) 255-0485			
a. REPORT Unclassified	b. ABSTRACT Unclassified	c. THIS PAGE Unclassified						

Table of Contents

LIST OF FIGURES	iii
LIST OF TABLES	x
1. SUMMARY.....	1
2. MOTIVATION AND PROGRAM RATIONALE	3
3. SPECIMEN DESIGN AND FABRICATION	8
4. MECHANICAL TESTING.....	10
4.1 Methods.....	10
4.2 Results & Discussion.....	11
4.2.1 Struts	11
4.2.2 Node Specimens.....	14
4.2.3 Cell Primitives.....	16
5. CHARACTERIZATION.....	19
5.1 Methods.....	19
5.2 Results & Discussion.....	19
5.3 Key Outcomes	30
6. ANALYTICAL MODELS OF STRUT COLLAPSE.....	31
6.1 Overview	31
6.2 Method.....	32
6.3 Results & Discussion.....	33
6.3 Key Outcomes	38
7. FEA SIMULATIONS OF PRIMITIVES USING CONVENTIONAL BEAM ELEMENTS... ..	39
7.1 Overview	39
7.2 Methods.....	39
7.3 Results & Discussion.....	41
7.4 Key Outcomes	44
8. FEA SIMULATIONS OF SURFACE DEFECTS IN STRUTS.....	45
8.1 Overview	45
8.2 Methods.....	46
8.3 Results & Discussion.....	46

8.4 Key Outcomes	51
9. FEA SIMULATIONS OF STRUT INTERSECTIONS (NODES).....	52
9.1 Overview	52
9.2 Methods.....	52
9.3 Results & Discussion.....	53
9.4 Key Outcomes	62
10. COMBINED NODE AND DEFECT SIMULATIONS	63
10.1 Overview	63
10.2 Methods.....	63
10.3 Results & Discussion.....	64
10.4 Key Outcomes	65
11. SUMMARY AND FUTURE WORK.....	66
11.1 Summary	66
11.2 Future Work.....	67
12. REFERENCES	68
LIST OF SYMBOLS, ABBREVIATIONS, AND ACRONYMS	70

LIST OF FIGURES

<u>Figure</u>	<u>Page</u>
Figure 1. Stiffness and strength as a function of relative density for EBM printed Ti-64 lattices, taken from the literature [1-3]; the results illustrate that the response of such lattices is significantly below that expected from cellular materials theory, principally due to the difference between nominal and actual strut dimensions and significant material contained in the intersections between struts, or nodes.	3
Figure 2. Microstructures in thin walled structures created powder-bed fusion (3D printing), taken from the literature [5-6]; the results illustrate the challenges in predicting mechanical response, since component geometry and material structure are intertwined, leading to shape-specific and size-specific material response that must be included in simulations.	4
Figure 3. Conceptual overview of an ICME framework for developing 3D-printed components; in order to assess component designs, information from the printing process and resulting defect structure must be incorporated into simulations to separate extrinsic performance limiters (e.g. topology and dimensions) from intrinsic limiters such as printing defects and material heterogeneity.	5
Figure 4. Overview of the UCSB program, which focused on developing simulations of component response that provide facile integration of printing related features. The program included both characterization of EBM printed Ti64 and reduced order simulations design to avoid the complexity and expense associated with fully three-dimensional models of lattice materials.	6
Figure 5. Primitive specimens of the program: the testing and characterization focused on those on the left (struts, 60 degree node B, cell B), including tension testing of struts, and compression testing of multi-strut structures; the structures on the right were printed at the same time and present opportunities for future testing of the simulations developed in this program.	8
Figure 6. Build layout of the primitive specimens shown in Figure 4; all structures were printed on an Arcam A series machine with a 70um build layer. Following printing, the specimens were hot isostatic pressed to completely remove internal voids.	9
Figure 7. A summary of the specimens, print orientation and strut diameters that were tested in the program indicating the number of tests in terms of the total number of specimens; the green boxes represent instances where more than five additional tests can be conducted, while the orange boxes represent specimens for which fewer than five original samples remain.	10
Figure 8. Load-displacement curves from the tensile tests conducted on struts of different diameter, printed at different orientations relative to the build direction. Note the strong orientation dependence of the peak loads, and for 1mm diameter struts, the elastic stiffness. The size-dependence is weaker in larger struts, but still present.....	12

<u>Figure</u>	<u>Page</u>
Figure 9. Peak load normalized to the nominal area and the average area given a print orientation based on CT scans (see later figures). The tails indicate the maximum and minimum peak stress for a given print orientation while the boxes display the average peak stress with bounds of one standard deviation above and below. Results are shown for struts with nominal diameter of (a) 1 mm and (b) 1.25 mm.	13
Figure 10. Optical images of Node B specimens deformed under uniaxial compression, tested in two different orientations, illustrating that multiple deformation modes are possible from identical specimens. A variety of platen conditions was considered. The pink lines illustrate the laser interferometry used to measure specimen compression.	14
Figure 11. (a) Schematics depicting Node B the two print directions, 0° and 90°, as-printed (P) and the two testing orientations (T), 0° and 90°, after samples were cut with EDM. (b) Load-displacement curves of compression tests on the nodes for 0° and 90° print orientations in both testing orientations for nodes with a nominal diameter of 1 mm. (c) Load-displacement curves of compression tests on the nodes for 0° and 90° print orientations in both testing orientations for nodes with a nominal diameter of 1.25 mm. 15	15
Figure 12. a) Optical images of the deformation modes Cell B specimens, with “bend”, “straight”, and “kink” schematics overlaid to display strut behavior. Load displacement curves of compression tests of the cell with results separated by deformation mode for cells with struts with a nominal diameter of (b) 1 mm and (c) 1.25 mm. Note that the cell with thicker struts exhibited no kink deformation mode.	17
Figure 13. Scanning electron micrographs of the as-printed strut surfaces at various levels of magnification, show hierarchical surface roughness; the deep crevices seen at high magnification are all surface-connected; 3D tri-beam sectioning of the specimens reveal submicron porosity, a result of the HIP post-processing step.	20
Figure 14. Composite optical micrographs of 1 mm diameter struts after polishing, illustrating the strong orientation dependence of both surface roughness and strut size; geometric deviations from nominal geometry explain part of the orientation-dependence, but even accounting for these differences, orientation-dependence remains. (See Figure 9.) 20	20
Figure 15. EBSD characterization of polished strut cross-sections oriented so that the 001 direction is in line (such as those shown in Figure 15), illustrating complex microstructures that depend on orientation. Note the build direction relative to the EBSD plane is indicated by the schematics below the figures.	21
Figure 16. CT scans of Cell B and Node B specimens; the Cell B image shows clear variations in strut geometry with orientation relative to the build direction (vertical in this picture). Full movies of the scans are available in the supplemental information. These scans were post-processed to analyze statistical variations in strut cross-section as a function of build orientation.	22
Figure 17. 2D slices from the 3D CT dataset for Node B, showing variations in strut cross-section along their length.	23

Figure	Page
Figure 18. 2D slices from the 3D CT dataset for Cell B, showing variations in strut cross-section along their length.	23
Figure 19. Plots of (a) area normalized to nominal area and (b) aspect ratio of inscribed ellipses for all struts in nodes and (c) normalized area and (d) aspect ratio of inscribed ellipses fit to individual struts within a print orientation in cells. Tails display the average maximum and minimum of within a print orientation while boxes display one average standard deviation above and below the average of the average value.	25
Figure 20. Autocorrelation functions for diameter as a function of location along a strut, which provides a measure of the size variability in the struts, and the characteristic length-scale between peaks and valleys.	27
Figure 21. Persistence length for surface features indicating the distance over which variations in strut diameter are correlated; the results clearly demonstrate that struts oriented with the build direction have stronger variations in strut diameter, as indicated in Fig.15	28
Figure 22. (a) CT reconstruction of a print defect near a node from a cell with a nominal strut diameter of 1 mm. (b) CT reconstruction of a strut from the same sample with two print defects shown. Note that the lines on the CT image are voxels from the CT reconstruction and not print layers.	29
Figure 23. Conceptual overview of defect modeling with beam elements; the presence of a surface defect is modeled using an elastic-plastic beam element that forms a plastic skin at the notch; theoretical relationships for the moment/force vs. curvature/stretch relationship of the notch were derived and used to map out response.	32
Figure 24. Structural yielding map showing combinations of stretch and curvature that lead to complete yielding of a beam element (without variations along its length, i.e. in a short notch). This can be used to identify limit loads and moments near notches. The notch height and width factors into the scaling of the defect element dimensions.	33
Figure 25. Contours of constant force (left) and moment (right) for compression loading of a notched struts, illustrating peak resultants than can be sustained once complete yielding has occurred. Complete analytical models were generated to predict resultants as a function of imposed strain. Note that the triangular regions of the bottom corners in the left and right figures correspond to the plastic collapse region indicated in red in the center figure.	34
Figure 26. Force-stretch and moment-curvature responses for the notch defect element, assuming constant curvature (for stretch loading) or constant stretch (for moment loading). The curves illustrate the complex yielding behavior that results from combinations of stretch and bending. On the left, cases are shown with constant normalized curvatures of 0,0.25, 0.5,0.7 (traversing from blue to red); on the right, cases are shown with constant normalized stretch of 0, 0.25, 0.5, 0.75 (traversing from blue to red).	35

<u>Figure</u>	<u>Page</u>
Figure 27. Force-stretch and moment-curvature responses for the notch defect element, assuming that curvature and stretch deformation are imposed at fixed ratio. The curves illustrate the complex yielding behavior that results from combinations of stretch and bending, include post-yielding (softening) induced by axial deformation in the presence of bending. Values of α are 0, 0.5, 1.0 and 1.5 (traversing from blue to red).....	36
Figure 28. Contour map of the size of the plastic zone under stretching and bending deformation, with corresponding yield map on the right. The results indicate that the notch defects will go fully plastic for imposed deformation just outside the elastic limit.	37
Figure 29. Force-stretch relationship with proportional curvature imposed, illustrating the size of the plastic zone at various combinations of stretch and bending. For sufficiently high curvatures imposed with stretch, bending initiates and drives the size of the plastic zone on either side of the notch.	37
Figure 30. Moment-curvature relationship with proportional stretch imposed, illustrating the size of the plastic zone at various combinations of stretch and bending. For sufficiently high stretch with imposed bending, stretching initiates and drives the size of the plastic zone on either side of the notch.	38
Figure 31. Schematic overview of modeling strategy using conventional beam elements; the nodes connecting struts are essentially rigid, such that the simulation preserves angles between struts. Essentially, on the struts themselves can yield and contribute to softening behavior.....	40
Figure 32. A comparison of tests and modeling with conventional beam elements with nominal dimensions, for nodes subjected to various end/platen conditions and cages subjected to frictionless platens. The FEA consistently overestimates the stiffness and peak load of the structure, due to the fact it does not account for plasticity in the nodes connecting the ends of the struts.	41
Figure 33. A comparison of simulations with conventional beam elements with nominal dimensions (1.25 mm diameter struts) with various end conditions and various hardening rules; the results demonstrate that no amount of hardening or lack of constraint (due to platen sliding) can account for the discrepancies shown in Figure 32.	42
Figure 34. Effect of strut dimensions on predictions, with experiments: Load displacement curves from a FEA beam model compression test of a node as compared to the experimental results with nominal strut diameter of (a) 1 mm and (b) 1.25 mm. The solid line indicates the results using a cross-sectional area based on the nominal diameter while the shaded region has bounds using the maximum and minimum cross-sectional areas of inscribed ellipses based on the CT scan shown in Fig. 2b. The dashed line indicates the result using the average cross-sectional area of an inscribed ellipse from the CT scan. Similar results are shown for a FEA beam model of a cell compression test shown with nominal strut diameter of (c) 1 mm and (d) 1.25 mm.....	43

<u>Figure</u>	<u>Page</u>
Figure 35. Schematic overview of the modeling of defects in struts; a notched strut is analyzed under compression and end rotation (in various combinations), using both 2D plane stress FEA (fully resolving behavior near the defect) and a beam element approach that reduces the net section of the strut at the location of the defect. Localized plastic deformation in the reduced section is an approximation to the plastic zone that develops in the notch... 45	45
Figure 36. Effect of notch dimensions on the compression/rotation response of a strut with a defect, for full 2D FEA to model the defect. The notch depth dominates the results, with notch width having little impact on the response in this range of widths, which correspond to sharp notches consistent with micrographs of surface defect. Plane strain calculations are somewhat stiffer than plane stress, owing to the additional constraint of zero out-of-plane straining. 47	47
Figure 37. A comparison of 2D FEA (fully resolved plastic zone at the notch) and beam element approach to modeling surface defects; resultant loads and moments are extracted from both models. The beam element results are a fair approximation to the global force displacement response of the strut with a defect. Complex moment responses are a function of whether or not the next section yields in compression prior to rotation. Defect is loaded at the center of the strut. 48	48
Figure 38. A map of notch closure as a function of end displacement and end rotation; for a given notch depth, combinations above the boundary indicate that the strut will bend to open the notch, while those below indicate that compression of the strut closes the notch prior to significant bending deformation (that would otherwise open the notch)..... 49	49
Figure 39. A comparison of full 2D FEA with beam element defect approach, for equal amounts of compression and rotation and several different notch depths. Generally, the beam element defect approach tracks the trends of the full FEA across a range of defect sizes, with larger discrepancies at larger defect sizes. Defect is located at the center of the strut. 50	50
Figure 40. A comparison of full 2D FEA with beam element defect approach, for differing amounts of compression and rotation. Generally, the beam element defect approach tracks the trends of the full FEA across a range of proportional loadings, with larger differences once the net section near the defect has gone fully plastic. 50	50
Figure 41. A comparison of full 2D FEA with beam element defect approach, for purely proportional loading (equal amounts of end rotation and compression), across a range of defect locations (relative to the end of the strut) and defect depths. The beam element approach does an excellent job of capturing the behavior regardless of notch depth and defect location. 51	51
Figure 42. Schematic illustration of Node B specimens in two different orientations, used to study the effect of yielding at the node (strut intersections). Both 2D FEA (plane stress) and beam element approaches were studied to determine effective means to capture nodal deformations without resulting to full FEA. 53	53

<u>Figure</u>	<u>Page</u>
Figure 43. Full 2D FEA predictions of the load-displacement response for Node B in compression, showing the evolution of plastic zones at the ends of the struts and in the center node. Yielding of the node section controls the peak load in the structure.	54
Figure 44. Full 2D FEA predictions of the load-displacement response for Node B in compression rotated 90 degrees from Figure 43, showing the evolution of plastic zones at the ends of the struts and in the center node. Yielding of the node section controls the peak load in the structure. Note that the deformed shape is virtually identical to one of the images shown in Figure 10.	54
Figure 45. Full 2D FEA predictions of the evolution of plastic zones at the ends of the struts and in the center node. Yielding of the node section controls the peak load in the structure. Note that the deformed shape is virtually identical to one of the images shown in Figure 10.	55
Figure 46. Full 2D FEA predictions of evolution of plastic zones at the ends of the struts and in the center node. Yielding of the node section controls the peak load in the structure. Note that the deformed shape is virtually identical to one of the images shown in Figure 10..	55
Figure 47. A comparison of the predicted deformed shape with plastic zones illustrated and the experiments on Node B, rotated configuration.	56
Figure 48. A comparison of the predicted load-compression curve from full 2D FEA (using nominal dimensions) and the corresponding experiments.	57
Figure 49. The beam box concept for modeling nodes, wherein additional beam elements with dimensions that match the node are added to the connections between the strut elements. The dimensions of the beam box elements (representing the node) can be defined with asymmetry, which leads to strut rotations such as those shown in Figure 10.	58
Figure 50. A comparison of beam box simulations (to capture nodal deformation) with full 2D FEA, showing the effect of asymmetry and elevated strain hardening (SH) in the beam elements used to represent the node. The elevated strain hardening is motivated by the fact that the node sees elevated strain hardening due to a strain concentration, which cannot be captured by the beam elements with one-dimensional geometry.	59
Figure 51. Conceptual diagram motivating the calibration used to specify strain hardening in beam box elements; the full 2D plane stress calculation is used to estimate the maximum strain in the nodes (due to the strain concentration); elevated hardening is prescribed in the beam box that will produce the same stress elevation at the strain level observed in the beam box.	60
Figure 52. A comparison of “best fit” between the beam box concept and full 2D FEA, wherein the hardening properties of the beam box elements are adjusted to maximize agreement; the black dashed line indicates the 2D FEA result while the grey dashed line shows the result of beam box with no adjustments. The yellow line is the best fit, while the blue line uses the calibration concept described in the text.	60

<u>Figure</u>	<u>Page</u>
Figure 53. A comparison of calibrated beam box predictions and full 2D FEA for nodes with different strut angles and different boundary conditions; the calibration is the theoretical calibration developed from the 60 degree nodes.	61
Figure 54. A comparison of full 2D FEA simulations and beam element simulations, with edge defects (at 30% depth) in the struts placed at position A and/or B. These simulations demonstrate that strut defects without plasticity in the nodes (i.e. no nodal beam box) does not produce accurate results.	63
Figure 55. A comparison of full 2D plane stress FEA simulations and beam element simulations, for a defect at position A.....	64
Figure 56. A comparison of full 2D plane stress FEA simulations and beam element simulations, with numerous edge defects placed at positions A and B.....	65

LIST OF TABLES

<u>Table</u>	<u>Page</u>
Table 1. Strut peak load and stiffness	18
Table 2. Node peak load and stiffness	18
Table 3. Cell peak load and stiffness	18

1. SUMMARY

Additive manufacturing is an attractive pathway to producing truss-based cellular structures (commonly referred to as lattices) with high specific stiffness, strength and energy absorption. Powder bed fusion via electron beam melting is advantageous for such applications, as it is capable of producing features with high aspect ratio and low residual stress. A central challenge in the design and fabrication of such structures is understanding and predicting the impact of printing-related features, such as deviations in truss geometry and surface defects that arise as a natural consequence of the powder-bed fusion process. This coupling creates a critical need to develop efficient simulation tools to predict the impact of printing-related features, which can be used to speed the design process by identifying critical defects or robust cellular topologies.

This program addressed this critical need for electron beam melted (EBM) Ti-6Al-4V strut-based structures, through a combination of experiments and simulations, with the integrated goals of (i) identification of printing-related features that impact response, and (ii) the development of highly efficient, low dimension models that can incorporate such features while avoiding the need for expensive, time-consuming fully three-dimensional modeling of struts and their intersections. The strategy was to test and model sub-elements of a complex lattice, or ‘primitives’, consisting of struts, strut intersections (or ‘nodes’) and cells consisting of multiple nodes. The underlying hypothesis was that one-dimensional beam elements can be adapted to account for deviations from nominal geometry and deformation within nodes; these adaptations would be calibrated using the primitive experiments to account for variations in strut size and strength, surface defects, etc. that result from the EBM process.

The mechanical testing and characterization thrusts of this program illustrate that strut size, shape and mechanical response depend on the orientation of the strut relative to the build direction. The fact that adjustments to nominal geometry are insufficient to eliminate the orientation-dependence of measured strength suggests that the microstructure is orientation-dependent. Therefore, this is a critical component of future work. The scope of this program is limited to hot isostatically pressed (HIP'd) structures, which exhibited essentially no internal defects, but significant surface-connected defects that serve as nucleation site for localized plasticity. In the context of struts subjected to stretching and bending, these plastic zones grow quickly with small load increments above the elastic limit, and span the entire cross-section of the strut. Plastic zones that span the entire cross-section are commonly referred to as ‘plastic hinges’, which strongly limit the response of the structure. Testing of node primitives (i.e. four struts intersecting to form a single node) and cells (consisting of multiple struts and nodes) revealed that the truss structures were generally more compliant and weaker than expected from elementary truss models; conversely, they exhibit greater load-carrying capacity beyond peak loads. These differences are a consequence of plastic localization within nodes (i.e. strut intersections) and at surface defects, as established by a comparison of experiments and finite element simulations.

The simulations developed in this program illustrate that beam-based models can be adapted to account for these plastic localization near defects and within nodes by using additional beam elements. For surface defects, the adaptation is to use a beam-based ‘defect’ elements with reduced area that are offset to account for the axial eccentricity created by the defect; a

comparison of fully-resolved 2D plane stress simulations and those utilizing ‘defect elements’ illustrates the latter accurately captures the (force/moment)-(stretch/curvature) response of struts with defects. For larger lattices involving numerous struts, this enables far more rapid predictions of global response than fully-resolved 3D finite elements filling the entire structure. The simulations illustrate that suitably adapted beam-based models are effective because plastic localization near defects is highly localized; plastic zones span the net section in the thickness direction and only a fraction of strut diameter in the axial direction. Hence, a single ‘defect’ beam element is sufficient to capture the loss of bending and stretching stiffness associated with plastic collapse controlled by defects.

With respect to plasticity within nodes, fully resolved two-dimensional finite element analysis (FEA) of strut intersections illustrate that the transition from node yielding to widespread strut yielding is controlled by the spread of plastic zones across the node. This behavior can be captured using beam elements that form a ‘box’ whose corners connect to strut axes; elements in the box yield preferentially prior to strut yielding (when appropriate) and capture the loss of constraint associated with node yielding. The simulations indicate that the beam-box approach should be calibrated to account for the enhanced hardening that arises within nodes due to the strain concentration at the strut intersection. This program has identified appropriate, straightforward calibrations, and demonstrated their efficacy for a wide range of strut intersection angles. Further, using a combination of fully resolved 2D FEA and beam-based models with both nodal adjustments and surface defects, the approach was shown to be effective in structures with multiple nodes and defects.

Future work should focus on demonstrations that the beam-based simulations are effective for three-dimensional structures, and target the identification of instances where orientation- or location-specific material structure must be incorporated into beam properties. Toward that end, characterization of spatial variations of internal microstructure is critically needed.

2. MOTIVATION AND PROGRAM RATIONALE

Additive manufacturing of truss-based cellular structures (or “lattices”) holds significant promise for the development of components with high specific stiffness and strength. Powder-bed fusion via electron beam melting (EBM) is an attractive method for printing such structures, due to its ability to fabricate struts or cell walls with large aspect ratios and low residual stress. Early studies of such lattices [1-3] have illustrated that their mechanical response is inferior compared to that anticipated via conventional models of cellular materials [4], as shown in **Figure 1**. Printed lattices exhibit lower stiffness and strengths than expected, across a broad range of topologies and relative densities. The discrepancy between expectation and performance is most significant at low relative density, where struts cross-sections are small relative to the cell size. For most components, cell size is limited by component dimensions to be on the order of centimeters (e.g. to provide multiple cells across a component that is tens of centimeters in dimension), implying millimeter-scale struts.

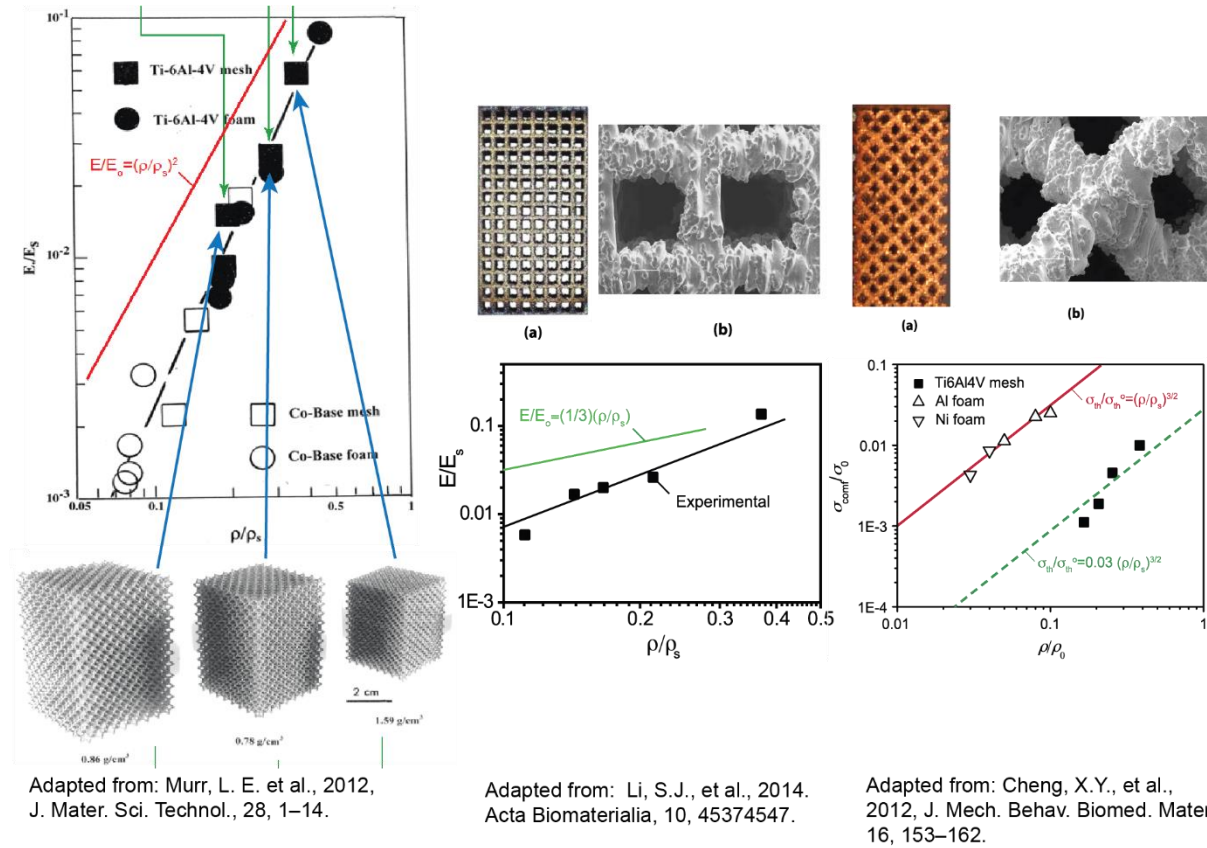


Figure 1. Stiffness and strength as a function of relative density for EBM printed Ti-64 lattices, taken from the literature [1-3]; the results illustrate that the response of such lattices is significantly below that expected from cellular materials theory, principally due to the difference between nominal and actual strut dimensions and significant material contained in the intersections between struts, or nodes.

In turn, this implies that struts (or cell walls) will have thickness that is on the order of typical melt pool dimensions, and perhaps only an order of magnitude bigger than the powder size. This

interaction between physical length-scales suggests that strut dimensions and material structure will be, in many instances, inseparable from processing parameters (such as raster scheme, power, beam speed, etc.) and component geometry. For struts on the order of millimeters, melt pools, solidification and subsequent thermal history will be a function of strut orientation. The implications of this are shown in **Figure 2**, which illustrates grain structure in printed thin walled components taken from literature [5]; here, ‘thin walled’ refers to walls with thickness that is within an order of magnitude of the melt pool size, and typically only several times bigger. In this regime, grain size, shape and distribution are shown to be a function of wall thickness, and orientation, as are surface features or “defects”. While manipulation of build parameters to control such features are effective in larger scale features [6], such methods typically rely on controlling heat transfer over multiple build layers and away from raster edges. As such, they are likely not feasible for thin walled components, i.e. struts and cell walls required to build cellular structures.

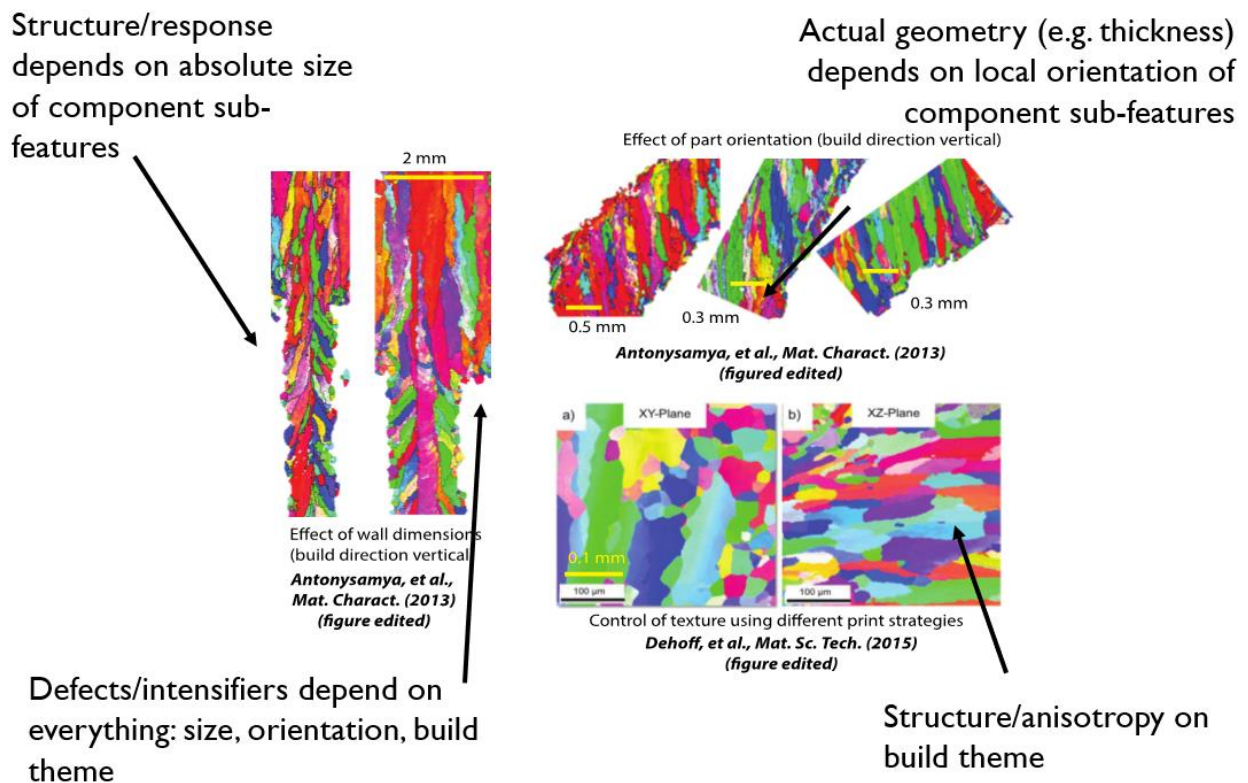


Figure 2. Microstructures in thin walled structures created powder-bed fusion (3D printing), taken from the literature [5-6]; the results illustrate the challenges in predicting mechanical response, since component geometry and material structure are intertwined, leading to shape-specific and size-specific material response that must be included in simulations.

A new framework for the design and development of printed cellular materials is therefore needed, one that establishes quantitative links between processing parameters and component geometry as shown in **Figure 3**. Candidate geometries must be integrated with process-design; in-situ monitoring of the printing process would provide quantitative information about discrepancies between prescribed and printed features, including defects. This information,

include orientation-specific properties, must be utilized in simulation tools to evaluate component performance. In some instances, the component geometry (i.e. cellular topology) can be altered to achieve performance (i.e. extrinsic performance limiters). In others, the process will need to be modified to control structure and defects (i.e. intrinsic performance limiters).

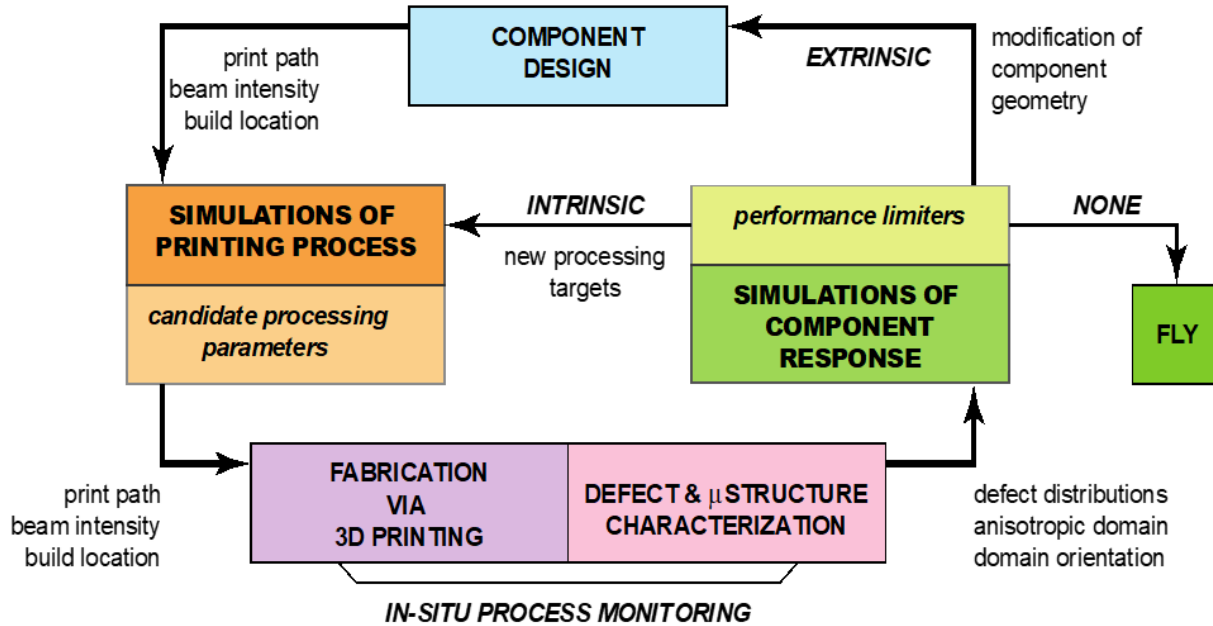


Figure 3. Conceptual overview of an ICME framework for developing 3D-printed components; in order to assess component designs, information from the printing process and resulting defect structure must be incorporated into simulations to separate extrinsic performance limiters (e.g. topology and dimensions) from intrinsic limiters such as printing defects and material heterogeneity.

Simulations capable of identifying the underlying features controlling performance are a critical component of this integrated computational materials engineering (ICME) framework. These simulations need to be highly efficient (to evaluate the implications of various cellular design choices) and capable of handling printing related properties.

This program focuses on the development of simulation frameworks that address these needs, as shown in **Figure 4**. There are two central objectives. First, what features of printed thin-walled or strut-based structures most strongly influence performance? This includes surface features, material structure and their dependence on strut orientation and geometry (i.e. strut intersections). Second, what are efficient computational frameworks that can integrate such features to anticipate component response? In this regard, fully 3D rendering of the structure for conventional continuum finite elements is arguably a non-starter. First, the complex geometry requires highly expensive computations that will dramatically extend design cycles. Second, even if computationally feasible, such rendering requires idealizations of complex geometry near strut intersections that may or may not influence response. The proposed program adapts an alternative approach: the development of models based on beam elements that are adapted to account for the influence of plasticity in nodal connections and the presence of surface defects.

Such simulations are orders of magnitude faster than full 3D rendering, and side-step the need to digitally render the complex geometry of strut intersections.

What are the intrinsic performance limiters in printed lattices?

- Surface roughness
- Strut intersections
- Material anisotropy
- Rastering domains

What are *feasible* simulations for integrated component-process design?

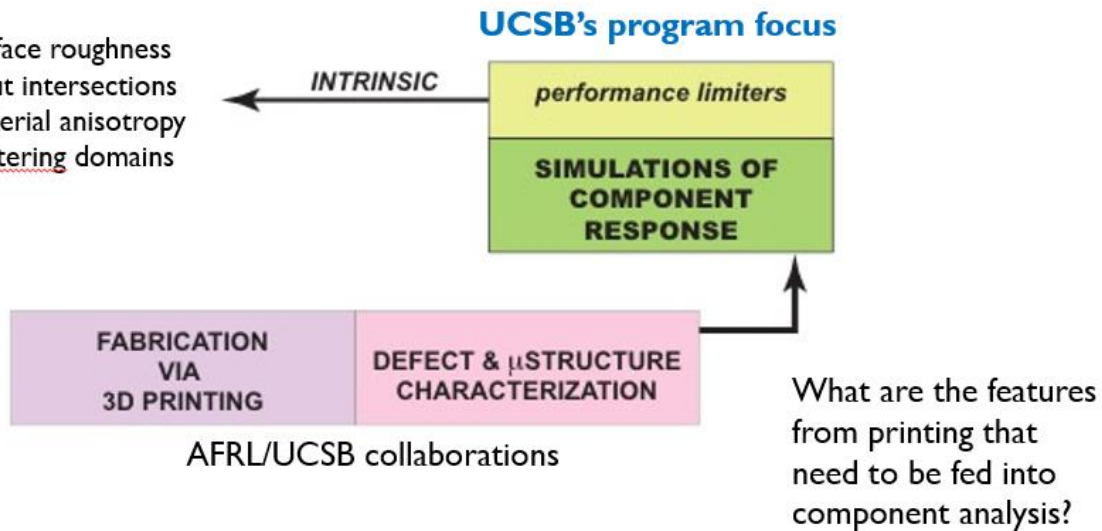


Figure 4. Overview of the UCSB program, which focused on developing simulations of component response that provide facile integration of printing related features. The program included both characterization of EBM printed Ti64 and reduced order simulations design to avoid the complexity and expense associated with fully three-dimensional models of lattice materials.

The proposed program addresses the development of simulation frameworks (based on beam elements) that are adapted to account for the influence of plasticity in nodal connections and the presence of surface defects. Naturally, when developing idealized models (i.e. those that reduce the complexity of geometry), one drawback is the need to calibrate the lower-order approximation. This must be accepted as the downside of obtaining dramatic reductions in the time required to evaluate candidate designs. (The results of this program illustrate that model calibrations may be straightforward, and are arguably comparable to inevitable calibrations of approximations to 3D geometry needed for fully rendered 3D FEA.)

The strategy of the program is based on the hypothesis that the response of large-scale cellular structures can be simulated using beam-based elements and built into a hierarchical framework of struts and “nodes” representing strut intersections. This hierarchical framework assumes that the response of each of these features can be validated using “primitives”, specimens which represent sub-elements of a large-scale cellular structure. That is, with effective beam representations of struts, and a new beam-based representation of nodes, the response of more complex structures can be accurately predicted at a fraction of the cost of full-scale 3D simulations. To test this underlying hypothesis, mechanical testing and characterization of printed primitives was conducted to identify orientation-specific mechanical properties, defects

and material structure. Beam-based simulations were then conducted to evaluate their efficacy in capturing the behavior of primitives.

A central goal of the program was to identify deformation mechanisms in the primitives and the role of defects. To limit the complexity of model calibration, two-dimensional plane stress analysis of primitives was used as a proxy for “fully rendered” solutions. By tuning beam-based models to this baseline, one avoids purely empirical calibrations by using experiments that include a myriad of printing features, including build-specific defect distributions. Such printing related features can ultimately be included in future beam-based approaches, once the foundational understanding of the impact of plasticity in struts, nodes and near surface defects is established.

3. SPECIMEN DESIGN AND FABRICATION

Specimens consisting of isolated struts, nodes formed by the intersection of multiple struts, and cells consisting of multiple nodes, as shown in **Figure 5**, were fabricated in Ti-6Al-4V by an EBM system (Arcam A Series, Arcam, Sweden) using a 70 μm build layer. All samples were hot isostatically pressed (HIP) upon fabrication, per ASTS F2924-14 or ASTM F3001-14: “process components under inert atmosphere at not less than 100 MPa within the range 895 to 955°C; hold at the selected temperature within $\pm 15^\circ\text{C}$ for 180 ± 60 min, and cool under inert atmosphere to below 425°C.”

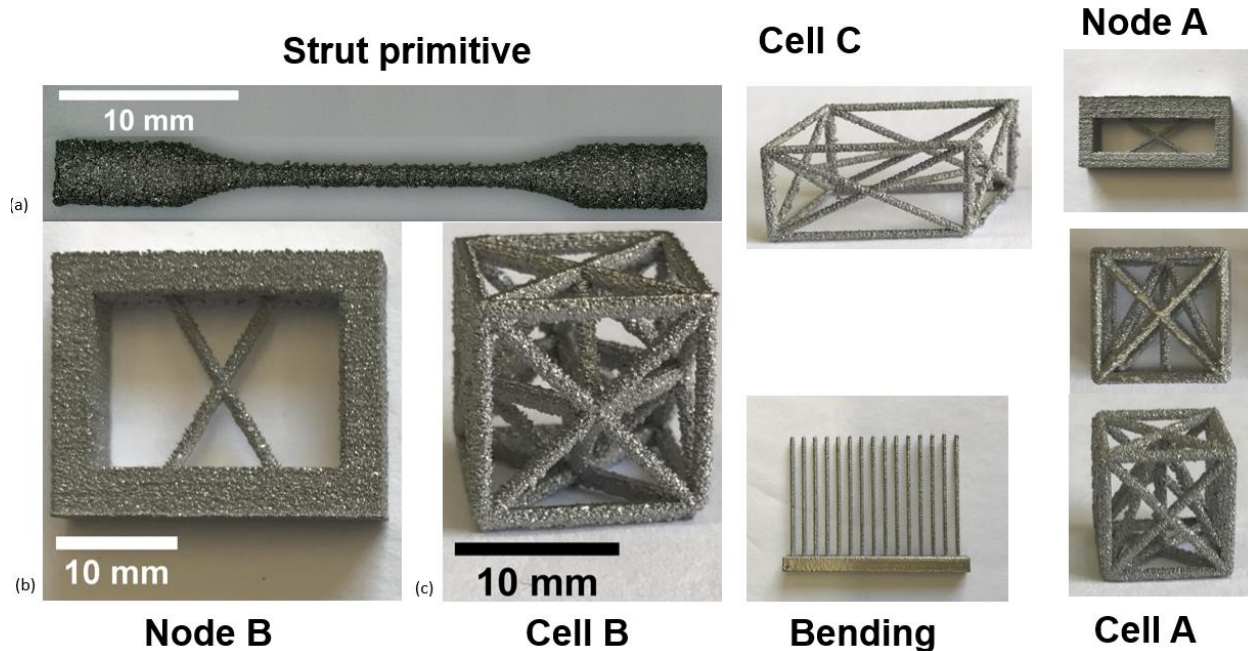
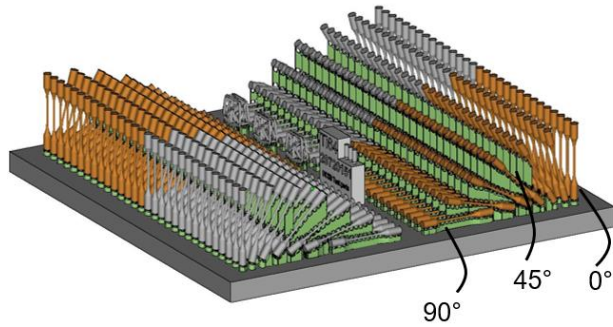


Figure 5. Primitive specimens of the program: the testing and characterization focused on those on the left (struts, 60 degree node B, cell B), including tension testing of struts, and compression testing of multi-strut structures; the structures on the right were printed at the same time and present opportunities for future testing of the simulations developed in this program.

There are two nominal strut diameters in all of the samples — 1 mm and 1.25 mm. Struts were printed at three different orientations relative to the build direction (0° , 45° , and 90°), with a minimum sample size of eight per orientation for each nominal strut diameter; **Figure 6** shows the build layout used to print all specimens. Nodes were printed at two print orientations, 0° and 90° from the build direction, with a sample size of eight per orientation for each nominal strut diameter. Cells were all printed at the same orientation, with a minimum sample size of eleven for each nominal strut diameter.



Tensile sample build plate layout
 70 micron theme, Arcam A series machine
 All samples examined post-HIP

Cell build plate layout
 70 micron theme, Arcam A series machine
 All samples examined post-HIP

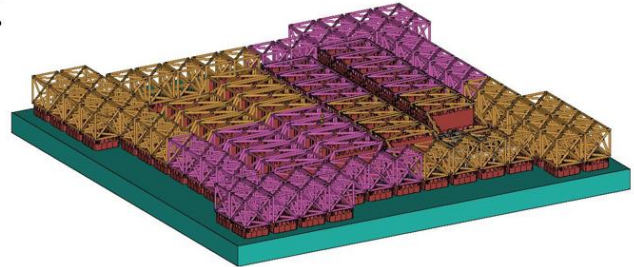


Figure 6. Build layout of the primitive specimens shown in Figure 4; all structures were printed on an Arcam A series machine with a 70um build layer. Following printing, the specimens were hot isostatic pressed to completely remove internal voids.

4. MECHANICAL TESTING

4.1 Methods

Figure 7 provides a summary of the tests on the specimens from the build layout shown in **Figure 6** completed for this program. The fractions listed in the table reflect the number of specimens tested over the total number available. Mechanical testing was done on a Material Test System 810 servo hydraulic load frame at room temperature under a displacement rate of 0.1 mm/min.

Apr-18		1 mm, HIPped						
		Print orientation						
		0	15	30	45	60	75	90
Tension	13/15	0/15	0/15	14/15	0/15	0/15	11/15	
Node A	0/25			0/25			0/25	
Node B	8/25			0/25			8/25	
Bending	0/30			0/15			0/30	
Cell A	1/15							
Cell B	15/15							
Cell C	0/15						0/15	

		1.25 mm, HIPped						
		Print orientation						
		0	15	30	45	60	75	90
Tension	10/15	0/15	0/15	12/15	0/15	0/15	13/15	
Node A	7/25			0/25			0/25	
Node B	18/25			0/25			8/25	
Bending	0/30			0/15			0/30	
Cell A	14/15							
Cell B	14/15							
Cell C	0/15						0/15	

		Legend						
			N/A, not printed					
			none tested yet					
			5 or more samples left					
			less than 5 samples left					

Figure 7. A summary of the specimens, print orientation and strut diameters that were tested in the program indicating the number of tests in terms of the total number of specimens; the green boxes represent instances where more than five additional tests can be conducted, while the orange boxes represent specimens for which fewer than five original samples remain.

Struts were tested in tension in custom-built stainless steel grips; initially, a laser extensometer with reflective tape in the gage section was used to measure strains in the cross section. However, inconsistent results obtained after post-processing indicated that the tape likely moved during testing, presumably due to a lack of adherence with the rough as-printed surfaces. Hence, grip displacements are used to report load-displacement behaviors in the struts.

The frames of the node A and B were cut via electrical discharge machining (EDM) in two different configurations, which removed the vertical support walls so that the load could be transferred through the struts during compression; i.e., the side walls **Figure 5** were removed with only the top, horizontal frame left in place. This produced a high angle "X" specimen from the node B specimen and a low angle "X" specimen from the node A specimen. The pre-cut node specimens were then compressed between two 4140 hardened steel platens with three different boundary conditions.

Several boundary conditions along the top and bottom of the node specimens were tested. “Rigid” refers to scenarios where the remaining thick, horizontal piece of the frame at the top of the specimen of the node specimen was epoxied to the hardened steel plates; this increased the contact area between the frame and the platens and prevented out of plane rotation. “Free rotation” refers to scenarios where the frame was simply taped to the steel platens; the tape does not create a significant constraint and hence allowed for out-of-plane rotations during compression. “Sliding” refers to scenarios where the top thick frame (running horizontally in **Figure 5**) was cut to allow for individual motion of the nodal struts; the remaining frame of the specimen was covered with Teflon tape, allowing for horizontal sliding of the struts into a splayed configuration.

Cell or “cage” specimens were tested in compression between hardened steel platens with Teflon tape at the interface between the specimen and the hardened steel platens. Several unloading cycles were included in all tests (prior to the onset of peak load, i.e. at small displacements) to determine stiffness via the unloading response. For compression testing of cage specimens, the specimens were loaded until at least one strut failed (and in some instances, loaded until several struts had failed); after the first strut failure, the test was stopped by unloading to zero load.

4.2 Results & Discussion

4.2.1 Struts

Figure 8 shows the resultant load-displacement curves from tensile tests of the strut primitives; the average peak load and average stiffness of the struts for a given print orientation are listed in **Table 1** (appearing later in **Figure 13**). As print orientation (angle between build direction and tensile axis) increases, average peak load and average stiffness increase, as shown in **Figure 9**. To estimate the peak stress from the peak loads seen in **Figure 8**, consideration was given to geometric variations based on print orientation from the CT scans fully described in the next section. Briefly, the stress was computed by calculating the area of ellipses fit to the cross-sections from the CT scans, where the fit is defined by the largest ellipse that contacts solid material at every point. (This corresponds to the biggest ellipse that can be fit within a solid section). Consequently, this computed stress, which uses a lower bound estimate for cross-sectional area that carries load, is a reasonable estimate for the upper bound for load capacity of the struts.

It should be emphasized that the CT scans were performed on two cage specimens, not the tested struts themselves. (This was a consequence of CT scans becoming available midway through the program.) However, the statistics of the strut geometry obtained from various specimens (e.g. struts, nodes and cages) were virtually indistinguishable. I.e., the average, standard deviation, maximum and minimum values of geometric parameters characterizing strut geometry were identical for the two cages. Furthermore, the parameters obtained for the node B specimen were identical when the orientation of the struts is identical. Hence, there is significant confidence that the parameters describing strut geometry are representative of the build and do not vary significantly from one geometry to the next.

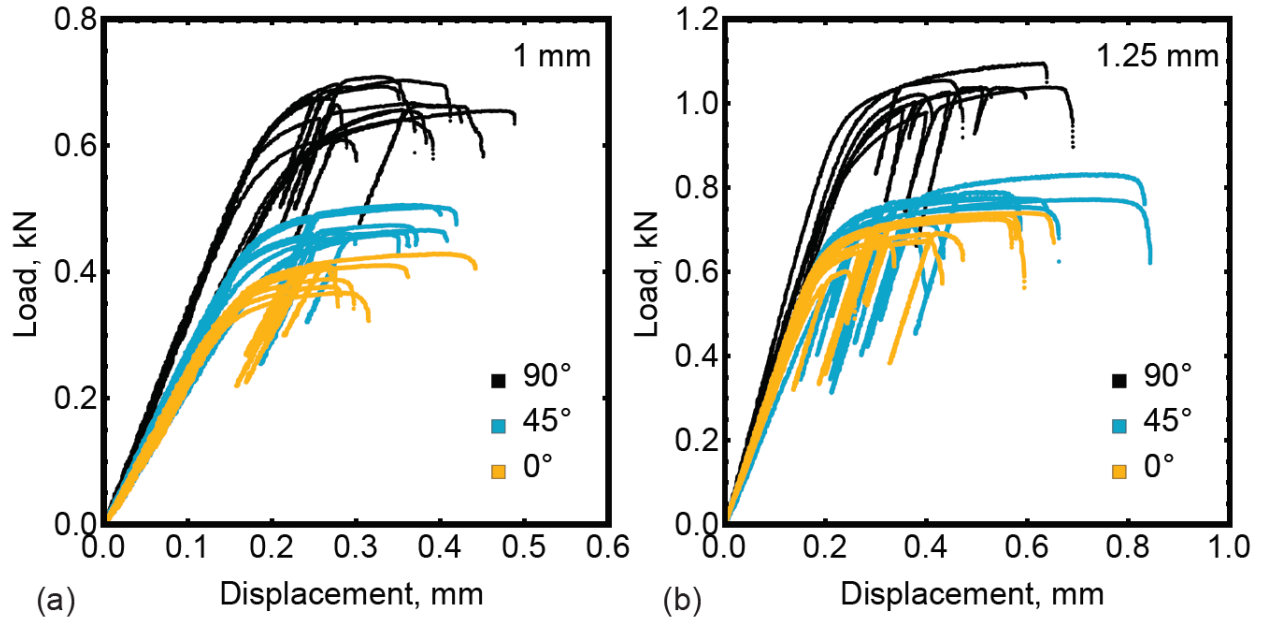


Figure 8. Load-displacement curves from the tensile tests conducted on struts of different diameter, printed at different orientations relative to the build direction. Note the strong orientation dependence of the peak loads, and for 1mm diameter struts, the elastic stiffness. The size-dependence is weaker in larger struts, but still present.

Figure 9 shows normalization by the nominal area and this experimentally-determined CT area; the peak stress for both normalizations is shown in the form of non-standard box plots. The area data was collected by fitting ellipses at various points along the struts, and repeated for multiple struts. The stress was then computed from the peak load in the strut experiments (**Figure 8**) and various measures of the strut cross-sectional area. The white bars represent the average stress based on all measurements for struts with the same orientation; the boxes represent the standard deviation of those stresses (i.e. using all data estimating the cross-sectional area of the strut). The tails represent the average values of the maximum/minimum values obtained from a collection of struts with the same orientation. A comparison of the 1 mm nominal diameter and 1.25 nominal diameter struts indicated a minor size effect, since the 0° and 45° struts for the smaller diameter struts appear to have a larger difference in average peak load than corresponding response of the larger diameter struts. It is clear from **Figure 9** that the orientation response of the struts cannot be solely explained via discrepancies between the nominal and as-printed cross-sectional areas.

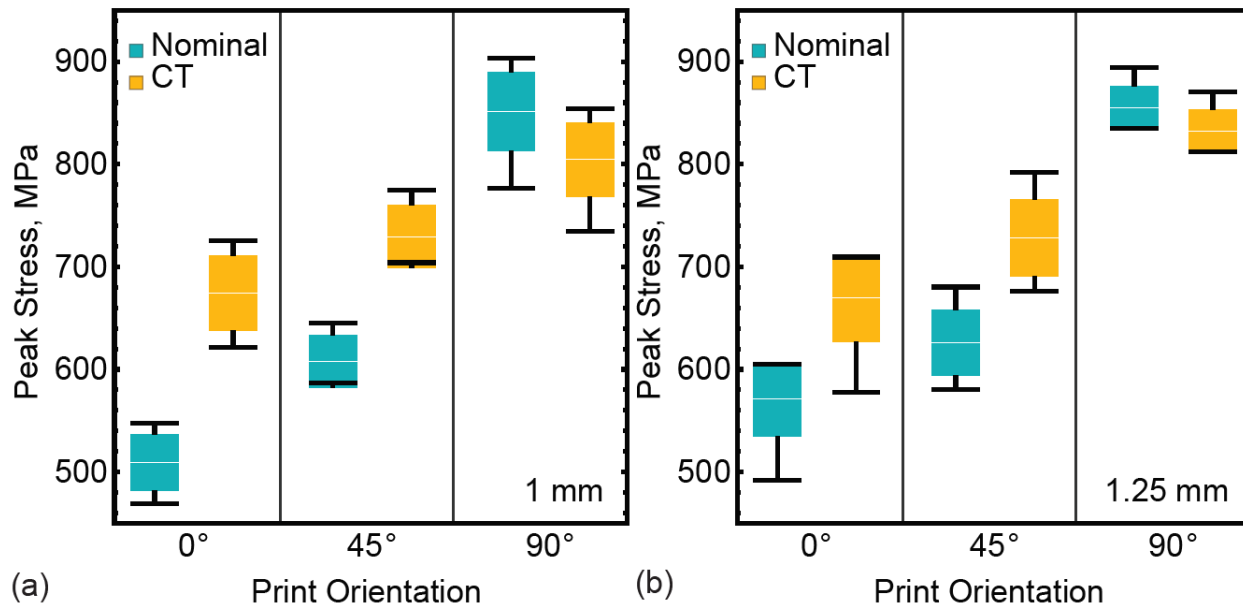


Figure 9. Peak load normalized to the nominal area and the average area given a print orientation based on CT scans (see later figures). The tails indicate the maximum and minimum peak stress for a given print orientation while the boxes display the average peak stress with bounds of one standard deviation above and below. Results are shown for struts with nominal diameter of (a) 1 mm and (b) 1.25 mm.

For the strut primitives and print orientations less than 90°, the peak stress with the nominal normalization is significantly lower than the peak stress with the normalizations based on the CT scans. This is because the 0° and 45° struts are undersized compared to the nominal dimensions while the 90° struts are oversized. For all struts, normalizing peak load by the average CT area narrows the spread in peak stresses among different print orientations but does not collapse the peak stresses to the same value. This is especially prominent in the 1.25 mm 90° case, as its peak stress remains significantly higher than the peak stresses of the 0° and 45° struts of the same nominal diameter. This suggests that, while geometric differences due to print orientation play an important role in resultant material properties, it is not sufficient to explain all deviations in material behavior.

The average peak stress normalized to the inscribed elliptical areas from **Figure 9** are significantly lower than the ultimate tensile strengths (UTS) of bulk EBM Ti-6Al-4V parts found by Murr, et al. [1-3, 7] and Facchini, et al. [8]. [It should be emphasized that in printed bulk components, the size variations due to surface roughness is negligible.] One reason for the discrepancy is that the primitives in this study were HIPed, which is known to result in microstructural coarsening, leading to decreases in strength [8, 9]. When comparing to the UTS of HIP'd EBM Ti-6Al-4V parts reported by Facchini, et al. [8], the average peak stresses are still significantly lower, with the exception of the average peak stress of those of the 90° struts with a nominal diameter of 1.25 mm. This is likely because the primitive struts were tested as fabricated while the samples tested by Facchini, et al. [8] were cut from bulk samples. The microstructure and texture of bulk EBM Ti-6Al-4V are significantly different than that of EBM Ti-6Al-4V thin-walled structures. Thin walled structures that are 1 mm thick consist of fine, curved-columnar prior β grains that grow inward from the exterior [5]. Bulk EBM Ti-6Al-4V structures have the

same microstructure along their exterior but have large, irregular, columnar prior β grains, which grow in the BD, within their interior [5, 10-12]. While HIPing does result in microstructural coarsening, it does not change the resultant morphology of the prior β grains, meaning that the descriptor of as-built EBM Ti-6Al-4V microstructure above likely applies to these samples [12]. In addition, surface roughness in the as-built parts can cause decreased mechanical performance as opposed to smooth samples cut from bulk specimens, which could also explain the discrepancies in reported strength [14].

4.2.2 Node Specimens

Node specimens were compression tested with two different print orientations and two different test orientations for a total of four types of tests, as shown in **Figure 10**. Representative results from these tests are shown in **Figure 11** for struts with a nominal diameter of 1 mm and 1.25 mm, respectively; the average measured peak loads and stiffness are listed in **Table 2** (appearing later in **Figure 13**). Node primitives tested in the 0° testing orientation (i.e. an “X” standing vertically) have a much stiffer and stronger response than struts tested in the 90° testing orientation (i.e. an “X” rotated on its side), since the strut axis are more closely aligned with the loading direction, and hence are dominated by axial compression of the struts. Conversely, the 90° testing orientation has strut axes that lie further from the loading direction and hence this is more strongly influenced by strut bending.

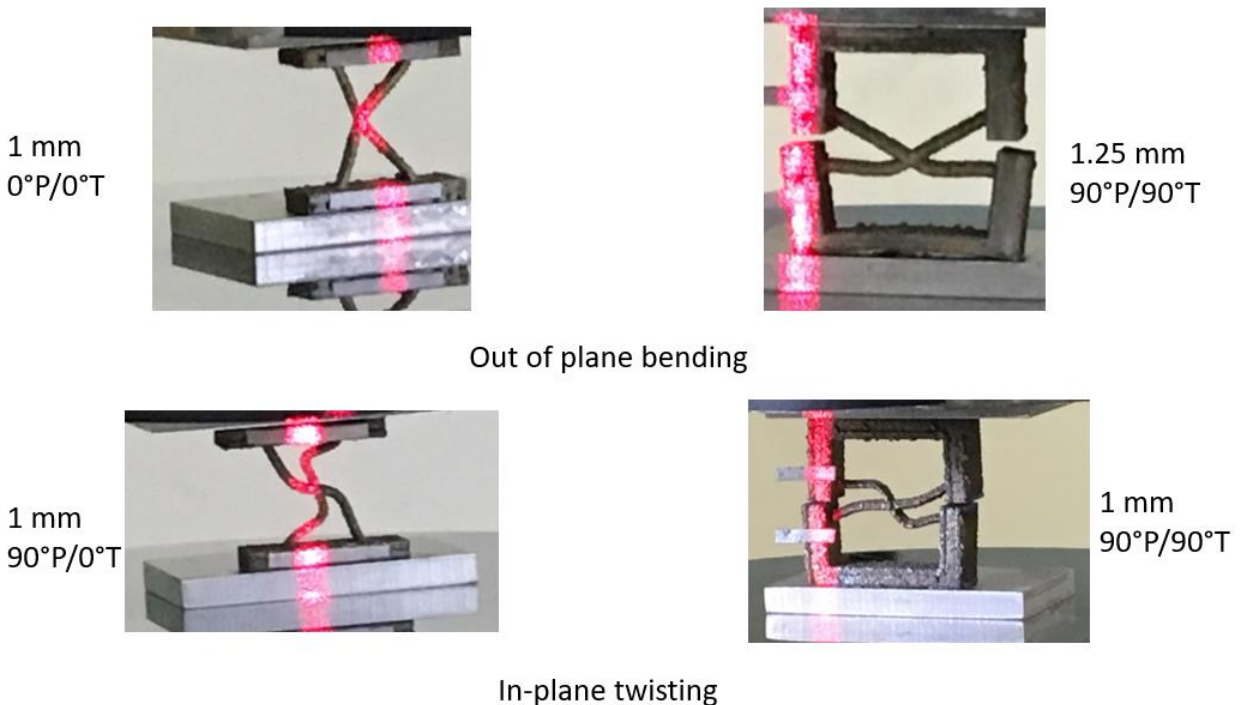


Figure 10. Optical images of Node B specimens deformed under uniaxial compression, tested in two different orientations, illustrating that multiple deformation modes are possible from identical specimens. A variety of platen conditions was considered. The pink lines illustrate the laser interferometry used to measure specimen compression.

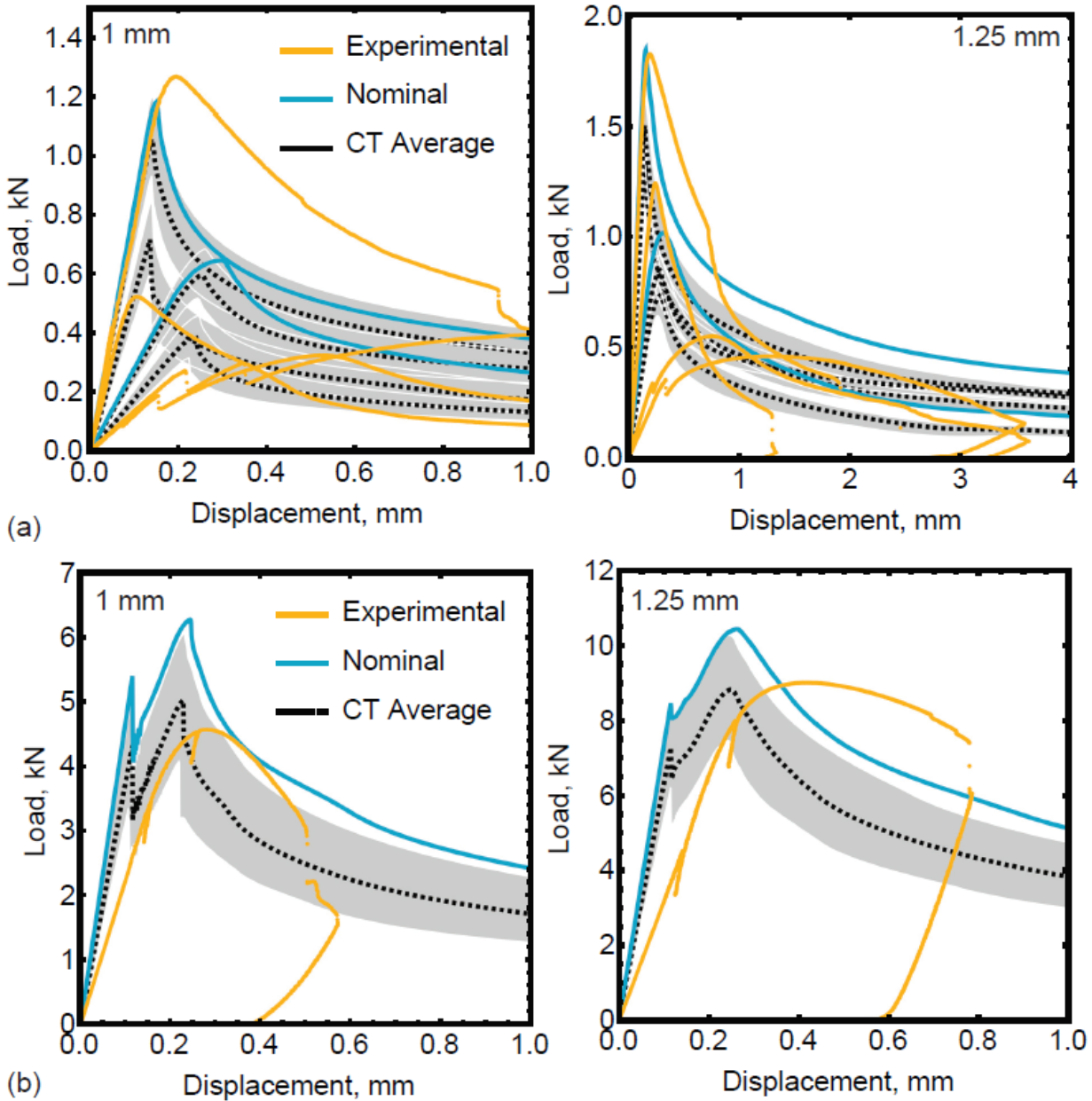


Figure 11. (a) Schematics depicting Node B the two print directions, 0° and 90° , as-printed (P) and the two testing orientations (T), 0° and 90° , after samples were cut with EDM. (b) Load-displacement curves of compression tests on the nodes for 0° and 90° print orientations in both testing orientations for nodes with a nominal diameter of 1 mm. (c) Load-displacement curves of compression tests on the nodes for 0° and 90° print orientations in both testing orientations for nodes with a nominal diameter of 1.25 mm.

As expected, the node primitives showed high sensitivity to the boundary conditions, which influences the elastic-plastic buckling load that controls strength. The results shown in **Figure 11** are for the ‘rigid’ boundary condition. When the “X” is printed lying flat in the build plane, the struts are oversized and produce much higher buckling loads (90° print/ 0° test). The response of

the rotated “X” (0° tests) showed similar behavior, with specimens printed parallel to the build plane being stronger due to thicker cross-sections; interesting, the smaller 1mm cross sections of the (0° print/ 90° test) allowed for out-of-plane buckling (as evidenced by strong softening after peak load), while this behavior was suppressed to very late stages of deformation in the nodes with thicker struts (90° print/ 90° test). Conversely, for the thicker 1.25 mm cross-sections, the dependence on print direction for the rotated “X” is far more muted, which is consistent with the strut behaviors seen in **Figure 8**.

As will be demonstrated, the node primitives showed elastic behaviors that were comparable to elastic-plastic beam element simulations, but smaller peak loads and much more gradual loss of load capacity than simulations. These behaviors are discussed in more detail in the sections on modeling.

4.2.3 Cell Primitives

The response of cell primitives is shown in **Figure 12**, along with optical images of crushed cells. The cell primitives deformed by two different mechanisms, as defined by post compression strut deformation. These mechanisms were categorized as “bend” or “kink”. A submechanism “straight”, which is a precursor to the “bend” mechanism but with the test stopped at a lower macroscopic displacement, was also noted. The “bend” mechanism involved all surface cross-struts on a face of the cell buckling and outer vertical struts buckling relatively symmetrically. Its “straight” precursor involved no apparent bending of the surface facial cross struts and minor symmetrical buckling of the outer vertical struts. The “kink” mechanism involved buckling of a single strut of the surface facial cross-struts and asymmetrical buckling of the outer vertical struts.

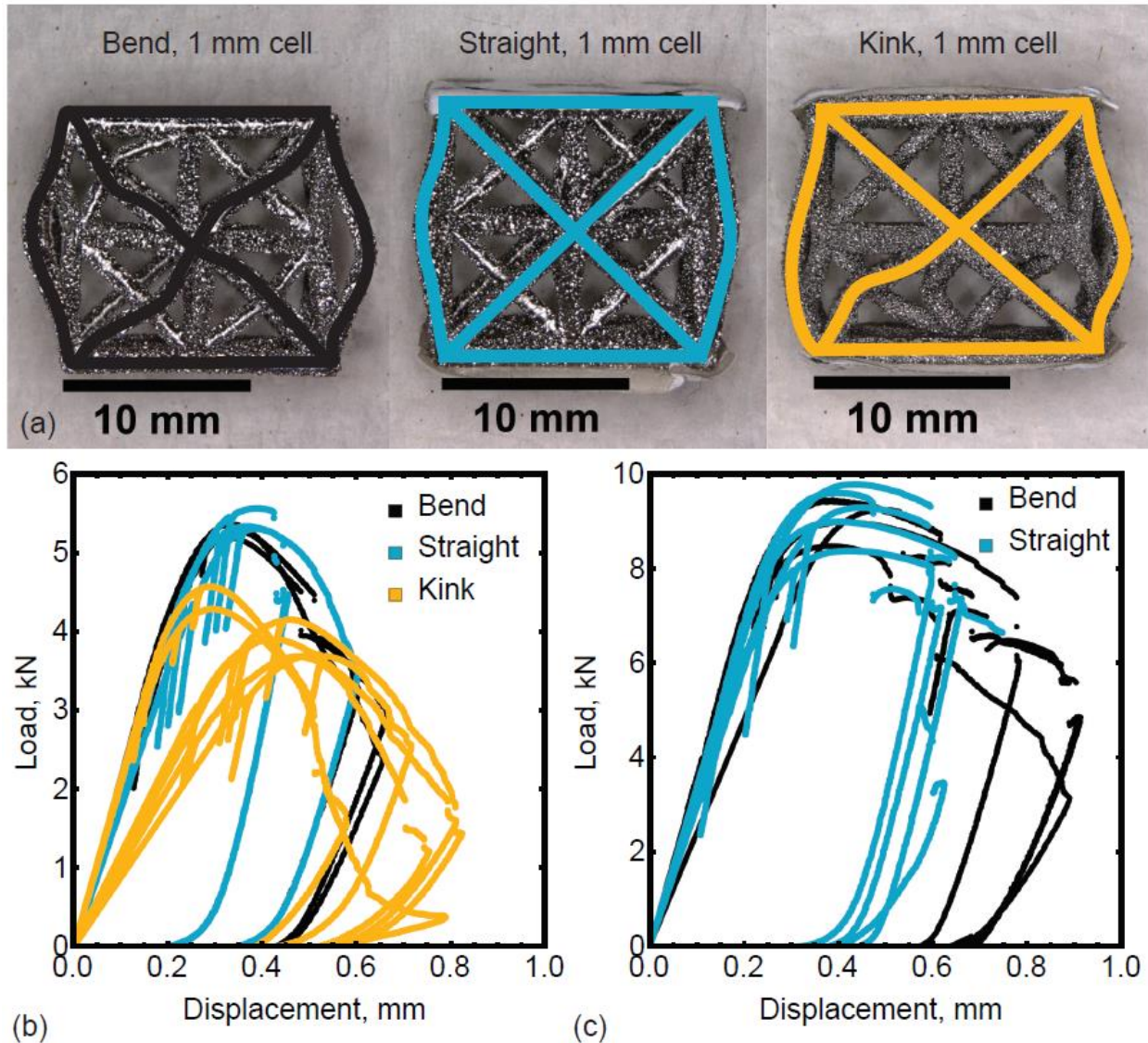


Figure 12. a) Optical images of the deformation modes Cell B specimens, with “bend”, “straight”, and “kink” schematics overlaid to display strut behavior. Load displacement curves of compression tests of the cell with results separated by deformation mode for cells with struts with a nominal diameter of (b) 1 mm and (c) 1.25 mm. Note that the cell with thicker struts exhibited no kink deformation mode.

The average peak loads and stiffness for the cell primitives are listed in **Table 3**. The “bend” mechanism and its “straight” precursor (test stopped at smaller macroscopic displacement) have a stiffer response and higher peak load than the “kink” mechanism, which only occurred in the cell with the smaller nominal diameter strut. Cells undergoing the “kink” mechanism tended to experience “first failure” (at least one of the struts fracturing) at a larger macroscopic displacement than cells undergoing the “bend” mechanism, i.e., the formation of a kink leads to loss of load capacity at a given displacement. Given that the kinked strut is not necessarily the highest loaded strut (i.e. the kink forms from a defect), one cannot necessarily assume the kinked

strut fails first. A kink may form, and experience unloading during continued deformation of the cage.

One can immediately see that the cell primitives with 1 mm struts exhibit much more variation in response; this is a consequence of the more significant impact of surface defects in the struts and near the nodes. Since these defects are controlled by powder size, they represent a more significant fraction of the strut dimension than for the 1.25 mm case. Characterization of these defects is described in the next section.

Table 1. Strut peak load and stiffness

Orientation	Peak Load, kN		Stiffness, kN/mm	
	1 mm	1.25 mm	1 mm	1.25 mm
0°	0.400 ± 0.022	0.701 ± 0.044	2.496 ± 0.042	3.844 ± 0.118
45°	0.477 ± 0.020	0.768 ± 0.039	2.859 ± 0.049	4.155 ± 0.253
90°	0.668 ± 0.030	1.050 ± 0.025	3.590 ± 0.070	5.185 ± 0.520

Table 2. Node peak load and stiffness

Orientation	Peak Load, kN		Stiffness, kN/mm	
	1 mm	1.25 mm	1 mm	1.25 mm
0° Print, 0° Test	0.569 ± 0.052	1.139 ± 0.084	6.039 ± 0.475	9.054 ± 1.678
90° Print, 0° Test	1.371 ± 0.123	1.965 ± 0.124	9.722 ± 0.821	12.054 ± 3.000
0° Print, 90° Test	0.324 ± 0.021	0.559 ± 0.020	1.114 ± 0.148	1.846 ± 0.160
90° Print, 90° Test	0.408 ± 0.025	0.470 ± 0.008	1.689 ± 0.153	1.499 ± 0.407

Table 3. Cell peak load and stiffness

Deformation mode	Peak Load, kN		Stiffness, kN/mm	
	1 mm	1.25 mm	1 mm	1.25 mm
Bend	5.288 ± 0.082	9.056 ± 0.423	45.226 ± 2.993	66.076 ± 11.370
Straight	5.413 ± 0.143	9.229 ± 0.556	46.268 ± 3.375	69.842 ± 3.398
Kink	4.060 ± 0.349	—	33.279 ± 3.015	—

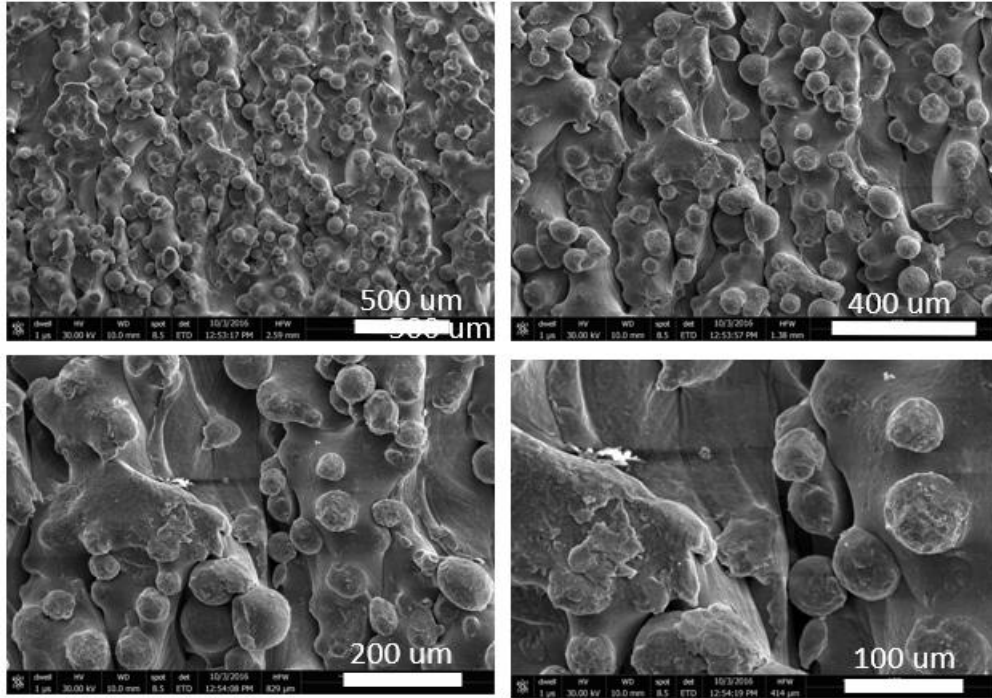
5. CHARACTERIZATION

5.1 Methods

Strut surfaces and polished strut cross-sections were analyzed using optical and scanning electron microscopy. (A limited amount of electron backscattered diffraction (EBSD) characterization was conducted on the polished strut surfaces; this exploratory study was relatively inconclusive and represents an area for future research). Further, four node primitives and two cell primitives were analyzed by x-ray computed tomography (CT) via a North Star Imaging X50 CT machine equipped with a 200 micron PerkinElmer detector. The node reconstructed images have a voxel size of either 34.38 μm or 34.44 μm over a length of roughly 20 mm. The reconstructed images for the cells have a voxel size of 27 μm over a length of roughly 17 mm. *ImageJ* software with its in-house plugins were used to quantitatively analyze the images. The maximum inscribed ellipse of the strut cross-section within the nodes and cells was determined every 27 μm along the strut.

5.2 Results & Discussion

Figure 13 shows representative SEM images of the strut surfaces at four different levels of magnification. One clearly observes surface connected defects with spacing and dimensions roughly equal to 2-3 powder diameters. **Figure 14** shows polished cross-sections of the struts; note that HIP post-processing has appeared to completely remove interior defects (pores) at this magnification. For the 45° and 90° struts, the bottom of the image in Figure 14 corresponds to the bottom of a part in the build volume; i.e. the build direction is roughly bottom-to-top for those two images. (For the 0° strut, there is not asymmetry in the surface roughness.) A tribeam dataset was generated for a single specimen of as-printed material, taken from the frame surrounding the node primitives; this confirmed the lack of interior defects through the specimens. Results of EBSD characterization of the polished strut cross-sections are shown in **Figure 15**; while the strut orientation leads to differences in structure, the impact of these differences has not been quantified and is discussed in the final section on future work.



M.P. Echlin

Figure 13. Scanning electron micrographs of the as-printed strut surfaces at various levels of magnification, show hierarchical surface roughness; the deep crevices seen at high magnification are all surface-connected; 3D tri-beam sectioning of the specimens reveal submicron porosity, a result of the HIP post-processing step.

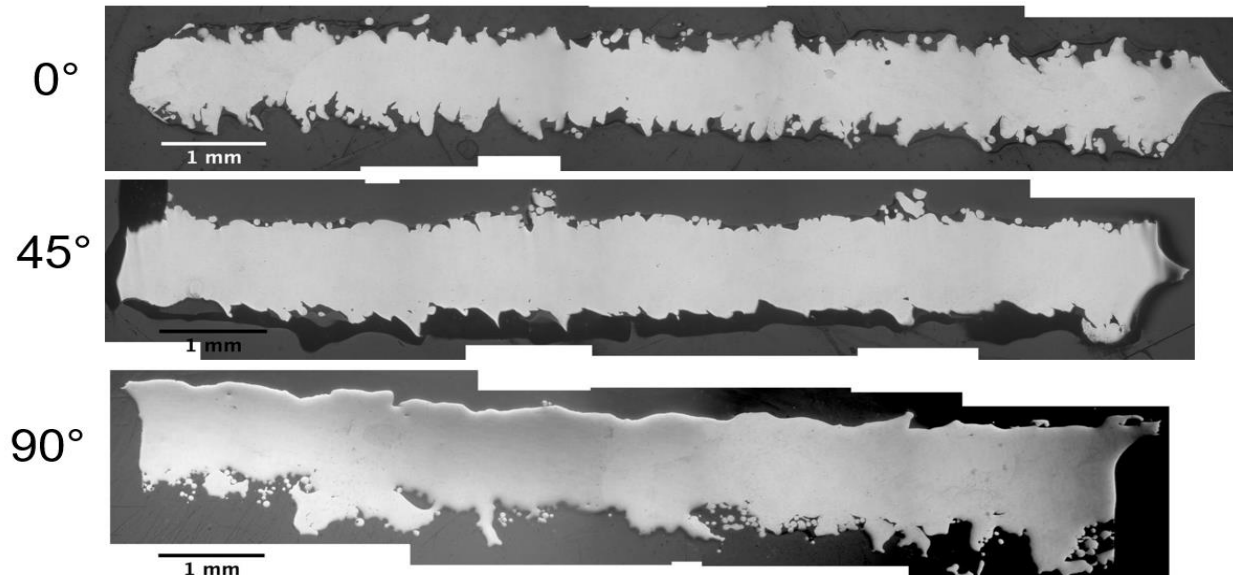


Figure 14. Composite optical micrographs of 1 mm diameter struts after polishing, illustrating the strong orientation dependence of both surface roughness and strut size; geometric deviations from nominal geometry explain part of the orientation-dependence, but even accounting for these differences, orientation-dependence remains. (See Figure 9.)

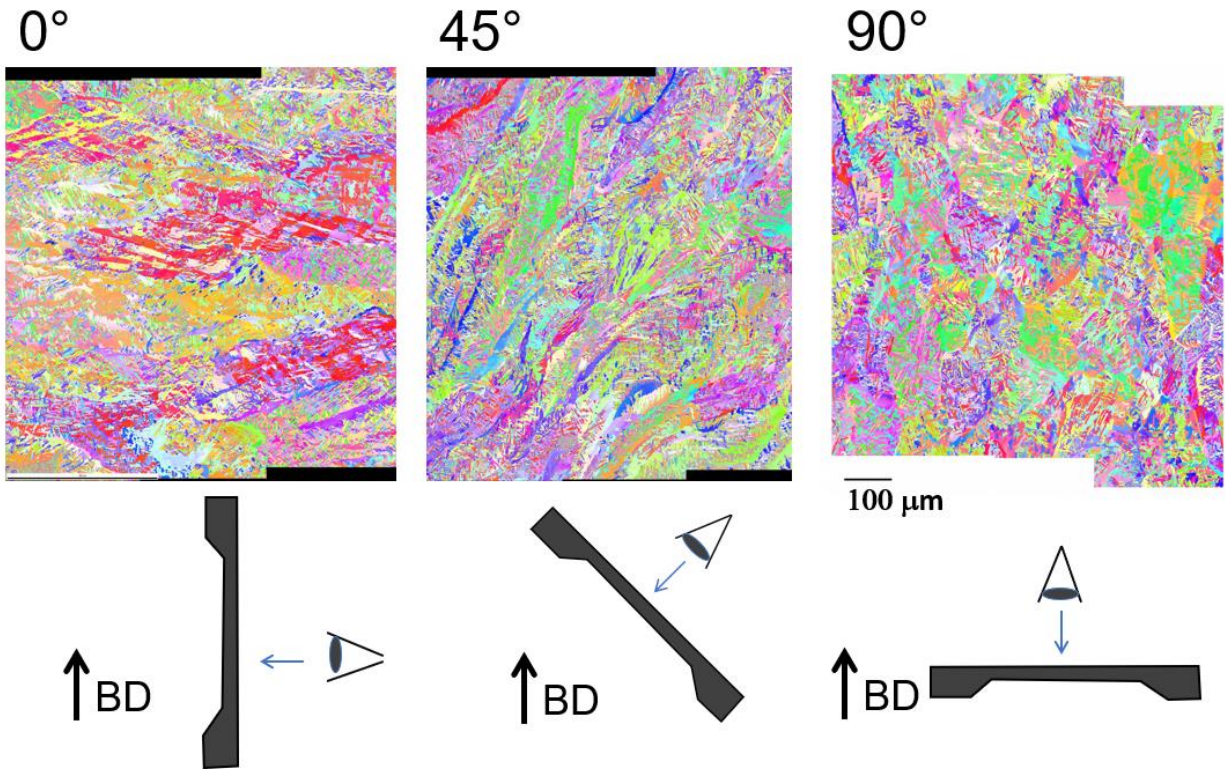
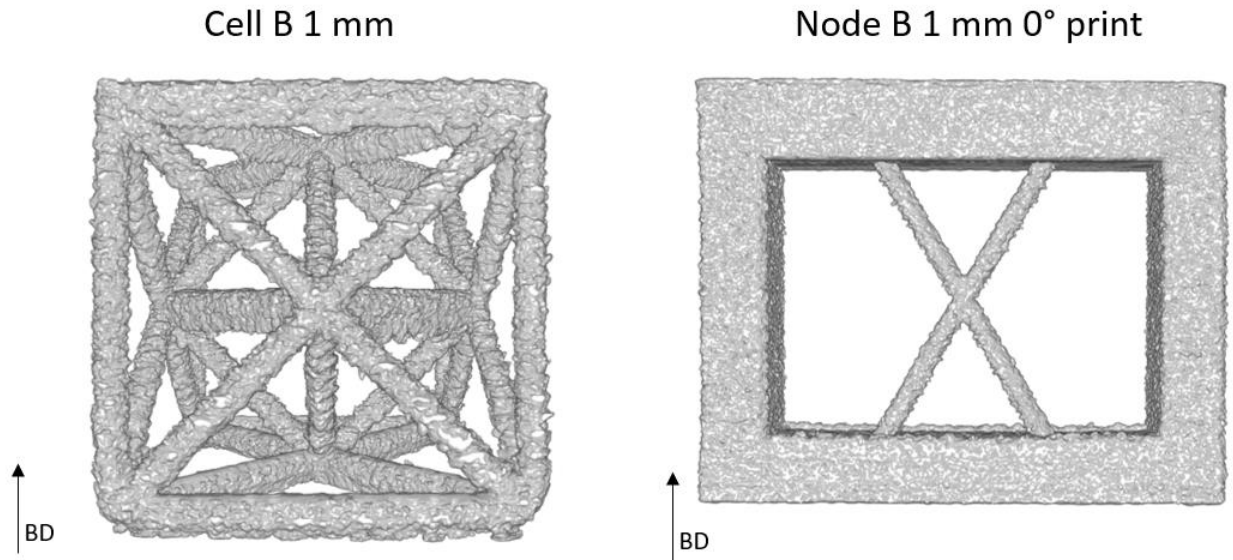


Figure 15. EBSD characterization of polished strut cross-sections oriented so that the 001 direction is in line (such as those shown in Figure 15), illustrating complex microstructures that depend on orientation. Note the build direction relative to the EBSD plane is indicated by the schematics below the figures.

3D geometric characterization of the cells and nodes provide insights into understanding the influence of the EBM process on the resultant properties and mechanical behavior of the primitives. **Figure 16** shows representative volume reconstruction images from the CT characterization of one cell and one node primitives. The image for the cell primitive clearly illustrates that the orientation of the strut relative to the print direction impacts strut geometry; note that the struts at 90° from the print orientation (horizontal in this figure) exhibit cross sections that elongated in the build direction.



In collaboration with Sean Donegan, AFRL

Figure 16. CT scans of Cell B and Node B specimens; the Cell B image shows clear variations in strut geometry with orientation relative to the build direction (vertical in this picture). Full movies of the scans are available in the supplemental information. These scans were post-processed to analyze statistical variations in strut cross-section as a function of build orientation.

Examples of volume reconstructions of struts taken from the full CT dataset of the cell and node primitives are shown in **Figure 17** and **Figure 18**. These figures show surface images of the struts, as well as two-dimensional slices perpendicular to the main strut axis. The 2D slices were taken on a plane that is perpendicular to the main axis of the strut, with the main axis computed from a line passing through geometric center points. The results in these figures clearly illustrate that cross-sectional shape and surface roughness of the struts depend strongly on their orientation relative to the build direction.

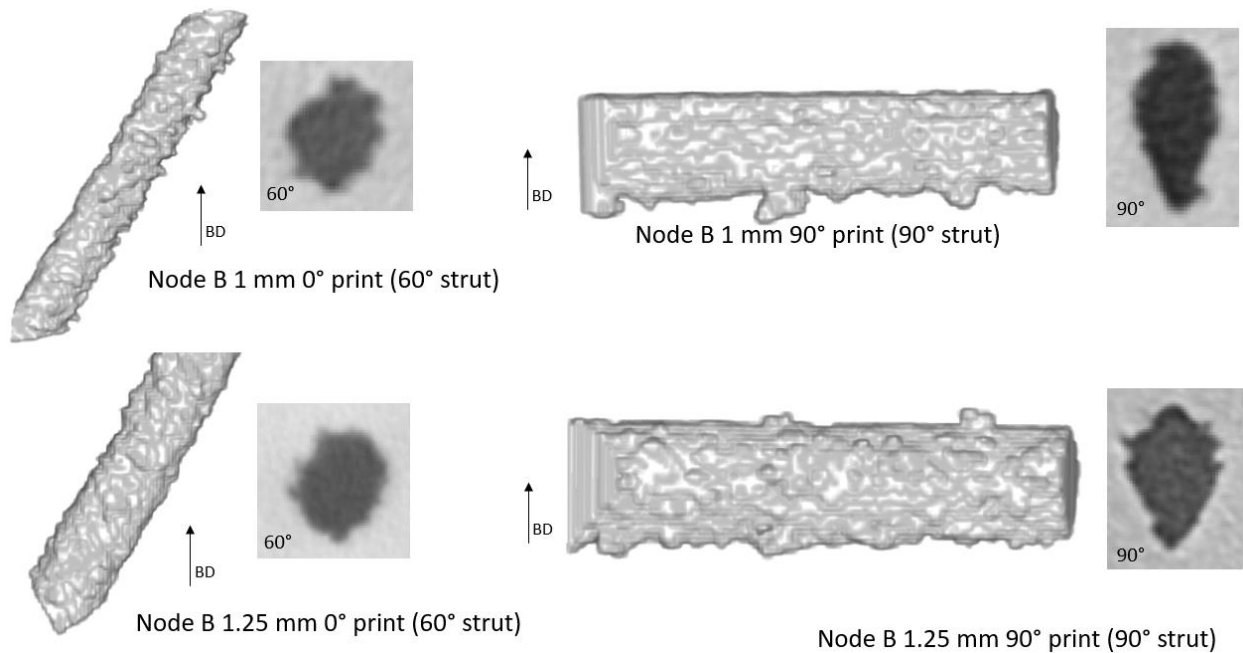


Figure 17. 2D slices from the 3D CT dataset for Node B, showing variations in strut cross-section along their length.

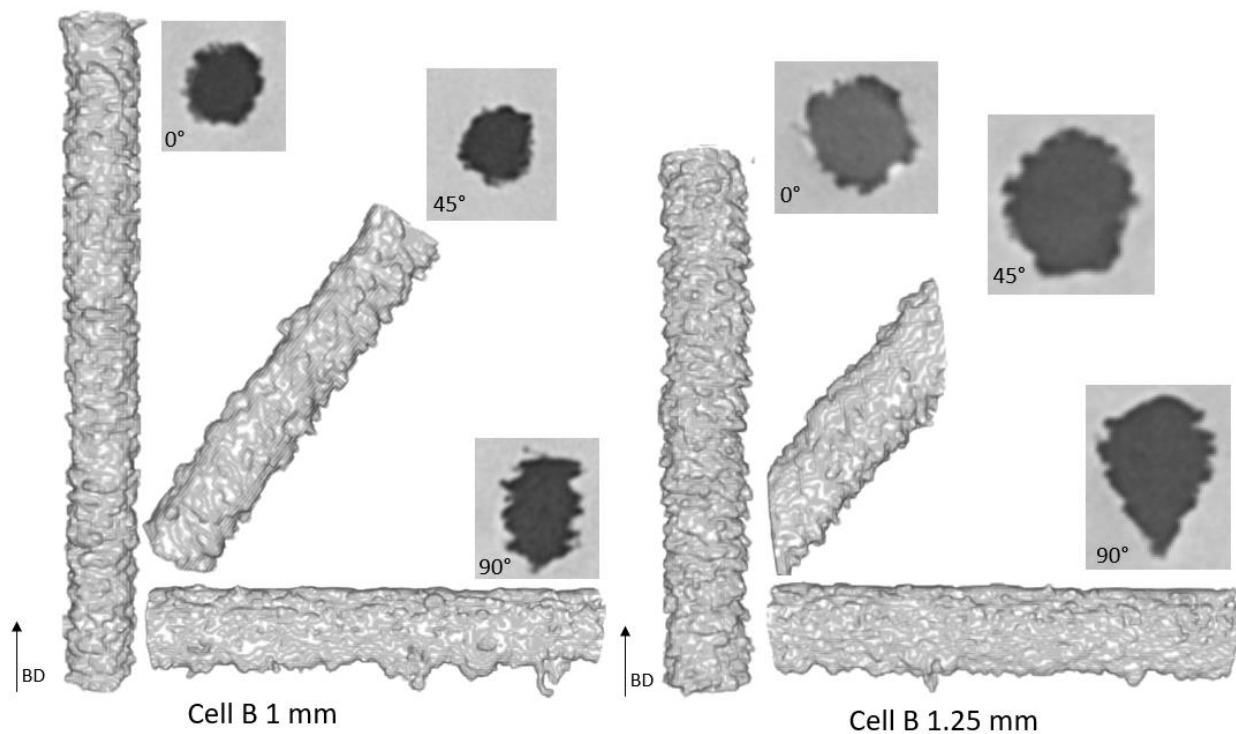


Figure 18. 2D slices from the 3D CT dataset for Cell B, showing variations in strut cross-section along their length.

As shown from **Figure 17** and **Figure 18**, the as-printed structures display significant surface roughness, which obviously are a result of the printing process. It is likely that regions with significant roughness and irregularities do not contribute to the load bearing capability of the structure, which should be a consideration when trying to determine material properties from these parts. Structures also display geometric differences. Example cross-sections of struts show that struts printed at an angle of 0° and 45° tend to have more circular cross-sections while struts printed at an angle of 90° tend to have elliptical cross-sections that are more elongated in the build direction. Further, struts printed at an angle of 90° appear to have larger cross-sectional areas.

The area normalized to the nominal area prescribed by the input computer-aided design (CAD) file and the aspect ratio of the inscribed ellipses fit to the cross-sections of all the struts in the nodes and cells was also determined using the CT dataset. Representative results are shown in **Figure 19**. The white line in the center of the boxes in **Figure 19** displays the average of the mean over all of the struts in a sample for a given orientation. The tails display the average maximum and minimum values, respectively, while the bounds of the box represent an average standard deviation above and below the average mean value. Results are shown for both nodes and cells, with struts with a nominal diameter of 1 mm or 1.25 mm.

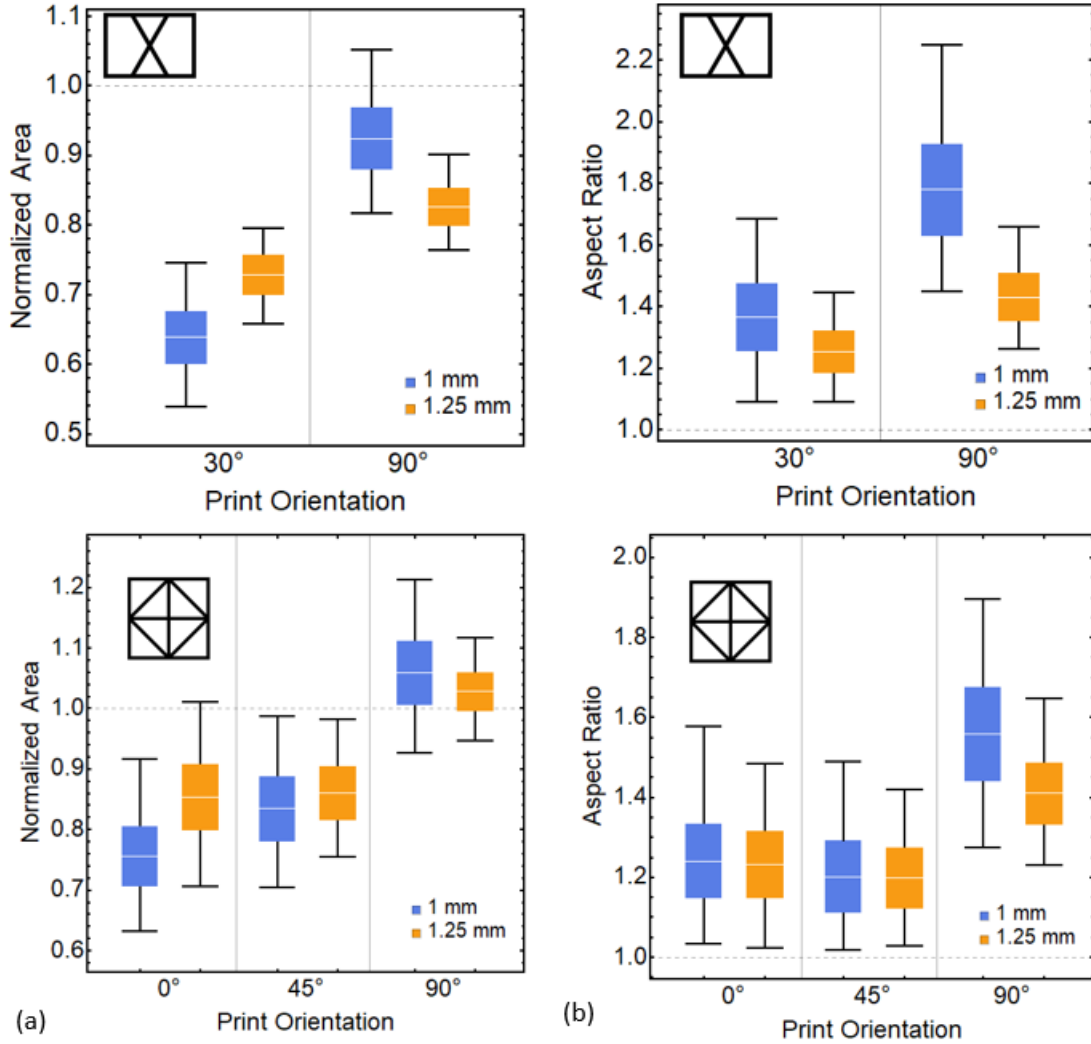


Figure 19. Plots of (a) area normalized to nominal area and (b) aspect ratio of inscribed ellipses for all struts in nodes and (c) normalized area and (d) aspect ratio of inscribed ellipses fit to individual struts within a print orientation in cells. Tails display the average maximum and minimum of within a print orientation while boxes display one average standard deviation above and below the average of the average value.

All struts in node primitives printed in the 0° orientation have a print orientation of 30° while all struts in nodes printed in the 90° orientation have a print orientation of 90° . From **Figure 19**, the normalized area and aspect ratio of nodes with 30° struts are significantly lower than nodes with 90° struts, for the same nominal diameter. There appears to be a significant size effect in normalized area for the struts of both print orientations, as the thinner struts (nominal diameter of 1 mm) have a lower normalized area for the 30° print orientation and a higher normalized area for the 90° print orientation, as compared to the thicker struts (nominal diameter of 1.25 mm). For aspect ratio, a significant size effect occurs in the 90° print orientation, with thinner struts being more elongated than thicker struts.

Similar to struts in the node primitives, the orientation of struts in cages relative to the build direction impacts the normalized area and aspect ratio of each strut in the cage. From **Figure 19**, the 90° struts have both a higher normalized area and aspect ratio than the 0° and 45° struts, which matches the trend found in the struts of the nodes. The 0° and 45° struts have approximately the same aspect ratio and normalized area. Unlike in the node samples, significant size effects are not apparent in the cell primitives; struts with a nominal diameter of 1 mm behave similarly to struts with a nominal diameter of 1.25 mm. However, there may be a minor size effect in normalized area with the 0° struts since the 1 mm nominal diameter struts have a lower normalized area than the 1.25 mm.

To examine the axial distances over which surface defects persist, the struts were characterized by examining the autocorrelation of strut diameter as a function of position along the strut, as shown in **Figure 20**, Autocorrelation was computed using Mathematica's in-built "Correlation Function" functionality. From the autocorrelation, the persistence length, defined to be the length at which the autocorrelation value falls within the 95% confidence interval of not being correlated, was determined. The autocorrelation measurement provides an indicator of the length over which strut size varies significantly; the persistence length provides an average measure of this correlation length. Larger correlation lengths imply that strut size variations are small along the axis of the strut, since a given diameter will persist over larger distances. **Figure 21** shows the average persistence length in the struts as a function of strut size and orientation. The 90° struts clearly have much larger persistence lengths, indicating that their size varies less over larger distances than lower angle struts. For low angle struts, the persistence length is approximately 2-3 powder diameters, indicating that powder diameter strongly impacts size variations in these configurations.

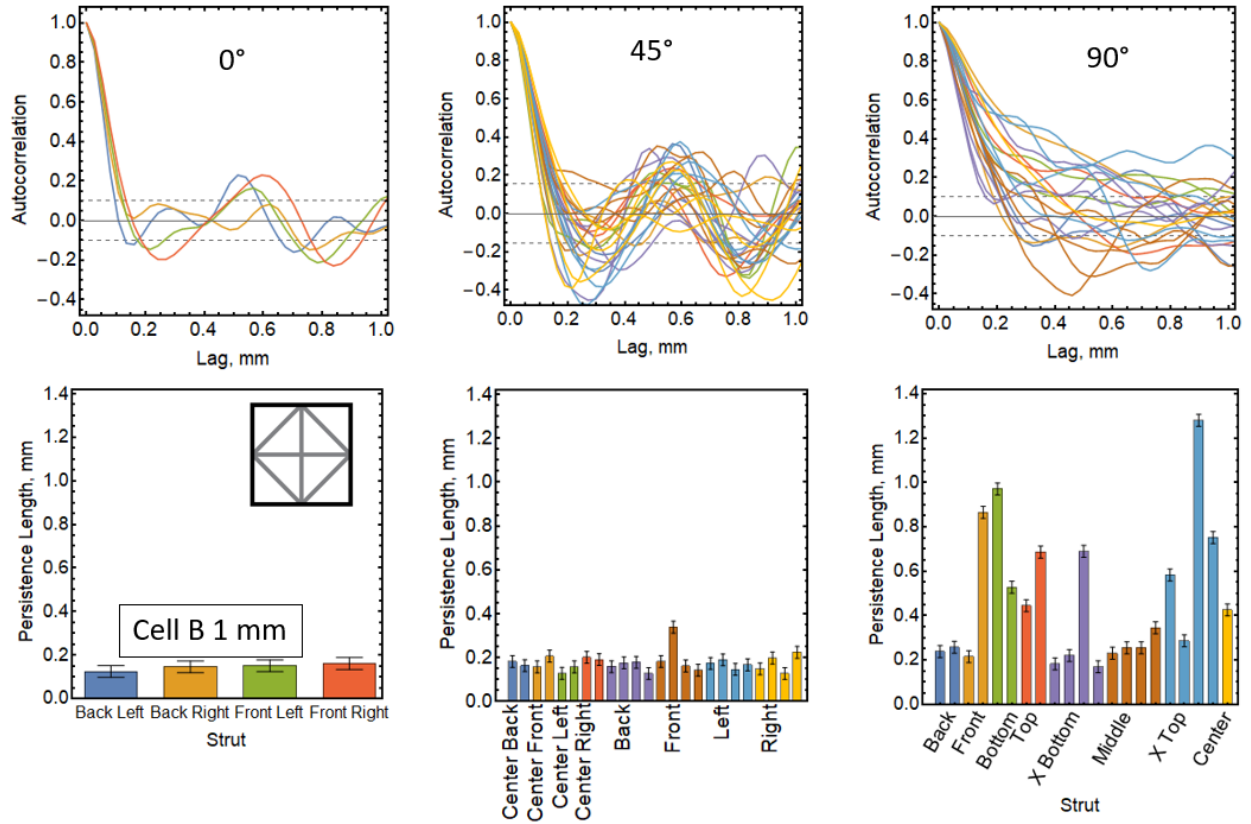


Figure 20. Autocorrelation functions for diameter as a function of location along a strut, which provides a measure of the size variability in the struts, and the characteristic length-scale between peaks and valleys.

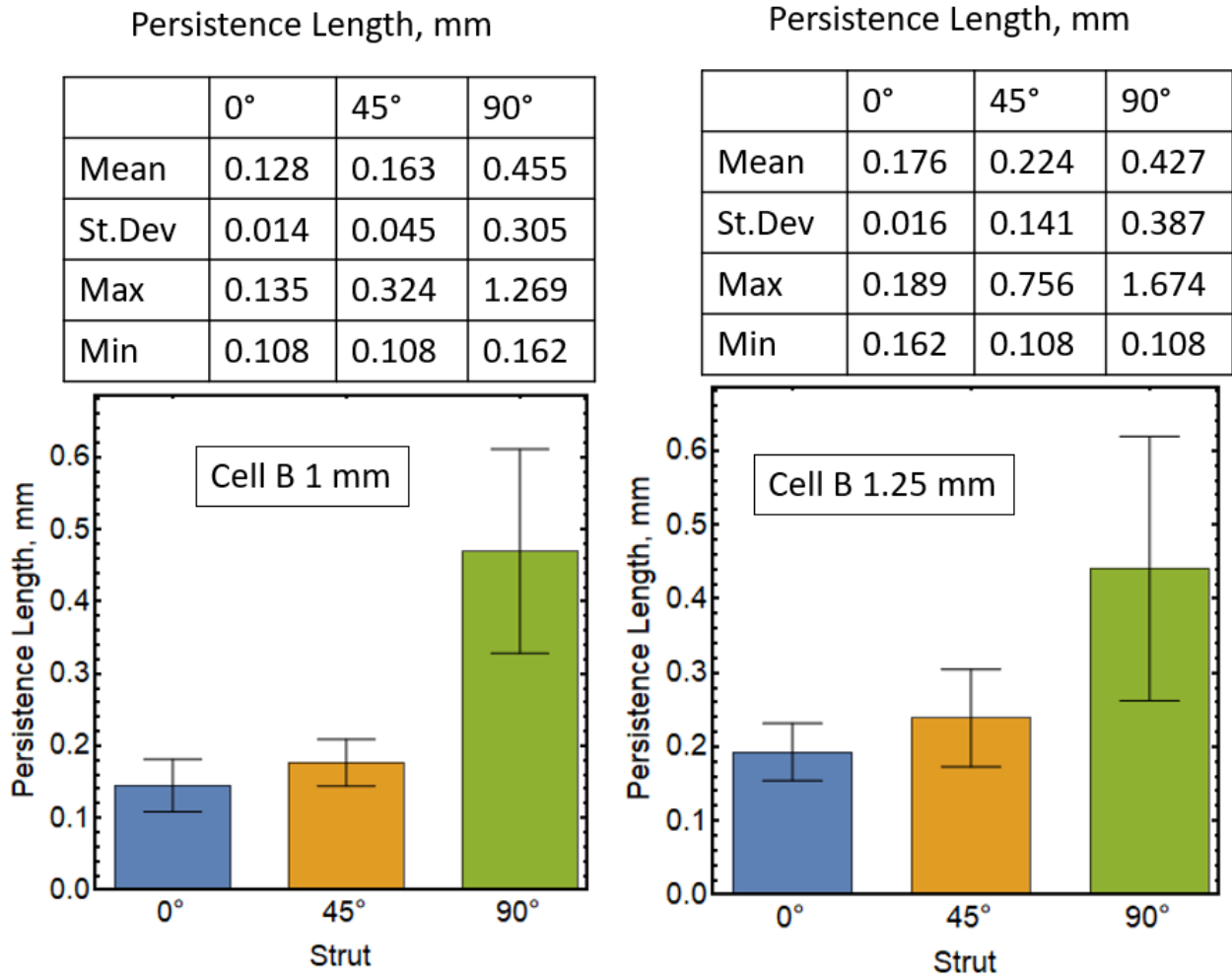


Figure 21. Persistence length for surface features indicating the distance over which variations in strut diameter are correlated; the results clearly demonstrate that struts oriented with the build direction have stronger variations in strut diameter, as indicated in Fig.15

The trends in normalized area and aspect ratio of struts in the nodes and cells follow those previously reported by Suard, et al. [13] and Perez-Sanchez, et al. [14], who also observed that cross-sections of struts fabricated perpendicular to the print direction tended to have larger cross-sectional areas and aspect ratios than those of struts fabricated parallel or oblique to the print direction. This geometric effect with respect to print orientation can be explained by the thermal conditions of the part. Fabricated struts are surrounded by loose, unmelted Ti-6Al-4V powder, which has a much lower thermal conductivity than that of the solidified part and the build plate (bottom plate). Because of this difference in thermal conductivity, the primary direction of the heat flux is from the melt pool down through the melted part and towards the build plate [13, 15]. For 0°, 30°, and 45° struts, the thermal flux is dissipated through the strut, resulting in a more equiaxed cross-section. For the 90° struts, thermal flux accumulates on the side facing the start plate, resulting in over melting in that direction. The resultant strut cross section is therefore elongated in the build direction.

In the node primitives, all struts are undersized, though the struts in the 90° print orientation tend to be close (within 80%) of the prescribed area. For both sizes of struts in the cells, the 0° and 45° struts tend to be undersized in comparison to the nominal while the 90° struts tend to be oversized. Oversizing of the 90° struts occurs due to over melting as described previously. Undersizing of struts in truss structures built using the default ARCAM print theme has been previously reported by Smith, et al. [16]. The default process parameters result in excessive beam energy density in regions with no prior melted material beneath them. This causes material to rise above the layer the electron beam is rastering, resulting in improper powder deposition in subsequent layers and undersizing of actual components [16]. The discrepancy between the resultant strut sizes of the 90° struts in the nodes and cells can be explained by the different sample sizes. The cells are larger specimens, which means they take longer to build. This allows for more time for over melting to occur, resulting in oversized struts.

Average measures of surface roughness are insightful, but are likely not sufficient to characterize the mechanical response of the struts, due to isolated defects that may be much larger and more deleterious than those associated with surface roughness. This is illustrated in **Figure 22**, which shows volumetric reconstruction of a node and a strut and clearly indicates the presence of larger scale defects that will limit mechanical response. Defects such as those shown in **Figure 22** motivate the numerical studies shown in the next section, which focus on the impact of large defects on overall macroscopic response.

Ideally, one would like to quantify the types of defects seen in **Figure 22**, particularly estimates of peak-to-valley distances measured from the center of the defect to the adjacent material. This computation is complicated by the fact that such defects have strong circumferential variations (traversing around the strut at fixed position along the strut). New algorithms are needed to post-process the data to account for this angular dependence of such large defects.

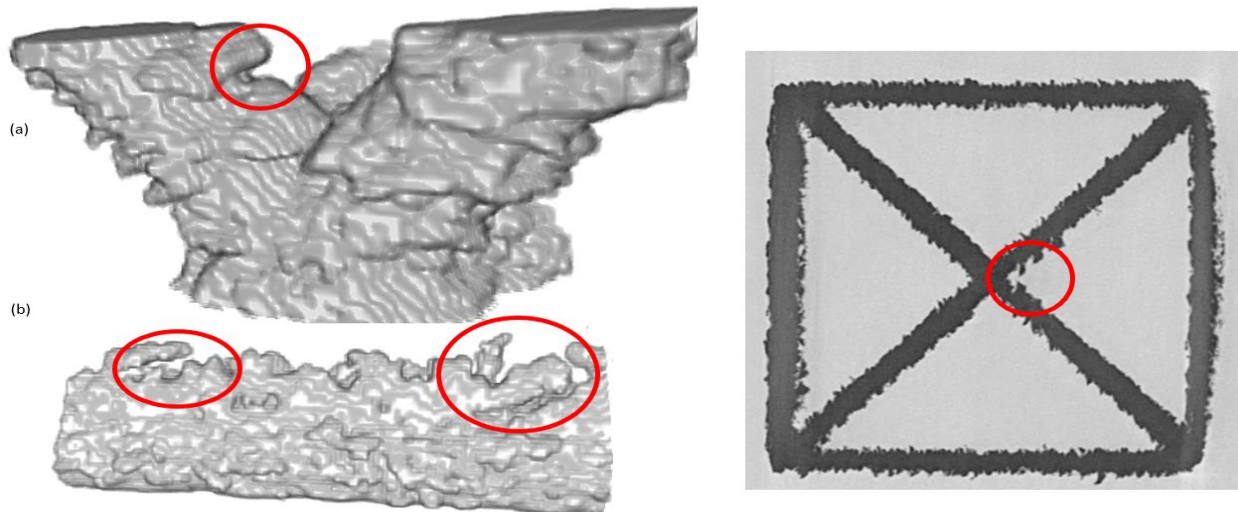


Figure 22. (a) CT reconstruction of a print defect near a node from a cell with a nominal strut diameter of 1 mm. (b) CT reconstruction of a strut from the same sample with two print defects shown. Note that the lines on the CT image are voxels from the CT reconstruction and not print layers.

5.3 Key Outcomes

- The geometry of struts in both node primitives and cell primitives show similar orientation-dependence, with undersized areas (as compared to nominal intended print area) for all orientations less than 90°. Struts printed at 90° from the build direction were slightly undersized for the node primitives, and slightly oversized for the cell primitives.
- Orientation dependence is much stronger for the 1 mm nominal struts than for the 1.25 nominal struts, with the latter exhibit significant dependence only in the jump from 45° to 90°.
- In all instances, the struts were (on average) non-circular, with significant deviations for the 90° print orientation (i.e. aspect ratios of ~1.6). The direction of maximum width is aligned with the build direction.
- Average measures of strut size (diameter) variations in the axial direction are approximately 2-3 powder diameters; the persistence length of equivalent strut size is approximately 1-3 powder diameters for struts printed at less than 90°; the 90° struts have much larger persistence lengths, indicating cross-sections with smaller variations in size along their length.
- Average measures of strut size (diameter) variations are insightful, but are likely not sufficient to characterize the mechanical response of the struts, due to isolated defects that may be much larger and more deleterious than those associated with surface roughness. The CT scans revealed large surface defects on the order of 30-50% of the strut diameter, with no apparent systematic location with respect to the primitive(s) geometry.

6. ANALYTICAL MODELS OF STRUT COLLAPSE

6.1 Overview

This section describes an analytical analysis of the elastic-plastic behavior of struts subjected to uniform applied forces and moments. The analysis provides insight regarding the nature of plastic zone evolution in struts under combined stretching and bending, and quantifies the coupling between deformation modes.

The analysis also provides insight regarding the behavior of surface defects, or ‘notches’, which lead to localized net-section yielding, as shown in **Figure 23**; the present analysis is motivated by the hypothesis that plastic localization near surface defects can be accounted for using ‘defect elements’ that capture global structural response, without having to resort to fully resolved two- or three-dimensional FEA near the defect. These defect elements can then be distributed throughout a structure to quantify the impact of distributed printing defects.

The rationale for the present analysis is that the response of the material adjacent to the notch can be viewed as a strut with reduced area that is offset from the main strut axis. The idealized ‘notch element’ relates stretch and bending deformation in the notch to the resultant force and moment at the location of the notch. As shown in **Figure 23**, the effective notch element must be offset from the main axis of the strut to account for eccentricity introduced by the notch. In an FEA framework, this implies that rigid links must be placed between the nodes of the elements in the intact strut and the node in the notch element.

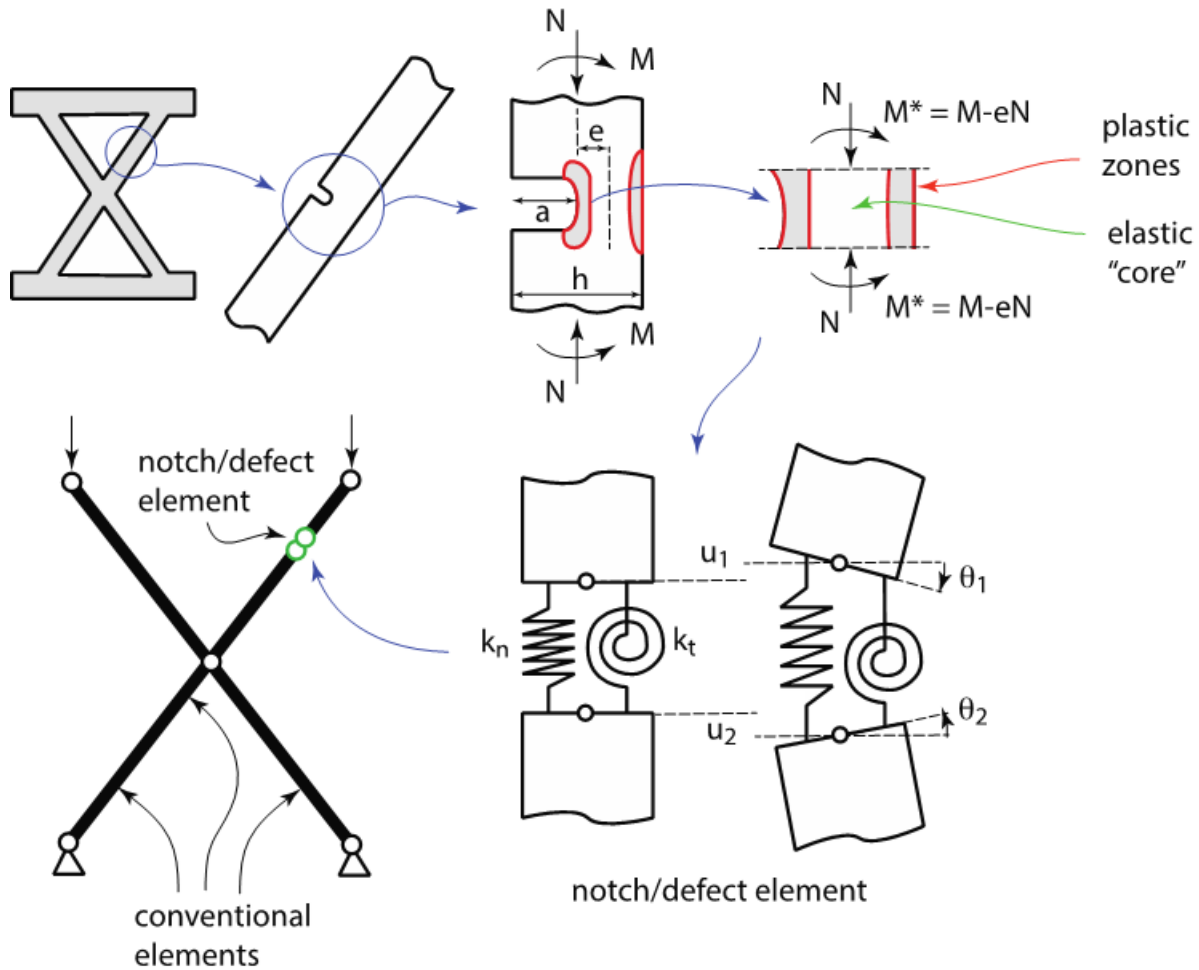


Figure 23. Conceptual overview of defect modeling with beam elements; the presence of a surface defect is modeled using an elastic-plastic beam element that forms a plastic skin at the notch; theoretical relationships for the moment/force vs. curvature/stretch relationship of the notch were derived and used to map out response.

Full analytical descriptions of the 'notch element' have been derived assuming that stretch and curvature do not decrease with applied far-field loading; that is, stretch and curvature in the element increase or decrease monotonically. In essence, these equations define relationships between stretch, curvature, force and moment as a function of beam dimensions, as well as the size and extent of 'plastic zones' (that form on either side of the beam element). Ultimately, this analysis corresponds to the simplified response of a single conventional beam element; the latter was used to study the impact of defects in struts.

6.2 Method

Here, we assume elastic, perfectly plastic response of the material, which is consistent with the very low hardening observed macroscopically in Ti-64. The response of an elastic, perfectly plastic beam subjected to uniform stretch and curvature can be analyzed simply by solving for

the sizes of the plastic ‘skins’ that form on either side of the beam. The right side of **Figure 24** illustrates a response map that indicates the type of response expected for each state of deformation. Combinations of stretch and curvature in the green region lead to purely elastic response; the red regions indicate stretch/curvature combinations associated with complete net section yielding. The yellow regions indicate combinations where at least one side of the defect element has yielded.

As shown in **Figure 24**, the plastic zones on either side of the defect element are in general asymmetric, owing to the fact that the axial force will either add to or subtract from the stresses generated by the bending moment. The size of the plastic zone on either side is found by equating the strain (defined by the imposed stretch and curvature) to the yield strain: the stress is defined by linear elasticity inside this region, and the yield stress outside this region where the imposed deformation exceeds the yield strain. Once the plastic zone sizes are defined in terms of the applied stretch and curvature, the stress profile is integrated to obtain the resultant force and moment associated with the imposed deformation. This process leads to complete closed-form expressions for the response of the beam.

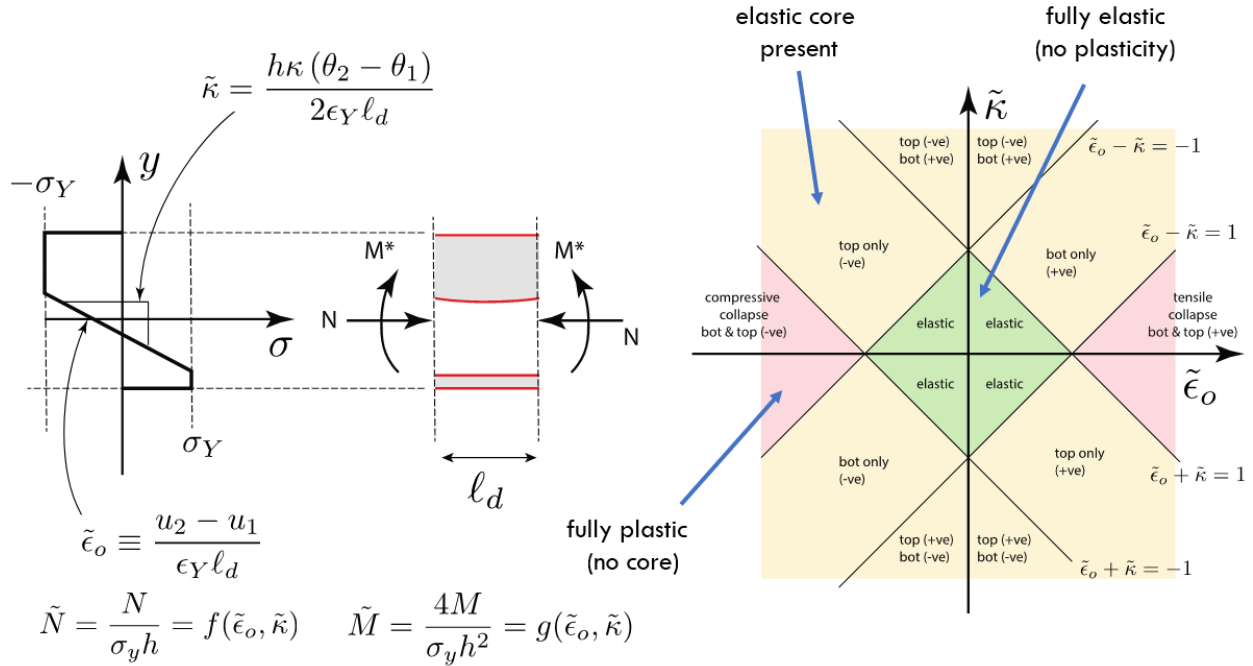


Figure 24. Structural yielding map showing combinations of stretch and curvature that lead to complete yielding of a beam element (without variations along its length, i.e. in a short notch). This can be used to identify limit loads and moments near notches. The notch height and width factors into the scaling of the defect element dimensions.

6.3 Results & Discussion

Plastic collapse refers to the scenario where the entire cross-section of the strut experiences yielding; the onset of plastic collapse depends on both applied force and applied moment. In the limit of zero moment, plastic collapse is governed by net-section yielding. In the limit of zero axial force, plastic collapse occurs when the applied moment reaches the collapse moment for

the beam, in which case the stress is completely compressive on one-half and complete tensile on the other. **Figure 24** shows a map of the relevant yielding regimes (e.g. yielding on one side, yielding on both sides, compression-tension yielding, etc.), along with the theoretical combinations of stretch and curvature associated with the transitions from one yielding state to the next. The green regions indicate purely elastic response; the red regions indicate scenarios where the stretch is large enough to cause complete net section yielding irrespective of moment. The yellow regions indicate deformation states in which an elastic core in the center of the strut remains; note that for sufficiently high curvature, a portion of the net section remains elastic.

Figure 25 shows the deformation map along with contours of the resultant force and moment associated with each deformation state (for one quadrant of the deformation map). Note that in the elastic region, force and moment are decoupled (as dictated by small deformation kinematics.) However, once yielding occurs, applied moments alter the resultant force and vice versa. For sufficiently large stretch (beyond the collapse limit) and small curvature, the resultants are again decoupled owing to the fact that complete collapse has occurred.

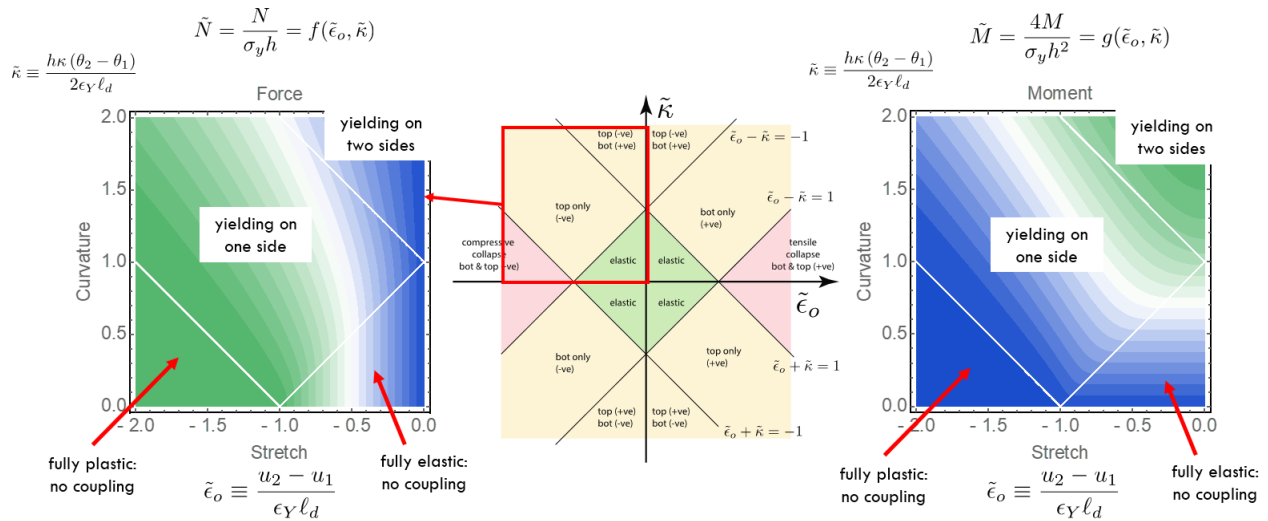


Figure 25. Contours of constant force (left) and moment (right) for compression loading of a notched struts, illustrating peak resultants than can be sustained once complete yielding has occurred. Complete analytical models were generated to predict resultants as a function of imposed strain. Note that the triangular regions of the bottom corners in the left and right figures correspond to the plastic collapse region indicated in red in the center figure.

Figure 26 shows resultant force for fixed applied curvature at various levels ranging from zero to finite values (left), and resultant moment for fixed applied stretch at various levels ranging from zero to finite values (right). The force-stretch curve with zero applied curvature is the expected bilinear response resulting from pure tension/compression of an elastic-perfectly plastic specimen. As applied curvature is added, the net force carried by the strut decreases, and is non-linear with respect to stretch deformation, due to the presence of the impose curvature. Likewise, the moment-curvature relationship with zero applied stretch follows the expected path, which is non-linear due to the gradual spread of the plastic zones induced by bending. The moment for a given curvature is reduced by the presence of imposed stretch, due to additional yielding; for

sufficiently high imposed stretch, no moment can be sustained until sufficient bending is imposed to unload one side of the strut (bottom curve on the right).

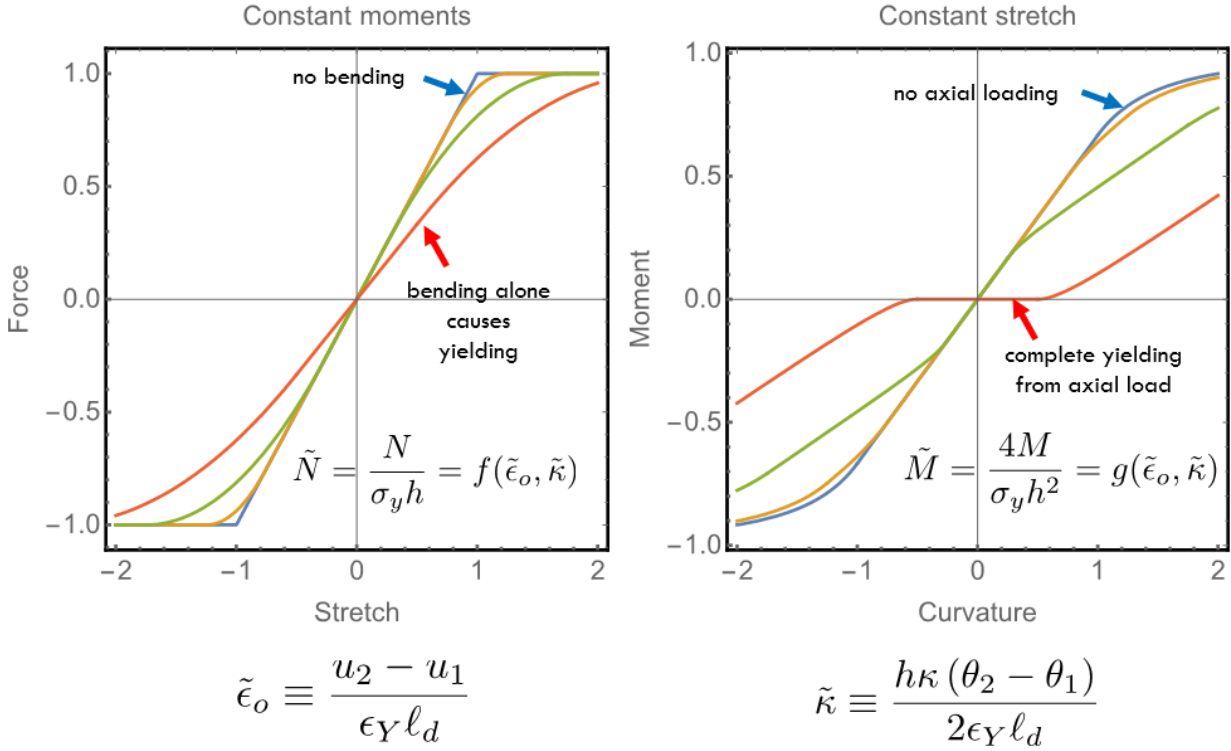


Figure 26. Force-stretch and moment-curvature responses for the notch defect element, assuming constant curvature (for stretch loading) or constant stretch (for moment loading). The curves illustrate the complex yielding behavior that results from combinations of stretch and bending. On the left, cases are shown with constant normalized curvatures of 0, 0.25, 0.5, 0.7 (traversing from blue to red); on the right, cases are shown with constant normalized stretch of 0, 0.25, 0.5, 0.75 (traversing from blue to red).

It is likely that in lattices, the imposed stretch and curvature will be proportional to one another, with a proportionality constant, α (ratio of bending to stretching), dictated by the cellular topology and imposed loading state. **Figure 27** shows the response of the strut in this scenario, i.e. the resultant forces and moments that result when stretch and moment are imposed in constant proportion. The proportion of bending to stretch is given by the constant α . An interesting feature is shown on the right; yielding induced by axial stretch (imposed in concert with curvature) will ultimately produce unstable moment-curvature relationships, wherein the resultant moment decreases with continued deformation. Under load control, this behavior would produce curvatures (i.e. bowing of the strut) that increase rapidly with continued loading. For sufficiently large deformations, this would quickly lead to post-buckling softening; large localized curvatures (i.e. at defect elements) would produce kinking. The subsequent geometry change reduces the axial force that can be carried by the strut.

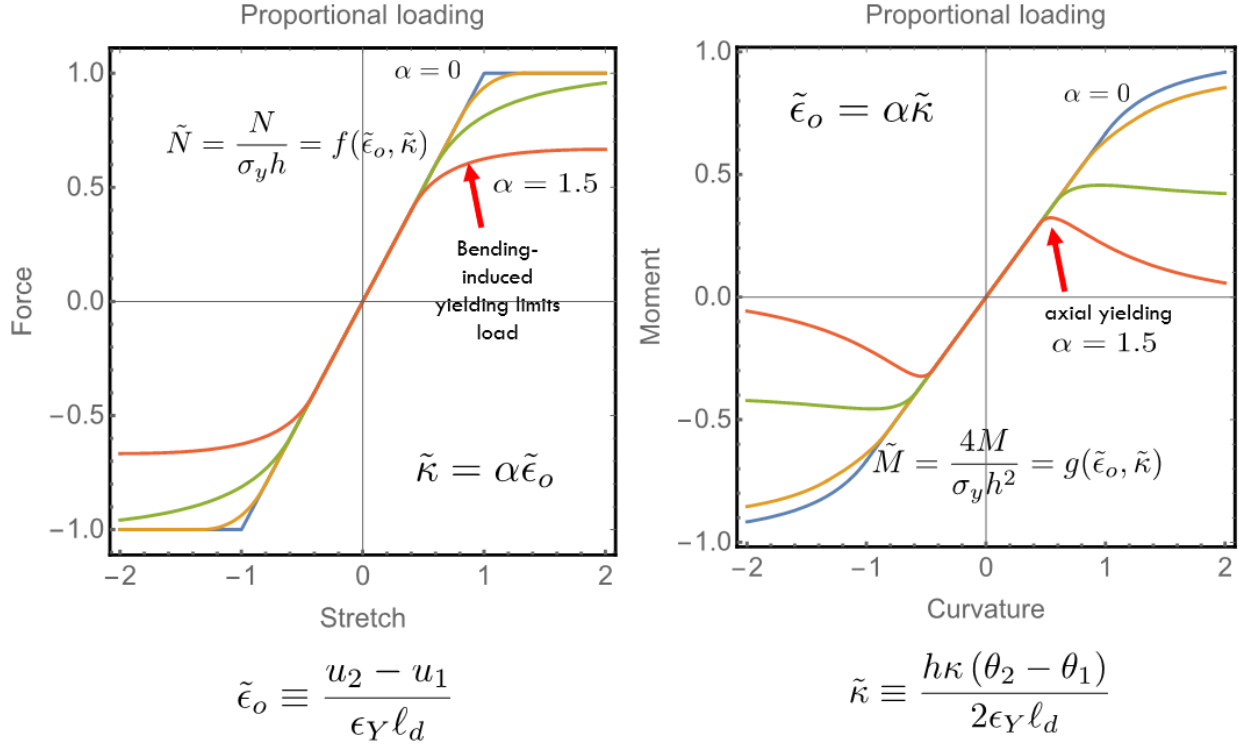


Figure 27. Force-stretch and moment-curvature responses for the notch defect element, assuming that curvature and stretch deformation are imposed at fixed ratio. The curves illustrate the complex yielding behavior that results from combinations of stretch and bending, include post-yielding (softening) induced by axial deformation in the presence of bending. Values of α are 0, 0.5, 1.0 and 1.5 (traversing from blue to red).

The model produces estimates for the plastic zone size as a function of imposed deformation, as shown in **Figure 28**. This should prove useful in guiding experimental characterization of deformation (e.g. DIC or x-ray scattering), since it provides an estimate of the physical extent of large deformations in terms of global deformations. Obviously, strut stretching that exceeds the yield strain produces net-section yielding (i.e. plastic zones that span the entire strut); in the limit of stretch beneath the yield strain, significant curvatures are needed to drive the plastic zone to significant fractions of the strut size. **Figures 29** and **30** illustrate the evolution of the plastic zones with respect to result moment and force, both for fixed deformation (**Figure 29**) and for proportional loading (**Figure 30**). It is interesting to note that the decrease in moment with applied curvature occurs prior to complete net section yielding; i.e. at the onset of bending instability, an elastic core remains. This suggests that experimental observations of plastic zones at the onset of lattice collapse will be challenging, due to the likely needed resolution.

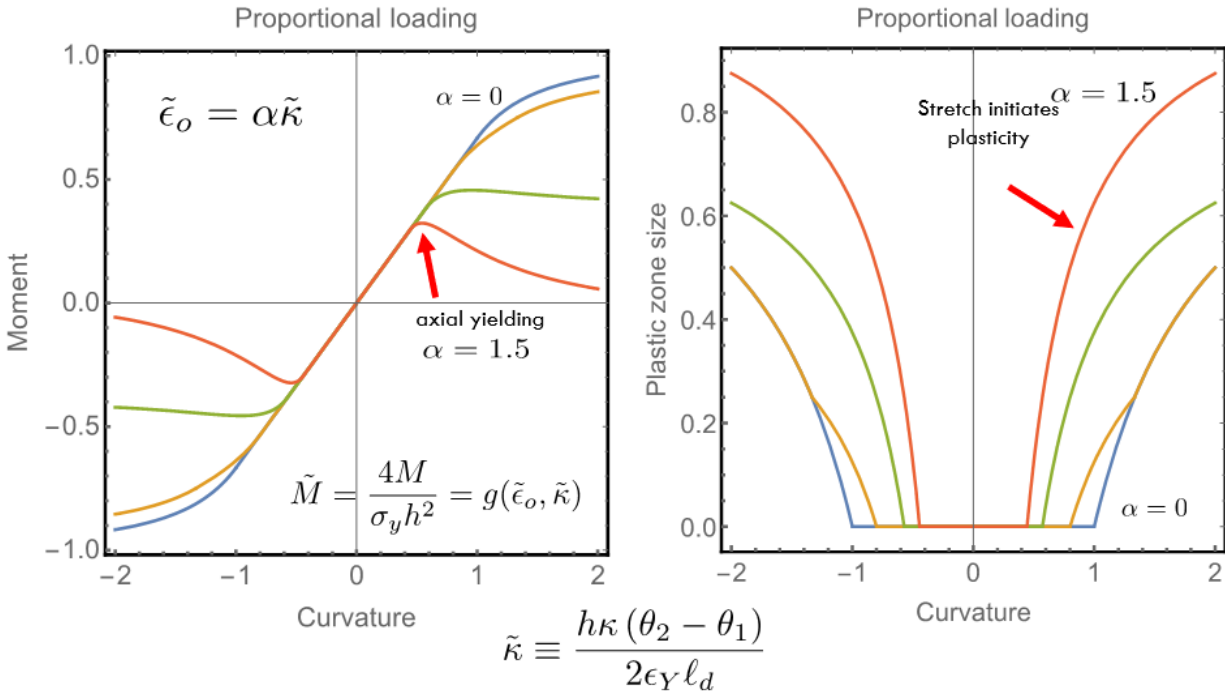


Figure 30. Moment-curvature relationship with proportional stretch imposed, illustrating the size of the plastic zone at various combinations of stretch and bending. For sufficiently high stretch with imposed bending, stretching initiates and drives the size of the plastic zone on either side of the notch.

6.3 Key Outcomes

- The value of the analytical defect element described here lies in understanding the nature of force-moment coupling and the identification of the scaling controlling limit loads and plastic zone sizes, for materials that exhibit low levels of strain hardening.
- Ultimately, a conventional elastic-plastic beam element in commercial codes will capture the exact same behavior, with several additional features that make it more favorable. First and foremost, such elements are capable of accounting for elastic unloading (which has not been added to the description above). Second, conventional beam elements capture the effect of shear forces, which are likely important in post-buckling behaviors triggered by decreasing moment capacity. Finally, conventional beam elements use linear or quadratic descriptions of rotation along the beam axis (while the above assumes it is constant), which accounts for the spread of plasticity in the axial direction, such behavior is likely inconsequential. Highly localized deformation near a small defect imply that axial gradients in the defect region are negligible, and hence this latter effect is likely inconsequential.
- As shown in **Figure 23**, it should be kept in mind that using conventional beam elements with reduced area to account for the depth of the defect still requires that the element be offset from the main strut axis; this is described in more detail in subsequent sections of this report.

7. FEA SIMULATIONS OF PRIMITIVES USING CONVENTIONAL BEAM ELEMENTS

7.1 Overview

This section describes FEA analyses of primitives using conventional beam elements, subject to various constraint conditions at the ends of the struts; the motivation for the study was to evaluate the efficacy of lattice modeling approaches that do not explicitly account for strut surface defects or plasticity within nodes (strut intersections).

Conventional beam elements that share nodal degrees of freedom enforce rotation and displacement continuity between connected elements. Hence, the initial angles formed by strut intersections (in the undeformed state) remain constant through the simulation; the global orientation of the node can experience large rotations, but the angles between connect struts do not change. In this regard, such simulations cannot account for plasticity in intersection material that may reduce the stiffness of strut connections. In essence, the analyses represent the simplest approach to simulating cellular materials, and discrepancies with experiments provide insight into additional deformation modes that are needed to capture the complex state of deformation within a lattice.

Simulations were conducted for Node A, Node B and Cell B shown in **Figure 5**; the simulations spanned a variety of boundary conditions for strut ends adjacent the loading platens, strut dimensions, and strain hardening descriptions.

7.2 Methods

The modeling approach is shown schematically in **Figure 31**. Node A, Node B and Cell B specimens were approximated using elastic-plastic beam elements using ABAQUS, with each strut broken into multiple B21 elements. Convergence studies revealed identical behaviors when ten or more elements were used in each strut. All analyses were conducted in displacement control, and included large deformation kinematics, which account for large rotations and capture buckling behaviors. Global resultant loads on the specimens were computed by summing the appropriate reaction forces from nodes with imposed displacements.

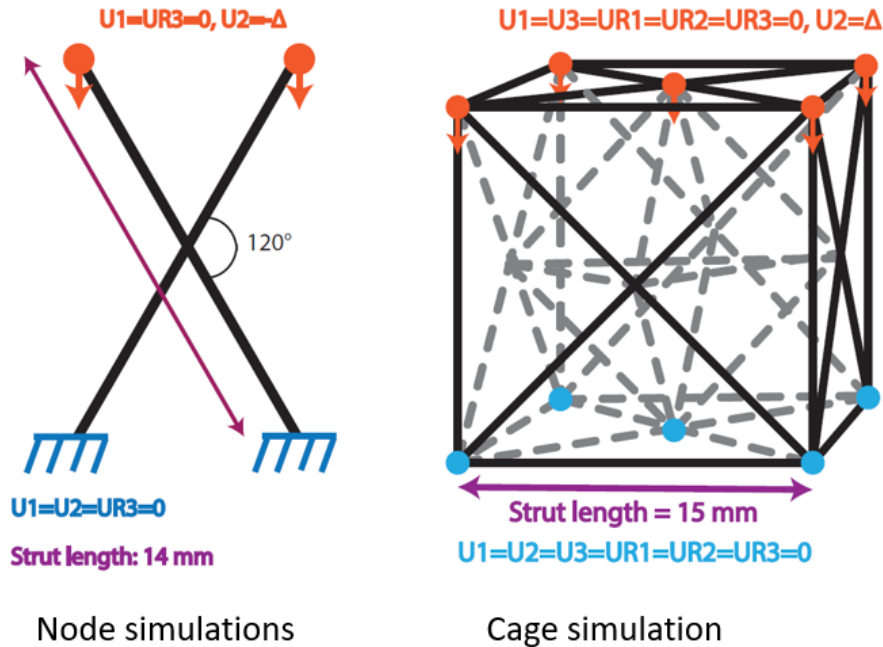


Figure 31. Schematic overview of modeling strategy using conventional beam elements; the nodes connecting struts are essentially rigid, such that the simulation preserves angles between struts. Essentially, on the struts themselves can yield and contribute to softening behavior.

Both implicit and explicit approaches were adopted, as convenient: implicit analysis were significantly faster, but occasionally failed to converge (with respect to load incrementation) due to post-buckling collapse of the structure. Explicit analysis was slower, but in all instances provided convergence with respect to load incrementation. With either method, complete convergence analyses were conducted to ensure that incrementation parameters did not influence the results. Implicit cases that ran to completion provided identical to corresponding explicit analyses over the range of where both approaches produced converged solutions.

A range of boundary conditions were explored both to establish their impact on response, and to mimic several experimental boundary conditions. For the Node A and Node B specimens, experiments were conducted with three ‘grip’ techniques. In the first, denoted as “rigid”, the thick connecting section of the specimen near the platens (see **Figure 5**) was left intact and glued to the loading platens, effectively eliminating out of plane rotation. In the second, denoted as “free rotation”, the thick connecting section was left intact but was not glued to the platens, allowing out-of-plane deformation via rotation. In the third, denoted “sliding”, the thick connecting section was cut between the struts, and teflon tape was used between the resulting thick sections and platens. The “rigid” case was modeled by constraining lateral displacements and all rotations to be zero. The “free rotation” case was constrained lateral sliding and in-plane rotation, but out-of-plane rotations at the grips were allowed. In the “sliding” cases, lateral displacement and out-of-plane rotation was allowed to occur, while in-plane rotation was fixed to be zero.

7.3 Results & Discussion

A comparison of primitive experiments and representative simulations is shown in **Figure 32**. In this figure, the blue and black cage schematics illustrate the position of a center strut that runs from the center of one face to the opposite face; this is the only asymmetric strut in the cage design. (The asymmetry of the cage design is difficult to see from images due to strut crowding.) The simulations in this figure correspond to assuming nominal dimensions for the struts, and elastic-perfectly plastic behavior with a yield stress equal to wrought Ti64 (880 MPa). In all cases, the FEA analysis produced stiffer, stronger responses than those seen in experiments. (This is true irrespective of specimen type and boundary conditions.) To determine if this was a consequence of material hardening, a complete suite of calculations was run with various level of hardening using a bilinear strain hardening relationship.

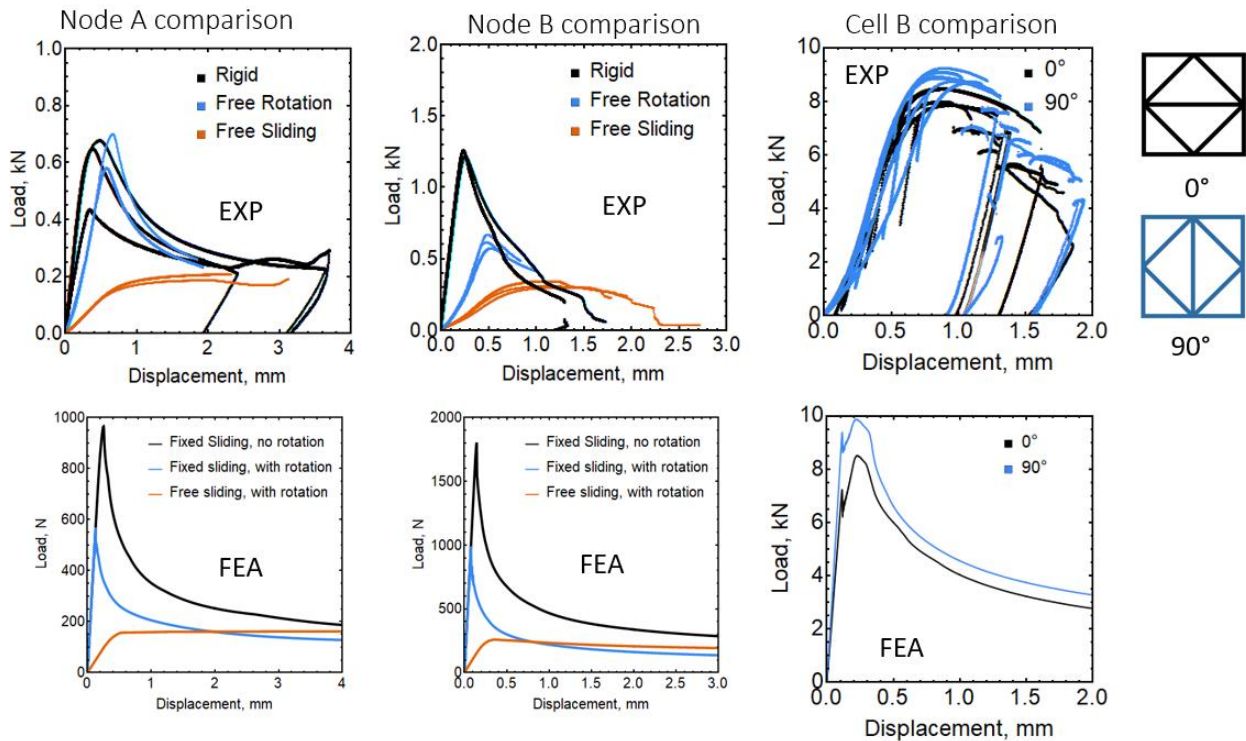


Figure 32. A comparison of tests and modeling with conventional beam elements with nominal dimensions, for nodes subjected to various end/platen conditions and cages subjected to frictionless platens. The FEA consistently overestimates the stiffness and peak load of the structure, due to the fact it does not account for plasticity in the nodes connecting the ends of the struts.

Figure 33 compares several simulations with conventional beam elements for Cell B, with various levels of strain hardening and different constraints used for the nodes at the platens. As expected, neither strain hardening nor rotation constraints for end nodes impact the initial stiffness; further, the impact on peak load is marginal. Including either strain hardening or added constraints for the end nodes produces more stable post-buckling behavior, i.e. higher loads for a given imposed displacement. Clearly, neither of these modeling choices (hardening or boundary

conditions) brings the predictions significantly closer to the observations shown in **Figure 32**; indeed, the net effect is comparable to the change in orientation of the cell, i.e. the center strut in Cell B which runs in only one direction.

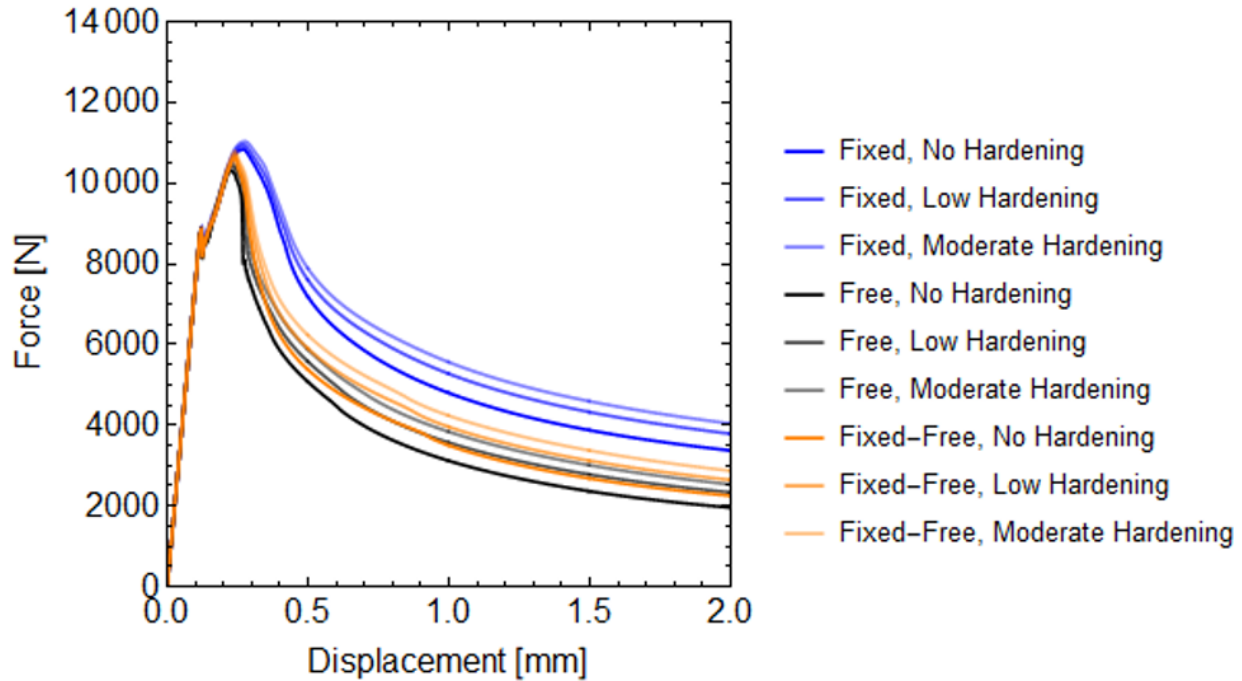


Figure 33. *A comparison of simulations with conventional beam elements with nominal dimensions (1.25 mm diameter struts) with various end conditions and various hardening rules; the results demonstrate that no amount of hardening or lack of constraint (due to platen sliding) can account for the discrepancies shown in Figure 32.*

Figure 34 illustrates that geometric differences between nominal geometry and as-printed geometry also do not rationalize difference with experiments. In this figure, the blue curves correspond to nominal geometry, while the black curves correspond to the average cross sectional size determined from CT experiments. The gray shaded region corresponds to minimum and maximum areas determined from the CT. While not shown, additional simulations with orientation-specific sizes were also conducted; these fall within the shaded regions shown in **Figure 34**. This is not surprising, given that simulations with all struts having maximum or minimum area will bracket the response of a strut with mixed strut sizes.

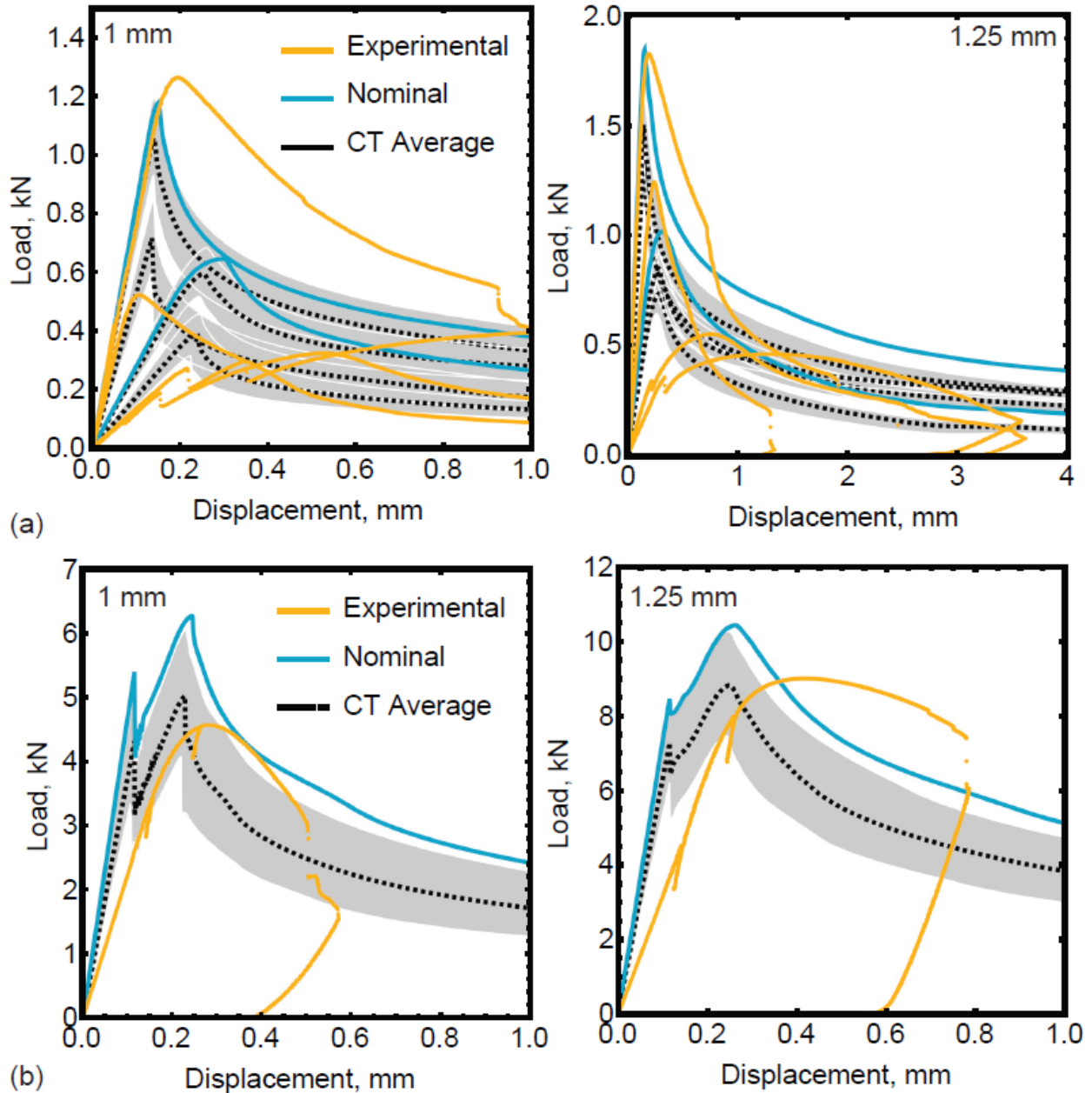


Figure 34. Effect of strut dimensions on predictions, with experiments: Load displacement curves from a FEA beam model compression test of a node as compared to the experimental results with nominal strut diameter of (a) 1 mm and (b) 1.25 mm. The solid line indicates the results using a cross-sectional area based on the nominal diameter while the shaded region has bounds using the maximum and minimum cross-sectional areas of inscribed ellipses based on the CT scan shown in Fig. 2b. The dashed line indicates the result using the average cross-sectional area of an inscribed ellipse from the CT scan. Similar results are shown for a FEA beam model of a cell compression test shown with nominal strut diameter of (c) 1 mm and (d) 1.25 mm.

7.4 Key Outcomes

- The clear implication from **Figure 34** is that strut behavior, independent of plasticity that may occur within the nodes (strut intersections) is not sufficient to ensure agreement with measured response.
- In all instances, the conventional beam element approach is stiffer than measurements. In most cases, the predicted peak strength is stronger (with the exception of Node B response with clamped conditions, where the agreement is close); in all cases, the load carrying capacity of the structure after peak load is greater than that predicted via conventional beam elements.
- In essence, conventional beam elements fail to capture the effect of local yielding near strut intersections and near stress concentrations caused by surface defects. This local yielding leads to softer behavior prior to the onset of peak loads, where plastic zones spread to cover entire struts and strut intersections. Strain hardening in these localized regions likely strengthens the post-peak response and delays the onset of plastic collapse. This hypothesis is tested in the next section.

8. FEA SIMULATIONS OF SURFACE DEFECTS IN STRUTS

8.1 Overview

This section describes FEA analyses of struts with surface defects, defined as rounded notches with various depths and widths, as shown in **Figure 35**. Two different FEA-based approaches were taken: (i) fully two-dimensional analyses with either plane stress or plane strain conditions, and (ii) beam-based analyzes where the defect is modeled using a beam element with reduced cross-section that is off-set from the main strut axis. The goals of the study are (i) to determine the impact of surface defects (typical of printing) on strut behavior, and (ii) establish the efficacy of using highly efficient beam elements to capture the impact of such defects.

In this section, the fully 2D FEA model is used as the ‘ground truth’, since these simulations capture strain concentrations near notches and the gradual spread of plastic zones around the notch. Comparisons are made between these simulations and equivalent beam based methods for a wide variety of loading conditions (i.e. applied rotations and stretch at the ends of the strut), defect geometry (i.e. depth and width) and defect location (relative to the end of the struts). An important outcome in this section is that strut defects are not the only feature contributing to the macroscopic response.

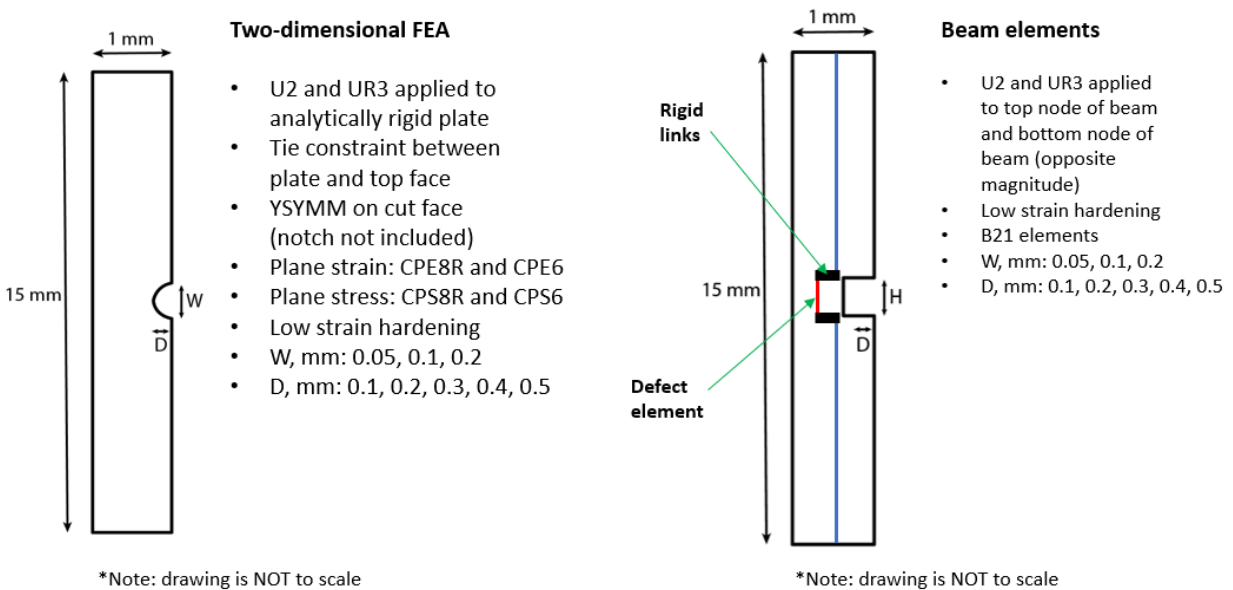


Figure 35. Schematic overview of the modeling of defects in struts; a notched strut is analyzed under compression and end rotation (in various combinations), using both 2D plane stress FEA (fully resolving behavior near the defect) and a beam element approach that reduces the net section of the strut at the location of the defect. Localized plastic deformation in the reduced section is an approximation to the plastic zone that develops in the notch.

8.2 Methods

The modeling approach is shown schematically in **Figure 35**; in fully two-dimensional FEA, the notch is modeled as a surface defect with straight sides and a rounded tip whose diameter is equal to the notch width. Planar rotations and uniform vertical displacements are applied incrementally to the ends of the strut in constant proportion, analogous to the ‘proportional loading’ cases described in Section 5. Nodal reaction forces are used to compute the resultant moment and forces in a post-processing step. Complete convergence studies were conducted to ensure the extracted results (i.e. force/moment resultants and plastic zone sizes near the notch) do not depend on the details of the finite element mesh. For the 2D FEA, element types CPS8R and CPS6 were used with ~2200 elements; computation times were on the order of ten minutes.

For the beam element cases, numerous beam elements were used above and below the location of the defect (or notch); at the notch, a single beam element connected the two defect free segments of the strut, with an offset to reflect the shift in the neutral axis caused by the notch. B21 elements were used with a rectangular cross-section and each simulation typically used 21 elements. Complete convergence studies were conducted to ensure that the number of beam elements in the intact strut (above and below the defect element) did not influence the results.

The single, reduced-area beam element is referred to as the ‘defect element’; various dimensions of the defect element were analyzed to determine properties that match the spread of plasticity in the 2D analyses and capture the resultant behavior at the grips (i.e. ends of the strut.) The ends of the ‘defect element’ are connected to the intact portion of the strut using a rigid link (aligned with the notch direction) that enforces displacement and rotation continuity with the ends of the intact portions of strut meeting the defect element.

The use of a B21 beam element as the defect element enforces a linear variation of shear deformation, stretch and curvature in the axial direction of the strut; for an intents and purposes, the defect element experiences constant deformation in the axial direction, and at least in this regard, behaves virtually identically to the behavior described in Section 5.

8.3 Results & Discussion

A summary of the response from the 2D FEA analysis is shown in **Figure 36**, showing the impact of a center, single sided notch of various dimensions, subject to plane stress and plane strain conditions. As expected, the plane strain simulations show 10-15% higher loads for a given deformation state, due to the additional constrain of zero out-of-plane deformation. The notch widths shown in **Figure 36** correspond to roughly one and four diameters of the powder (a reasonable estimate for surface defects in EBM printed struts/walls).

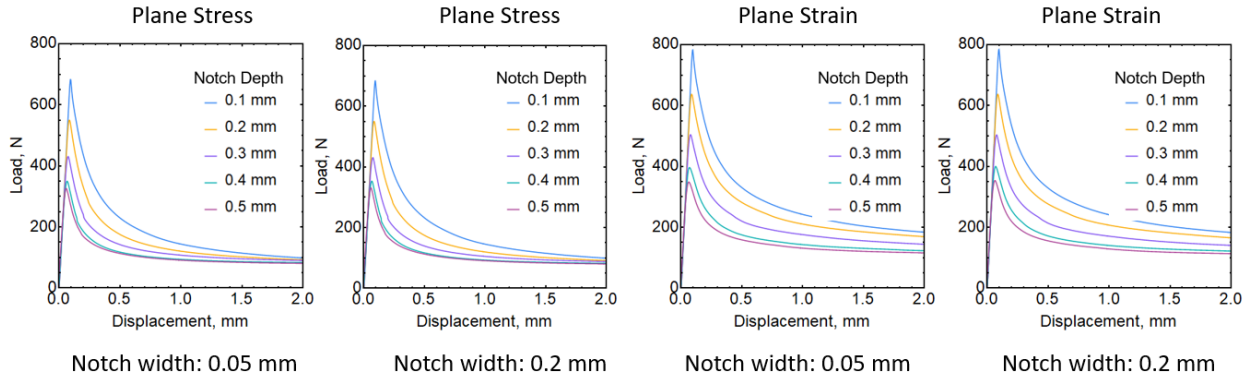


Figure 36. *Effect of notch dimensions on the compression/rotation response of a strut with a defect, for full 2D FEA to model the defect. The notch depth dominates the results, with notch width having little impact on the response in this range of widths, which correspond to sharp notches consistent with micrographs of surface defect. Plane strain calculations are somewhat stiffer than plane stress, owing to the additional constraint of zero out-of-plane straining.*

The notch height has relatively little effect, due to the nature of plastic localization at the tip of the defect; the plastic zone induced by the presence of the notch grows quickly after the onset of initial yielding and spreads across the entire remaining ligament. The axial extent of the plastic zone is typically one-half of the strut thickness, regardless of the notch height. To control the direction of buckling and facilitate post-processing, the struts were initially displaced laterally by a small horizontal displacement (i.e., half the notch depth) and then they were compressed by 2 mm. The initial horizontal displacement was to ensure notch opening upon compression. The peak loads observed in **Figure 36** correspond to the collapse load for net-section yielding; hence, the peak load can be predicted from notch depth according to simply net-section calculations of load capacity.

Vertical loads drop precipitously once net yielding occurs, due to outward buckling induced by the hinge formed at the notch. This precipitous drop is more dramatic than in the case of a single uniform strut (i.e. that of Section 5) due to the presence of the beam elements above and below the notch, which allow for greater lateral motion of the section containing the plastic hinge (i.e. the localized yielding at the notch).

A comparison of the two-dimensional FEA and defect element approach are shown in **Figure 37**, for a proportional loading ratio of 1 radian of face rotation per 1 mm of axial displacement. Both force-displacement and moment-rotation are shown, with the quantities taken from the ends of the strut. It should be emphasized that this behavior is more complicated than that of a completely intact strut (i.e. Section 5), owing to the formation of the plastic hinge at the defect and the additional moment arms provided by the intact strut both above and below the hinge. The effect of using different defect element heights is also shown. The most effective approach is to use a defect element length that is comparable to the notch; despite the spread of plasticity away from the notch plane in 2D FEA, additional defect height along the axis of the beam (moving away from the defect) is not needed to capture the macroscopic response of the strut with a

defect. Simply put, plasticity localizes in the defect and spreads only a very small distance along the strut direction.

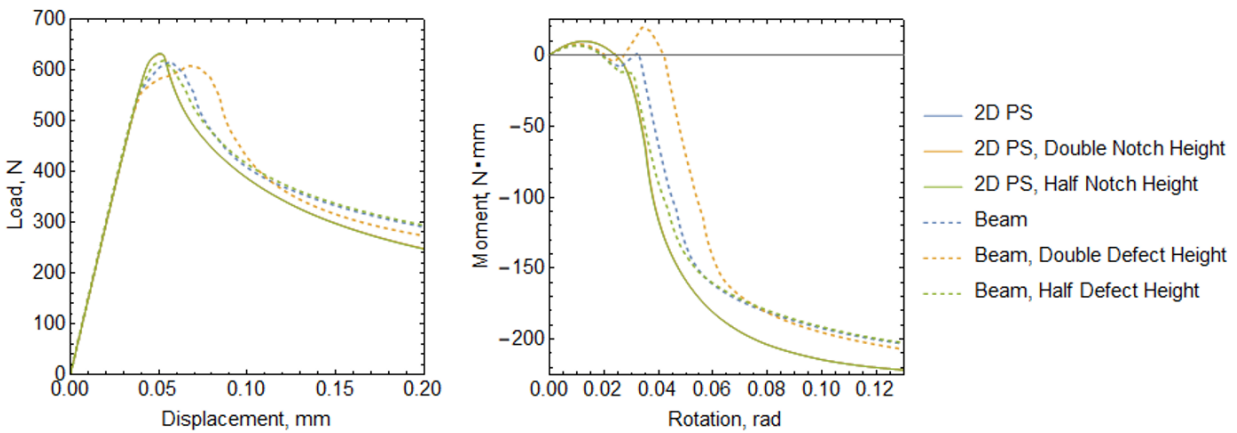


Figure 37. A comparison of 2D FEA (fully resolved plastic zone at the notch) and beam element approach to modeling surface defects; resultant loads and moments are extracted from both models. The beam element results are a fair approximation to the global force displacement response of the strut with a defect. Complex moment responses are a function of whether or not the next section yields in compression prior to rotation. Defect is loaded at the center of the strut.

The somewhat complicated moment-rotation response near the onset of yielding is a consequence of the fact that the notch may open or close during early stages of yielding, then switch when the hinge softens and the bending resistance is limited by the presence of a large plastic zone. That is, the notch may close at early stages of deformation, then begin to open again at later stages of deformation. Whether or not the defect opens or closes with initial applied loading is a function of the proportionality constant that defines the relative contribution of compression and bending; **Figure 38** shows a map indicating the initial deformation mode associated with defects of various depths. The degree of rotation needed to produce an opening mode at the onset of plasticity increase with notch depth; this is because large notches yield in compression prior the development of significant bending (that acts to open the notch).

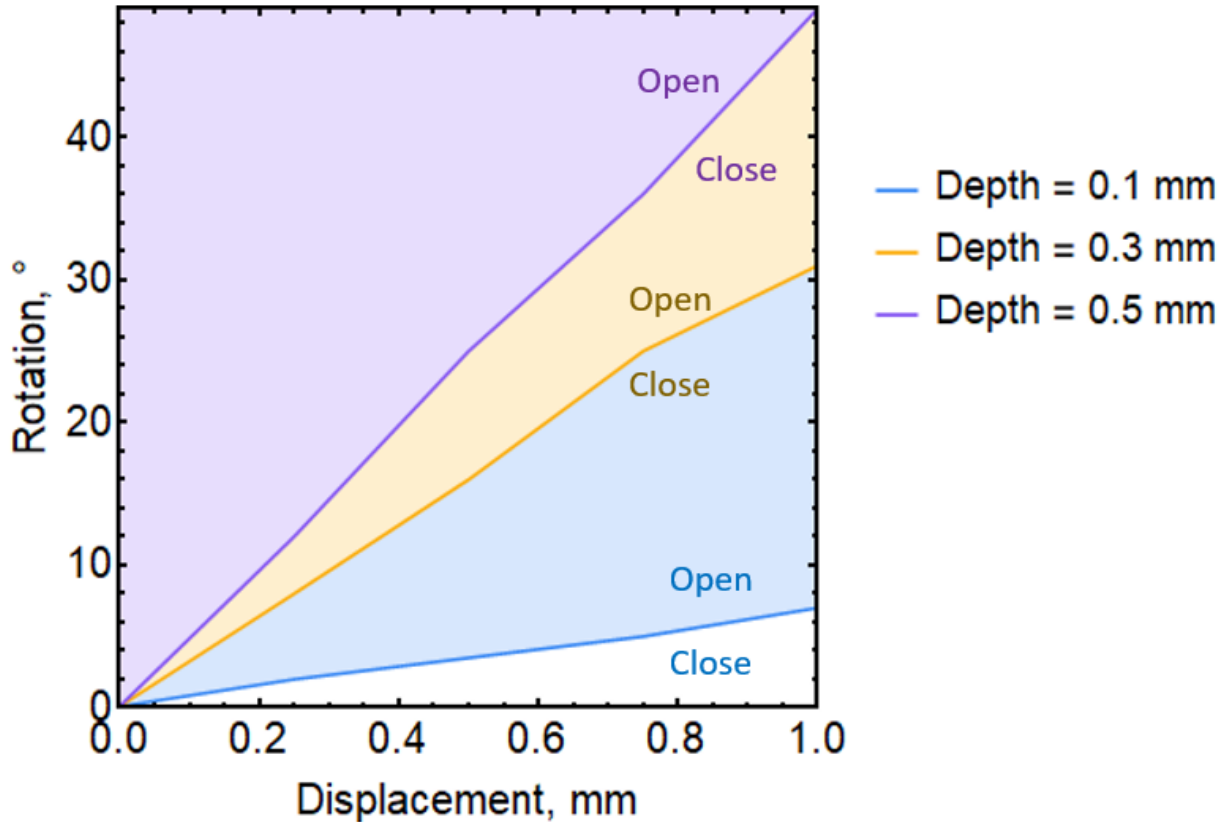


Figure 38. A map of notch closure as a function of end displacement and end rotation; for a given notch depth, combinations above the boundary indicate that the strut will bend to open the notch, while those below indicate that compression of the strut closes the notch prior to significant bending deformation (that would otherwise open the notch).

Figure 39 shows the quality of agreement between the two modeling approaches for notches of various depth. **Figure 40** shows the quality of agreement between the two modeling approaches as a function of the proportionality constant that controls the relative amounts of applied rotation and compression. All of the results indicate that very good agreement is obtained prior to the occurrence of large rotations; after large rotations occur, the beam element underestimates the resistance of the hinge.

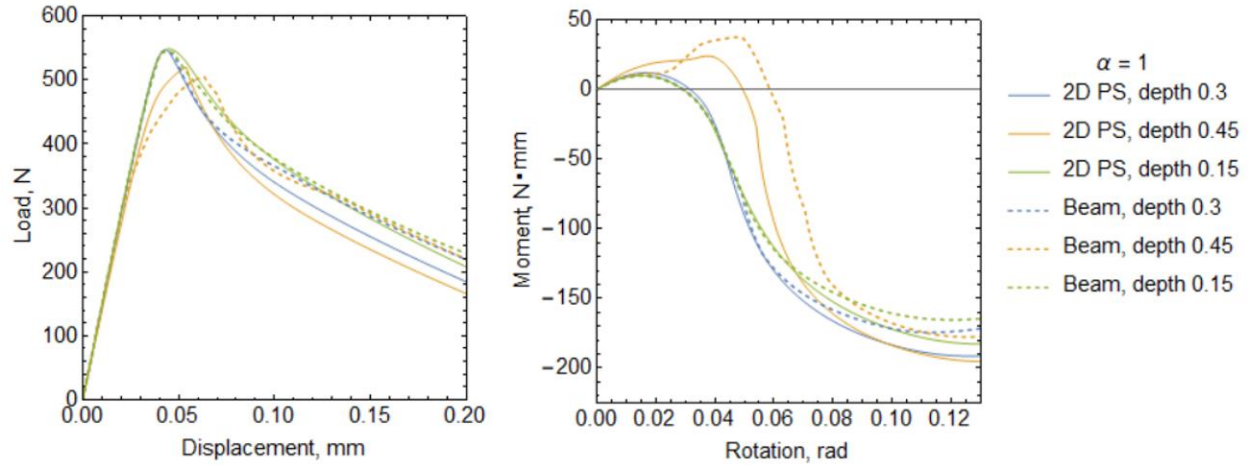


Figure 39. A comparison of full 2D FEA with beam element defect approach, for equal amounts of compression and rotation and several different notch depths. Generally, the beam element defect approach tracks the trends of the full FEA across a range of defect sizes, with larger discrepancies at larger defect sizes. Defect is located at the center of the strut.

This is likely a consequence of elevated hardening near the notch; that is, along a cut through the notch, the 2D FEA will capture the effect of strain concentration from the notch geometry, while the beam element will not. This effect is explored further in the analysis of nodes described in the next section. Finally, **Figure 41** compares the response of the two modeling approaches for notches at various axial locations in the strut. The results show that the agreement is consistent across a broad range of notch location and depth.

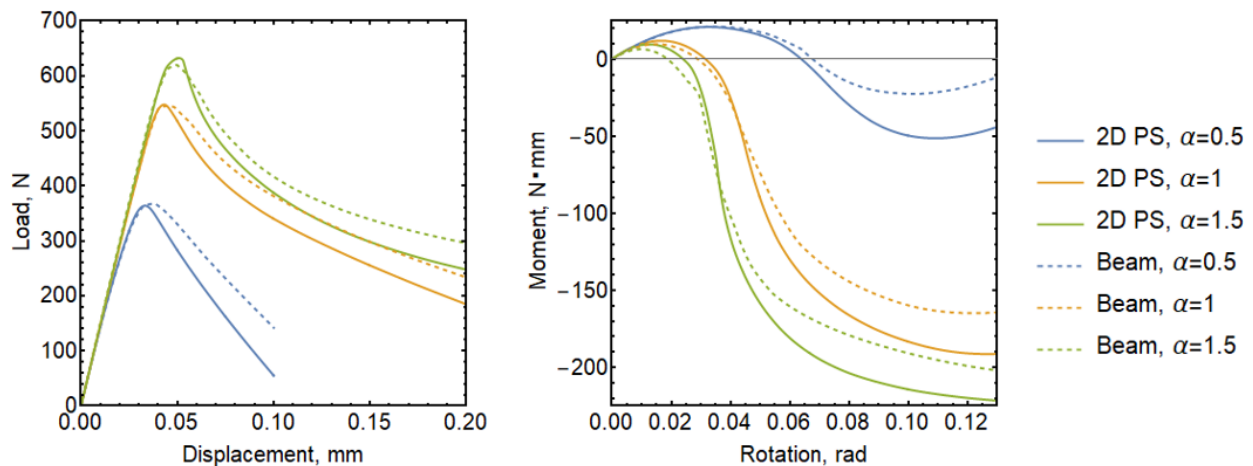


Figure 40. A comparison of full 2D FEA with beam element defect approach, for differing amounts of compression and rotation. Generally, the beam element defect approach tracks the trends of the full FEA across a range of proportional loadings, with larger differences once the net section near the defect has gone fully plastic.

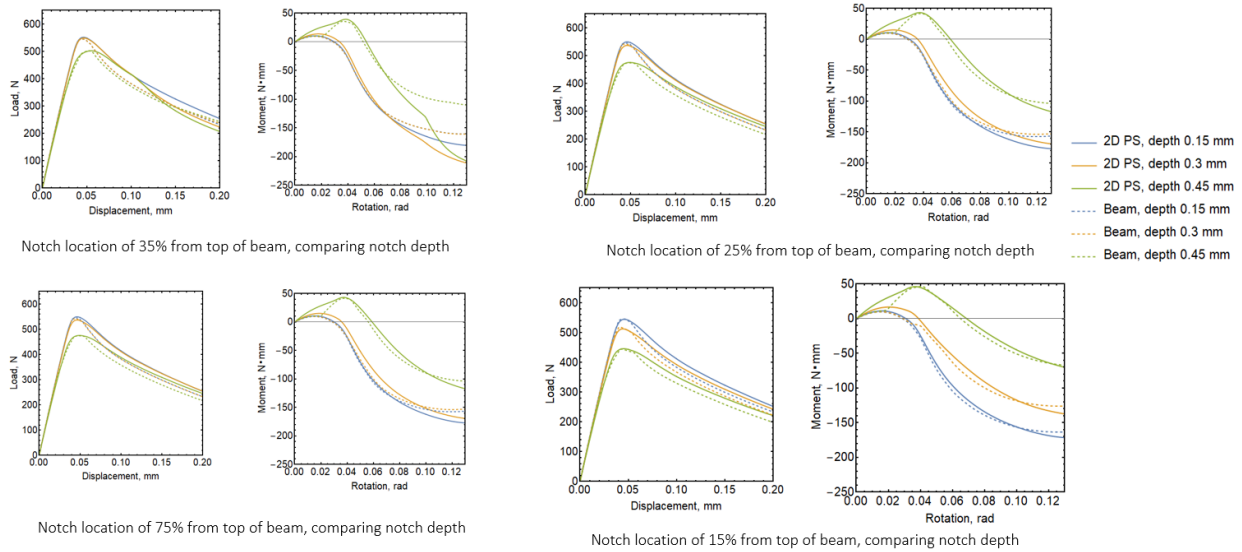


Figure 41. A comparison of full 2D FEA with beam element defect approach, for purely proportional loading (equal amounts of end rotation and compression), across a range of defect locations (relative to the end of the strut) and defect depths. The beam element approach does an excellent job of capturing the behavior regardless of notch depth and defect location.

8.4 Key Outcomes

- The modeling of surface defects with beam elements that account for the eccentricity introduced by the defect is a promising pathway to avoid the expense of full 2D analysis near notches, as it provides a reasonably accurate description of changes in the load/moment-stretch/curvature relationships prior to large rotations.
- The dominant effect of a surface defect on the strut is the formation of a plastic hinge that lowers the stretching and bending stiffness of the strut; this plastic hinge spreads from the notch tip to the opposing face of the strut over a narrow range of global deformation imposed on the strut. The extent of the plastic zone is limited in the axial direction, and is typically on the order of or smaller than the strut thickness.
- The defect element approach creates a potentially powerful opportunity to quickly assess the impact of defects in notches as a function of their size and location; future work will use this approach to map the sensitivity of lattice structures to distributed defects.

9. FEA SIMULATIONS OF STRUT INTERSECTIONS (NODES)

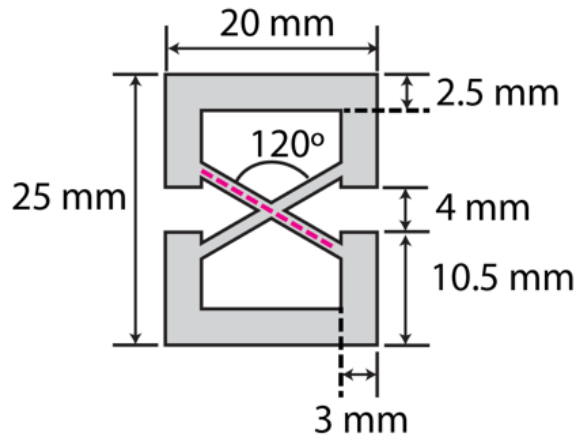
9.1 Overview

This section describes FEA analyses of intersecting struts, with the goal of rationalizing the observation that lattices are more compliant, weaker (in terms of peak load) and ductile (i.e. exhibit larger load capacities at large deformation) than expected from elementary models of truss-based structures. While a myriad of printing relating factors may play a role (such as local differences in material structure), the focus was on establishing the role of plasticity in strut connections (nodes) in overall macroscopic response.

To gain insight into this behavior and establish efficient modeling techniques, fully resolved two-dimensional FEA and beam-based models were used to quantify the nature of plasticity in nodes and establish a baseline for beam-based modeling approaches. These studies encompassed a broad range of node geometry (i.e. angles of intersecting struts) and strain hardening behaviors (to capture the effect of strain concentrations near strut intersections). The goal of this study was to establish the role of global structural plasticity at nodes in lattices; future work can build on this foundation to include printing-related features at smaller scales.

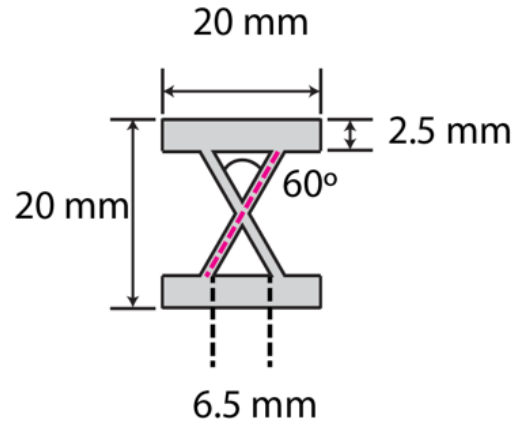
9.2 Methods

The structures shown in **Figure 42** were analyzed in plane stress, for two different end conditions, which influence the direction of forces directed toward the node, as well as several different strut angles. Full convergence studies were conducted to ensure the results were mesh independent. CPS8R and CPS6 elements were used with between 30,000 to 40,000 elements per structure. Boundary conditions imposed were encastre (in-plane rotation not allowed at frame ends, UR3 = 0). Pinned BCs (in-plane rotation allowed at frame ends, UR3=unset) were also tested but they resulted in the same result as the encastre BCs. Simulations were run with fillet radii at the strut intersections ranging between 0 and 100% of the strut diameter, with little effect.



Strut length: 16 mm

Strut diameter: 1 mm



Strut length: 16 mm

Strut diameter: 1 mm

Figure 42. Schematic illustration of Node B specimens in two different orientations, used to study the effect of yielding at the node (strut intersections). Both 2D FEA (plane stress) and beam element approaches were studied to determine effective means to capture nodal deformations without resulting to full FEA.

These simulations were compared with a beam-element approach which accounted for plasticity in the node using a ‘box’ of beam elements representing the material within the strut intersections. A variety of beam-box geometries (size and shape) and strain hardening descriptions were explored to establish efficient low-order beam-based modeling approaches for nodes.

9.3 Results & Discussion

Figures 43-48 illustrate various features of the plastic response near strut intersections as a function of compressive displacements applied to the top of the frame (while the bottom is held fixed). In comparing **Figure 43** and **Figure 44**, one can see that the development of nodal plasticity depends strongly on the angle formed by the struts, which alters the distribution of forces impacting the node. In general, low angle nodes (i.e., **Figure 43**) that are subjected to lateral constraint experience more widespread yielding that encompasses both the nodes and the adjacent struts. In contrast, high angle struts experience preferential yielding of the node prior to yielding in the struts (away from the nodes). **Figure 45** and **Figure 46** illustrate that at peak loading, the plastic zone encompasses the entire node; the largest plastic strains are associated with the direction with maximum axial force translated from the adjacent struts. That is, in the high angle struts in **Figure 46**, the maximum plastic strain component is in the vertical direction; conversely, for the low angle struts in **Figure 45**, the maximum plastic strain component is in the horizontal direction, as constraint against lateral expansion squeezes the node in that direction.

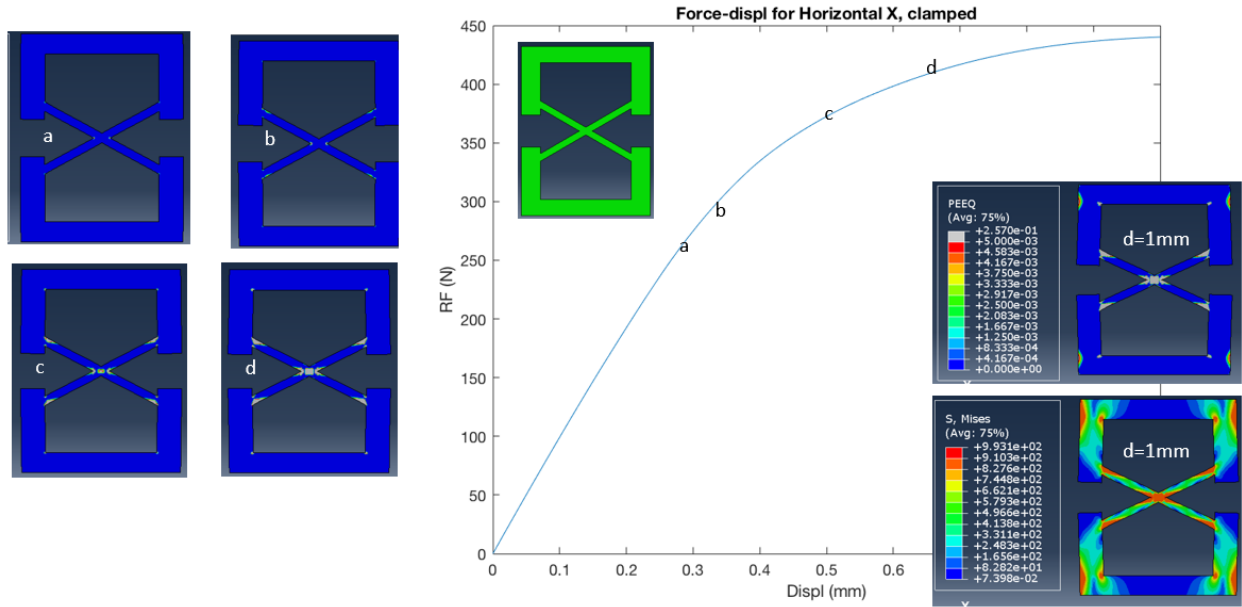


Figure 43. Full 2D FEA predictions of the load-displacement response for Node B in compression, showing the evolution of plastic zones at the ends of the struts and in the center node. Yielding of the node section controls the peak load in the structure.

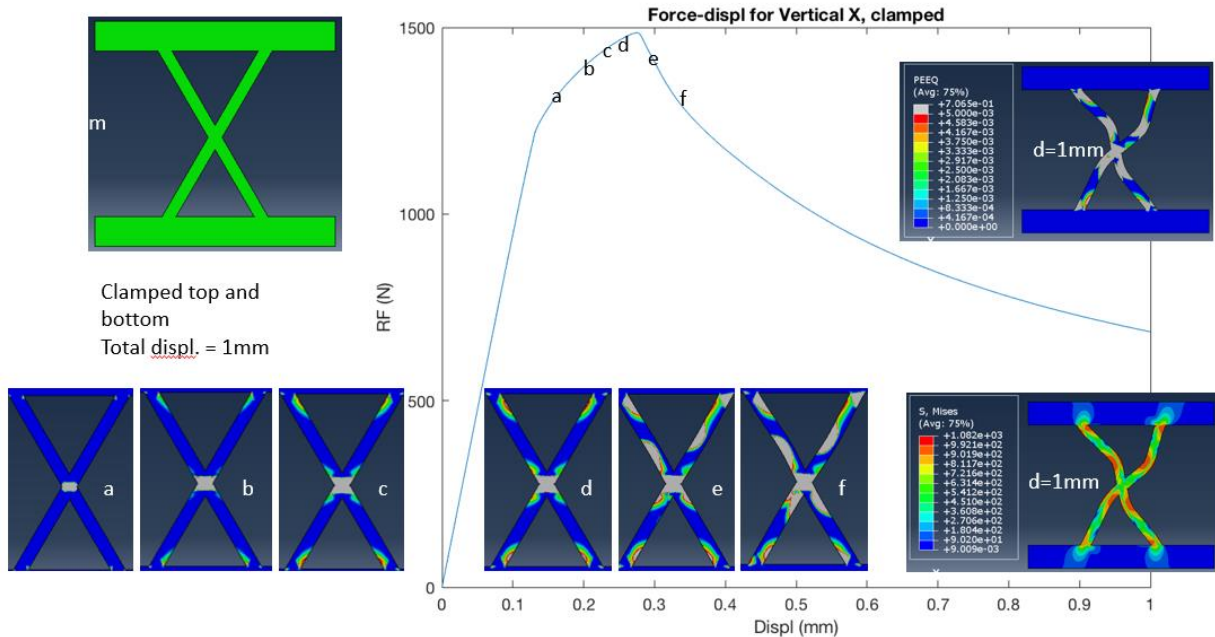


Figure 44. Full 2D FEA predictions of the load-displacement response for Node B in compression rotated 90 degrees from Figure 43, showing the evolution of plastic zones at the ends of the struts and in the center node. Yielding of the node section controls the peak load in the structure. Note that the deformed shape is virtually identical to one of the images shown in Figure 10.

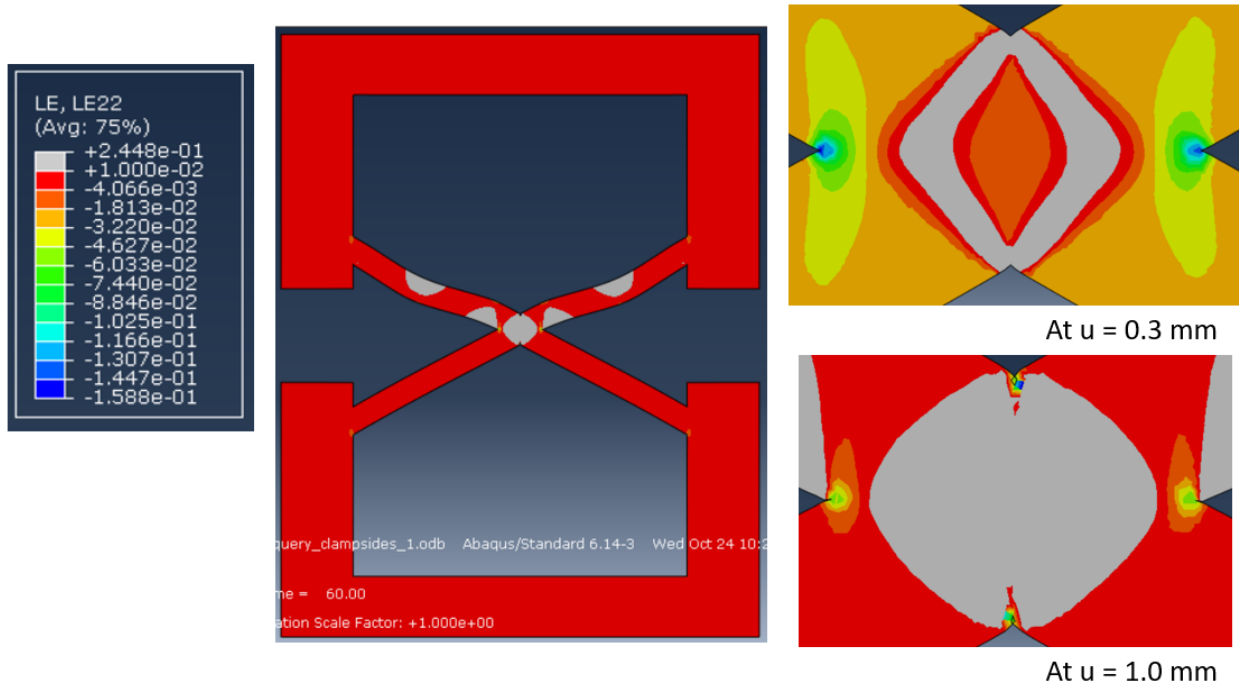


Figure 45. Full 2D FEA predictions of the evolution of plastic zones at the ends of the struts and in the center node. Yielding of the node section controls the peak load in the structure. Note that the deformed shape is virtually identical to one of the images shown in Figure 10.

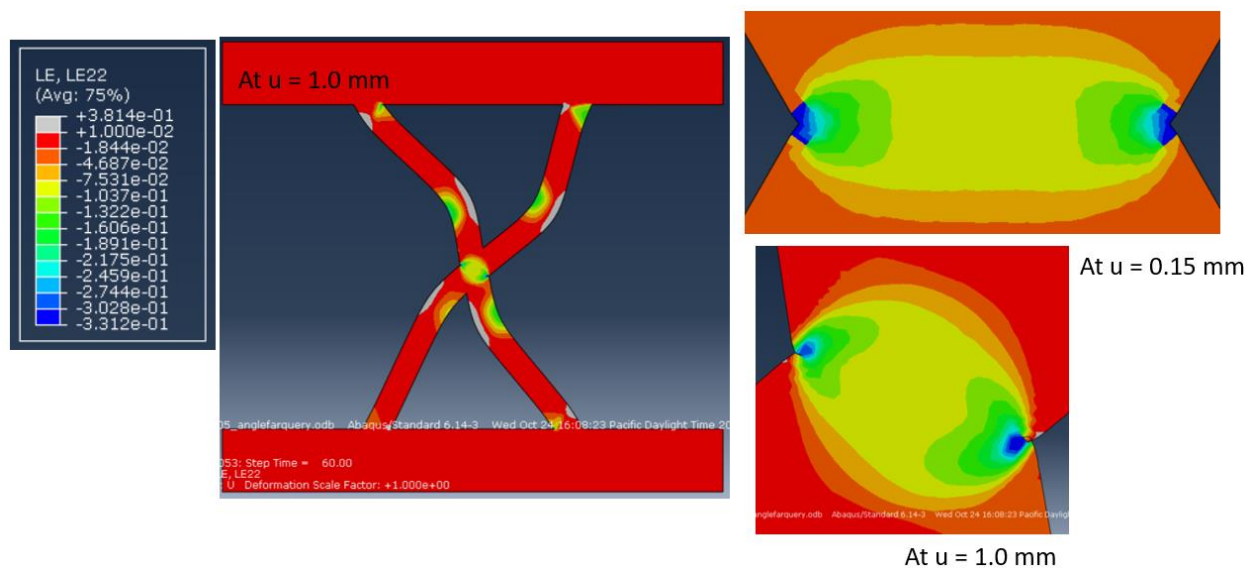


Figure 46. Full 2D FEA predictions of evolution of plastic zones at the ends of the struts and in the center node. Yielding of the node section controls the peak load in the structure. Note that the deformed shape is virtually identical to one of the images shown in Figure 10.

Figure 47 illustrates that the observed deformation mode is accurately predicted by the full 2D analysis; asymmetry is a consequence of slight mesh asymmetry that produces preferential yielding on one side that sets the subsequent deformation mode. The 2D FEA prediction is within 10-25% of the load for a given displacement, as seen in **Figure 48**. While closer agreement between 2D FEA and the experiments can likely be obtained by accounting for differences between nominal and as-printed geometry, the goal of this section was to establish techniques that avoid such calibrations due to the prohibitive expense of scaling 2D FEA into 3D FEA for complex lattices. As such, the remainder of this section focuses on establishing effective beam-based approaches in capturing the 2D results: future work can then focus on calibrating the beam-based approach to account for printing-related artifacts.

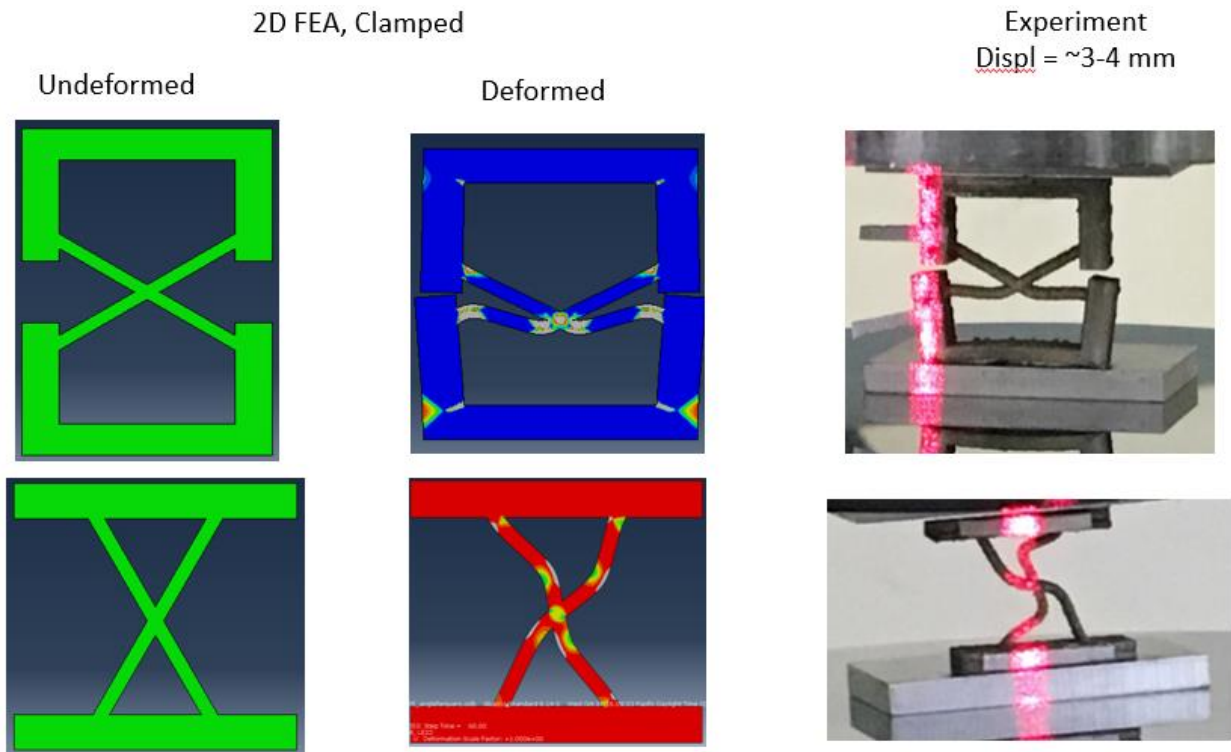


Figure 47. A comparison of the predicted deformed shape with plastic zones illustrated and the experiments on Node B, rotated configuration.

The central concept of the beam-based approach for nodes is shown in **Figure 49**. The material in the strut intersection (node) is modeled with a ‘box’ of four beam elements whose dimensions are adjusted such that the corners of the box intersect the strut axes. Asymmetry can be introduced by altering the dimensions of beam elements on either side of the box; e.g., a smaller box element on the left of the box will cause earlier yielding on that side.

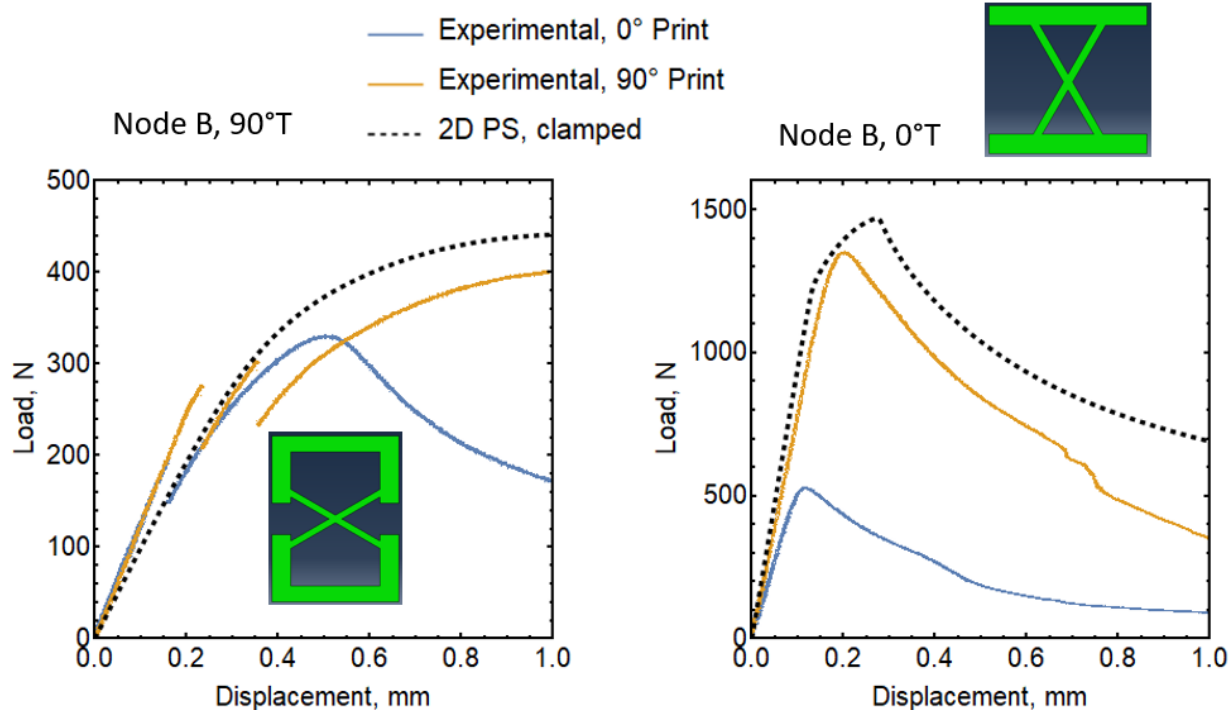


Figure 48. A comparison of the predicted load-compression curve from full 2D FEA (using nominal dimensions) and the corresponding experiments.

Figure 50 shows a comparison of the compressive response of the beam-box approach and the fully resolved 2D FEA of the nodal section. A comparison of the two dashed curves – the 2D FEA and the 'perfect' beam box (with nominal dimensions, complete symmetry and hardening behavior identical the 2D case) shows that the beam-box approach overestimates the peak load of the structure and underestimates the resistance to deformation after peak load is reached. Perfectly symmetric beam-boxes also fail to capture the deformation asymmetry seen in 2D FEA and experiments. As shown in **Figure 50**, defining asymmetric sides of the beam box leads to a significant decrease in stiffness at the onset of yielding, which persists to large compressive deformation and fails to capture the peak observed in 2D FEA and experiments. That is, displacements associated with peak load are much larger for beam-box simulations that use hardening descriptions identical to that in the 2D FEA.

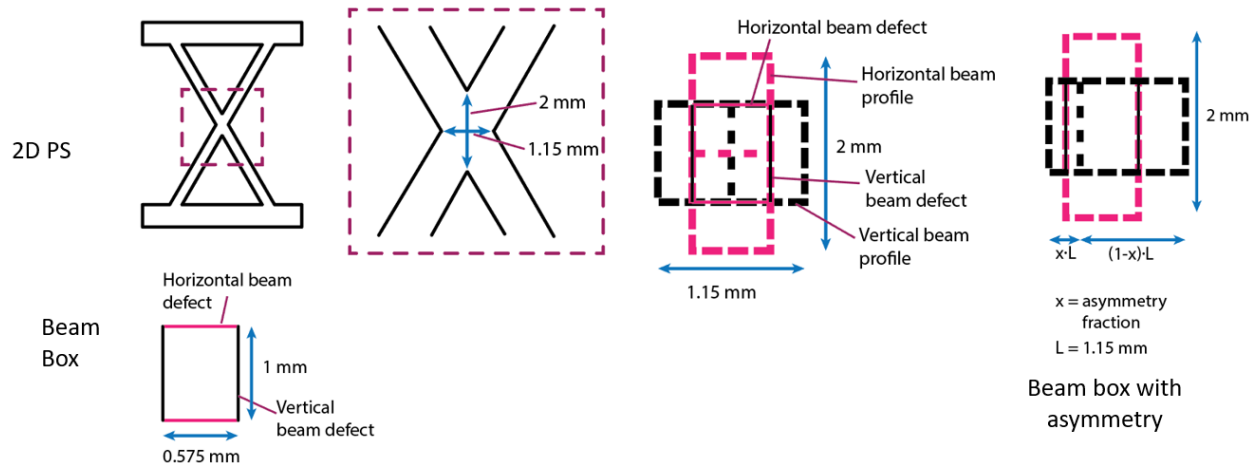


Figure 49. *The beam box concept for modeling nodes, wherein additional beam elements with dimensions that match the node are added to the connections between the strut elements. The dimensions of the beam box elements (representing the node) can be defined with asymmetry, which leads to strut rotations such as those shown in Figure 10.*

It was hypothesized that the beam-box approach fails to capture enhanced strain hardening (SH) that occurs in 2D FEA, as a result of the strain concentration arising from the strut intersections. To test this hypothesis, simulations were run with an enhanced level of strain hardening in the beam box elements; the effects of various levels of enhanced hardening (i.e. a higher slope in the hardening portion of the bilinear stress-strain curve) are shown in **Figure 50**. The results clearly demonstrate that increasing the level of hardening in beam-box and including 5-10% asymmetry more effectively match the predictions of 2D FEA.

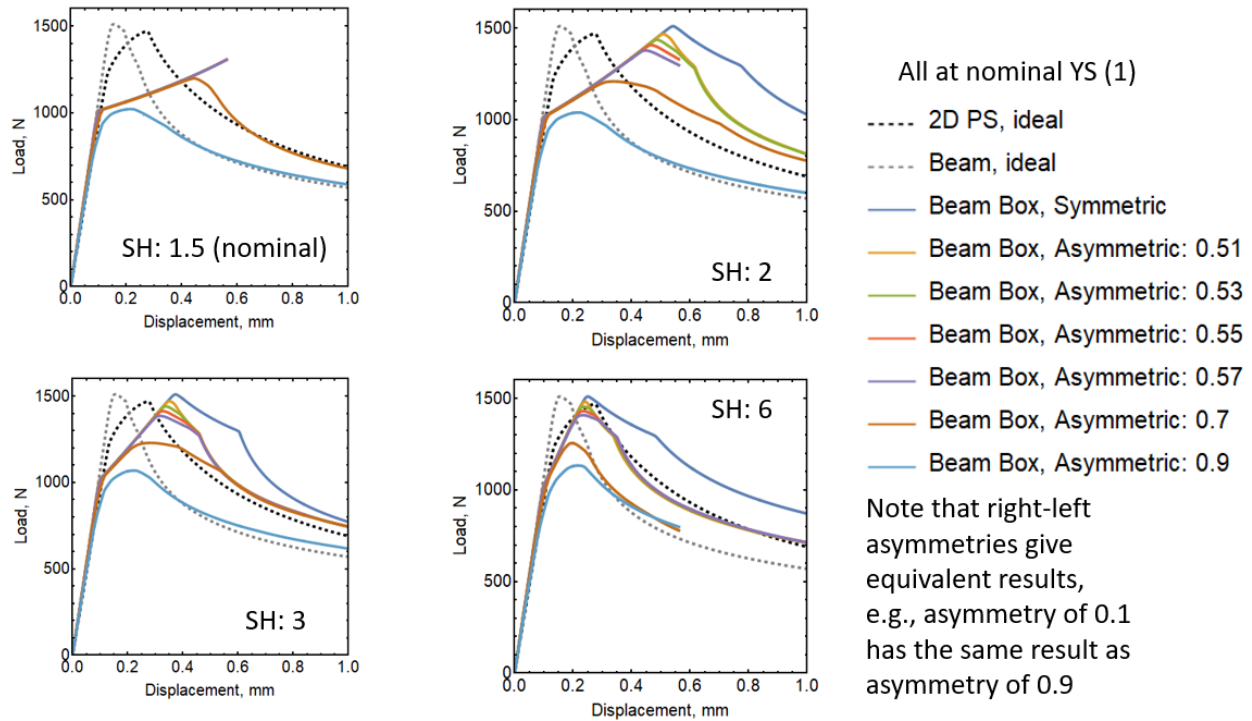


Figure 50. A comparison of beam box simulations (to capture nodal deformation) with full 2D FEA, showing the effect of asymmetry and elevated strain hardening (SH) in the beam elements used to represent the node. The elevated strain hardening is motivated by the fact that the node sees elevated strain hardening due to a strain concentration, which cannot be captured by the beam elements with one-dimensional geometry.

These results strongly suggest that the beam-box approach can be calibrated to yield consistent response to fully resolved 2D FEA. A theoretical approach to calibrating the beam box is shown in **Figure 51**. In this approach, the hardening level of the beam-box is adjusted such that the stress-elevation seen in the 2D FEA is matched at equivalent levels of strain. That is, the level of stress-elevation required in the beam-box method is identified as the stress jump produced in the 2D FEA. Using the observed strain in the beam-box, the hardening is adjusted until this beam-box strain produces the same stress jump as estimated from the peak equivalent plastic strain observed in the 2D FEA. **Figure 52** shows a comparison of ‘best fit’ of the beam box model to the 2D FEA, wherein the level of beam-box hardening is manually adjusted to maximize agreement between the two predictions. Also shown are the results of the calibration procedure based on strain concentrations estimated from the 2D FEA. The required degree of strain hardening in the beam-box, from both the theoretical estimate and ‘best fits’ is in the range of 3-4, which is in reasonable agreement with plastic strain concentrations for rounded notches.

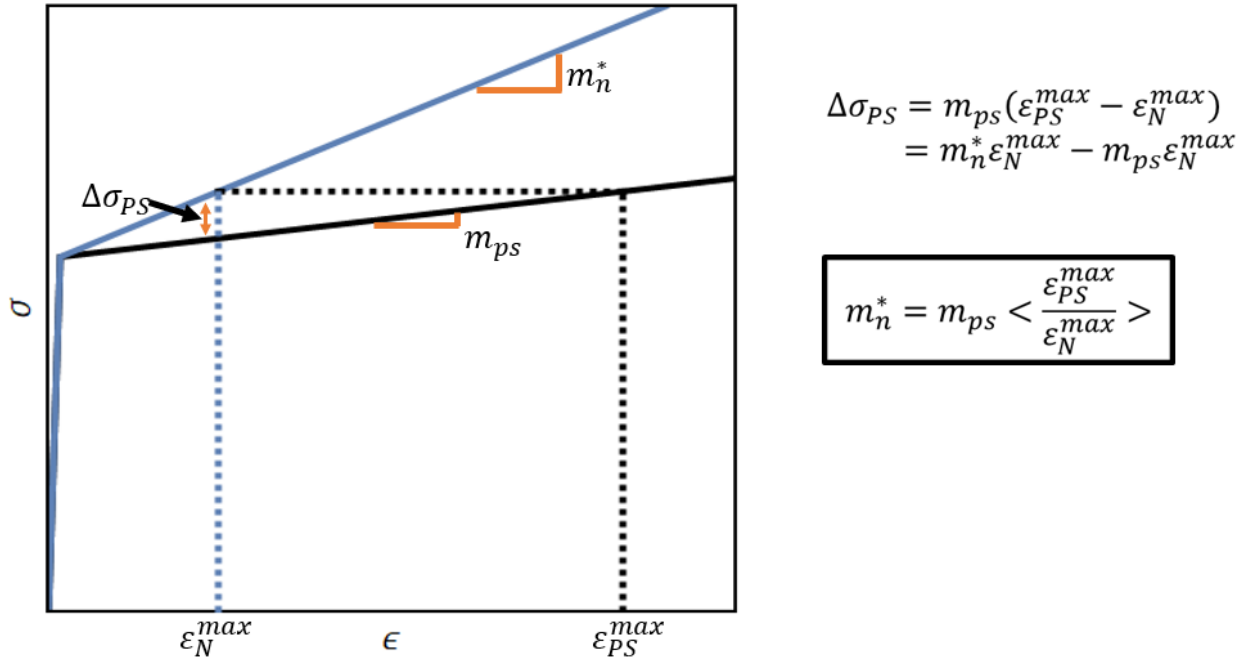


Figure 51. Conceptual diagram motivating the calibration used to specify strain hardening in beam box elements; the full 2D plane stress calculation is used to estimate the maximum strain in the nodes (due to the strain concentration); elevated hardening is prescribed in the beam box that will produce the same stress elevation at the strain level observed in the beam box.

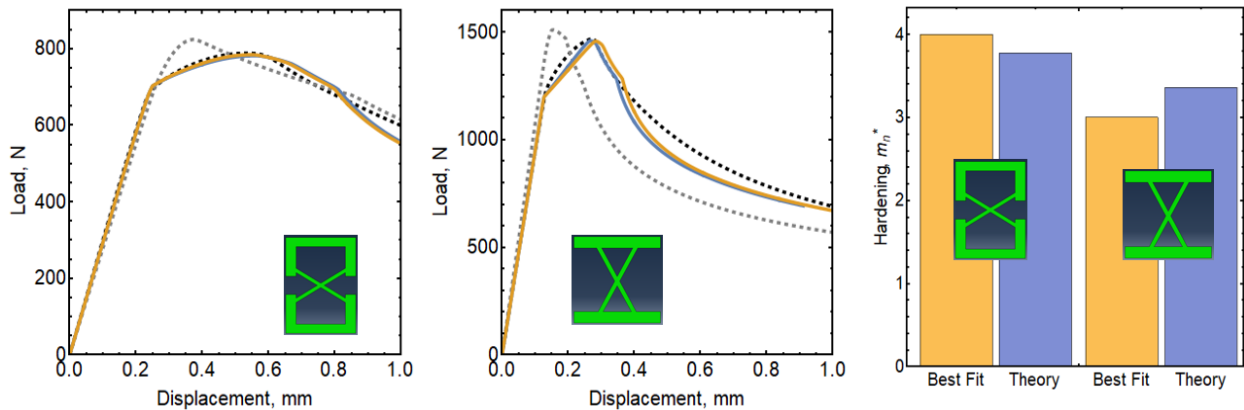


Figure 52. A comparison of “best fit” between the beam box concept and full 2D FEA, wherein the hardening properties of the beam box elements are adjusted to maximize agreement; the black dashed line indicates the 2D FEA result while the grey dashed line shows the result of beam box with no adjustments. The yellow line is the best fit, while the blue line uses the calibration concept described in the text.

While more sophisticated calibrations are obviously possible – e.g. those based on specific strain components within the node and/or stress/strain distributions through cuts in the notch – the use of maximum effective plastic strain is likely sufficient as it captures the dominant plastic strain

component in the node. The dominant strain component depends on strut orientation; strut orientation dictates the resolution of axial strut forces into components at the node.

This is supported by additional calculations for nodes formed by struts at different angles, as shown in **Figure 53**. Beam box calibration involves comparing the max PEEQ and SMISES corresponding to that max PEEQ of an uncalibrated beam box (beam box model with nominal strut diameter and node box area) to that of its corresponding 2D PS simulation. The hardening in the node of the beam box is then adjusted using the calibration scheme illustrated in **Figure 51** and the strut length is adjusted to match the modulus of the 2D PS simulation; the node box area can be adjusted to match the peak stress of the 2D PS simulation. For each case in Figure 53, the hardening adjustment, a single value of increased hardening in the node is applicable across many strut angles. Suitable length adjustments correspond to inscribing the beam box inside the node according to strut angle.

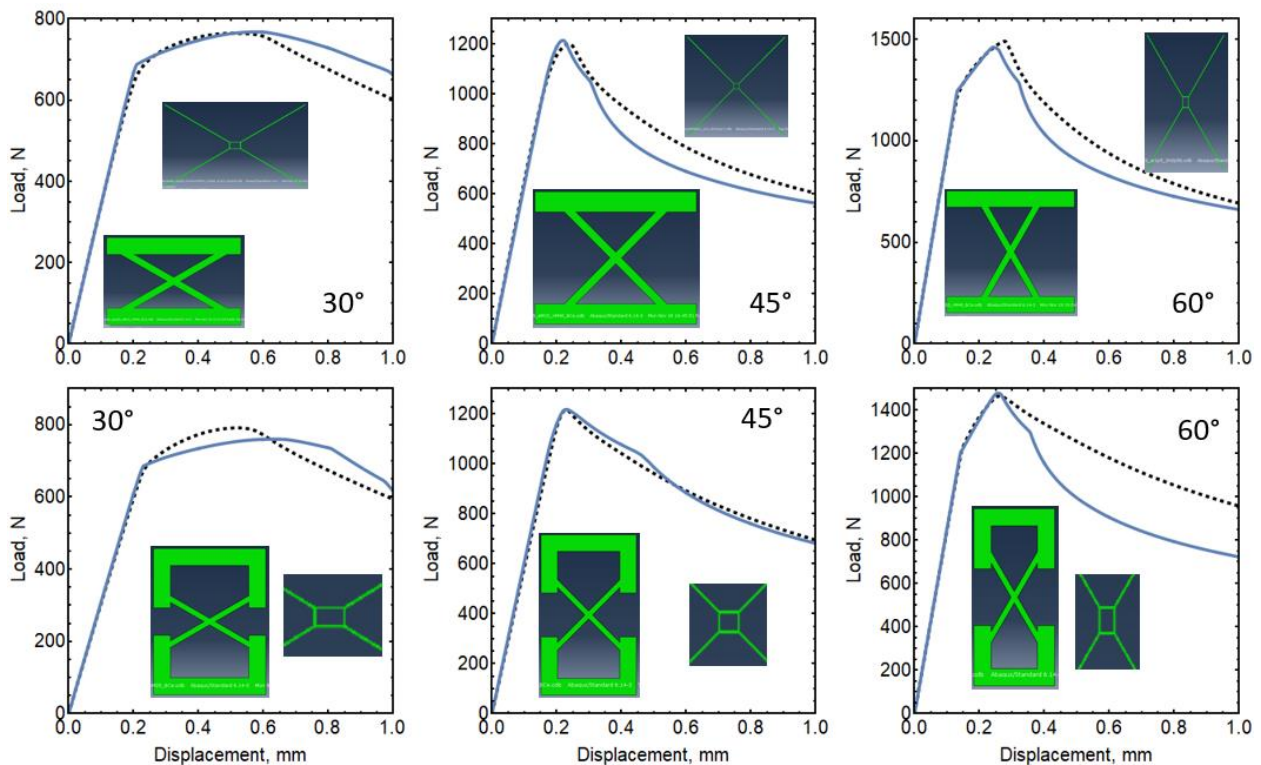


Figure 53. A comparison of calibrated beam box predictions and full 2D FEA for nodes with different strut angles and different boundary conditions; the calibration is the theoretical calibration developed from the 60 degree nodes.

The node with the largest angle with side constraints shows the most significant discrepancy beyond peak load. This is likely a result of additional hardening at the remote ends of the struts, where they connect to the frame. The simulations reveal that significant plastic zones develop at these locations in both 2D FEA and the beam-based models. However, the beam simulation does not include any additional hardening effects at these locations, where the strut forms a sharp angle with the surrounding frame. It is hypothesized that agreement could be improved by

include a beam-box node model at these locations with an increased level of hardening that would inhibit plastic collapse at the remote ends of the struts.

9.4 Key Outcomes

- The spread of plastic zones near strut intersections strongly impacts the global load displacement response of the structure. In essence, the peak load of the structure is determined by the instance in which the spread of plasticity across the node becomes fully established.
- Once sufficient straining has taken place in the nodes, the plastic zones in the strut themselves take over and govern the post-buckling collapse of the structure. Strain hardening plays an important role in this transition, as it governs the level of deformation needed to drive plastic zones from the nodes to the struts.
- The use of beam boxes to approximate yielding behavior in the nodes is quite promising, as it does a reasonable job of estimating response regardless of intersection angle. The calibration of these boxes appears relatively insensitive to the node geometry, strongly suggesting that a single calibration (i.e. enhanced hardening of 3-4) can be used irrespective of the nodal geometry.
- Naturally, the quality of the simulation also depends strongly on boundary conditions; it is likely that all strut connections require beam boxes to accurately capture the spread of plasticity in those locations.

10.COMBINED NODE AND DEFECT SIMULATIONS

10.1 Overview

This section describes FEA analyses of a simple structure consisting of multiple nodes (strut intersections), as well as strut surface defects such as those considered in Section 7. The motivation of this study was to determine whether the beam-box approach accurately captures response when multiple nodes are present, and, whether combining beam-boxes and defect elements can capture the combined effects of nodal plasticity and surface strut defects.

10.2 Methods

As in Sections 7 and 8, the simple structure shown in **Figure 54** was modeled with fully resolved 2D FEA subject to plane stress, and compared to simulations using the beam-box approach described in Section 8. For these preliminary calculations, enhanced strain hardening was not included in the nodes; this is the focus of on-going work to validate the calibration procedure used earlier. Simulations were run for cases summarized in **Figure 54**, spanning nominally perfect structures and those with defects.

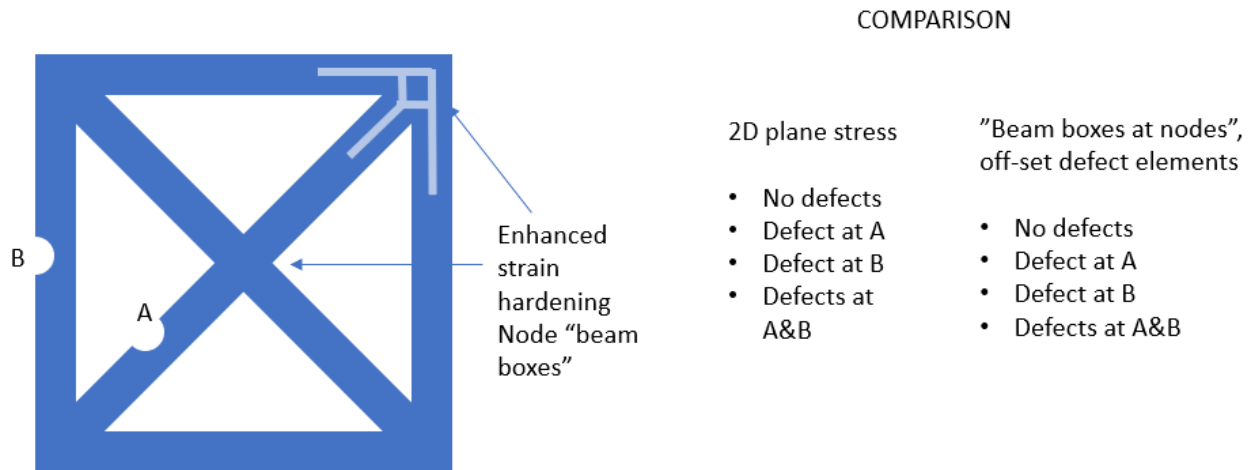


Figure 54. A comparison of full 2D FEA simulations and beam element simulations, with edge defects (at 30% depth) in the struts placed at position A and/or B. These simulations demonstrate that strut defects without plasticity in the nodes (i.e. no nodal beam box) does not produce accurate results.

10.3 Results & Discussion

Figure 55 shows the responses of the nominal structure, and those with a single strut defect at location A. It can be seen that the lack of enhanced hardening in the beam boxes leads to low predictions of post-peak strength, as expected. The peak load on the structure and behavior up to ~2% nominal strain is accurately captured.

As indicated on the right in **Figure 55**, the presence of a single defect in one of the center struts leads to softer response after peak load; interestingly the presence of this defect diminishes the importance of strain hardening in the center node. The beam box approach, combined with a strut defect element, does an excellent job of predicting the impact of a strut defect. Note that there is strong agreement between the fully resolved FEA and beam-based approach with respect to the extent of plastic zones throughout the structure.

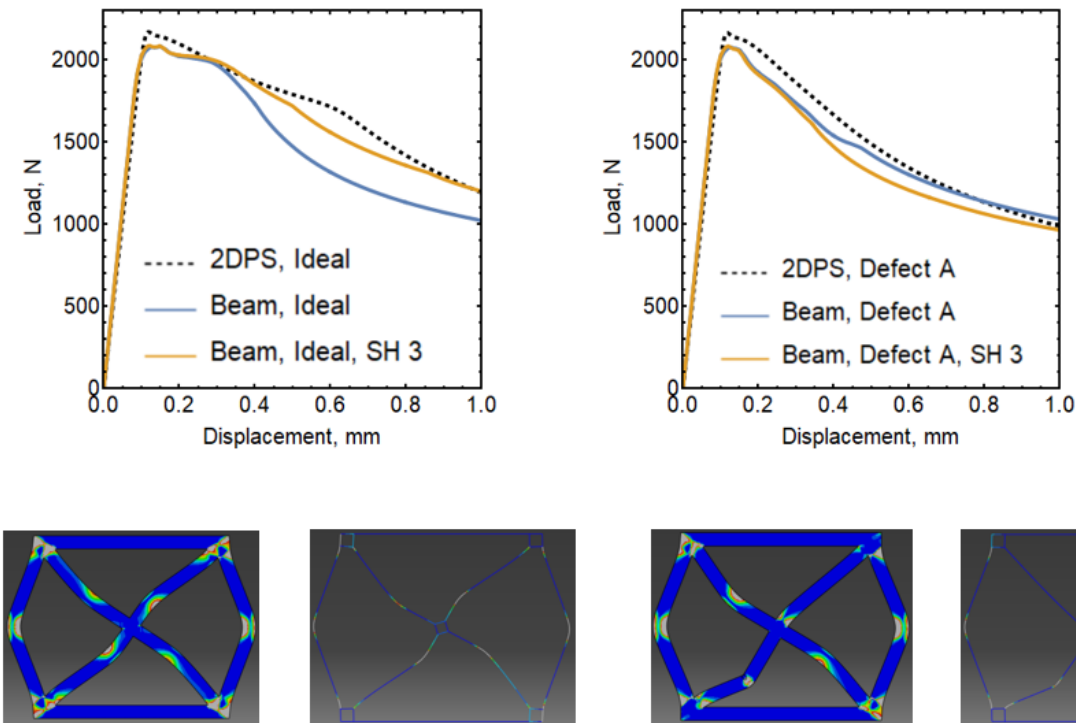


Figure 55. A comparison of full 2D plane stress FEA simulations and beam element simulations, for a defect at position A.

Figure 56 shows that the location of the defect has a moderate impact on the post-peak response; interestingly, a defect in the outer strut (aligned with the loading direction) shows smaller post-peak softening. The prediction of the beam-box model with a strut defect element is slightly poorer than a defect in the center strut, but still shows reasonable agreement. The impact of two defects is also shown in **Figure 56**; a comparison of the Defect A and Defect A&B cases shows that the defect in the center strut dominates the post-peak performance of the structure.

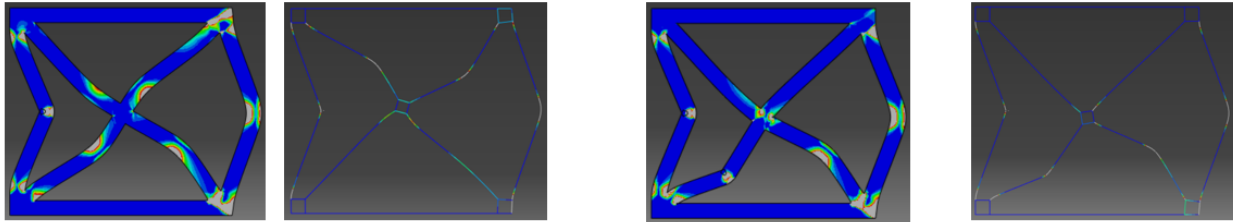
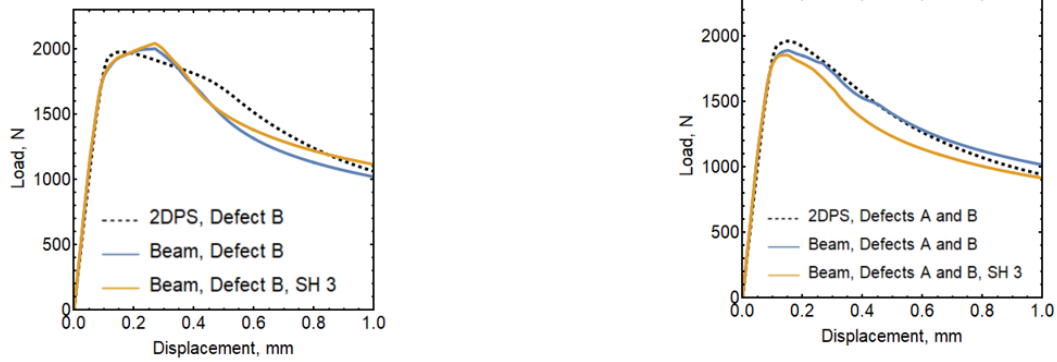


Figure 56. A comparison of full 2D plane stress FEA simulations and beam element simulations, with numerous edge defects placed at positions A and B.

10.4 Key Outcomes

- The agreement between beam-box models, with and without strut defects, and fully resolved FEA strongly suggests the approach will be effective in more complicated structures involving multiple nodes and multiple printing defects.
- While this study is only preliminary, future work will include extending the method to three dimensional lattices and verifying the approach works with non-planar nodes. This set of calculations will include a defect sensitivity study to identify defect locations that most strongly impact the response of the lattice.

11.SUMMARY AND FUTURE WORK

11.1 Summary

- Significant differences exist between nominal and as-printed geometry, at least for strut sizes at the lower limit of printing resolution (where AM lattices will exhibit their largest benefit, i.e. at low relative density). Significant surface defects exist both within struts and near/within nodes, but HIP'ing eliminates interior defects.
- Geometric differences are likely insufficient to explain orientation-dependence in struts. Orientation-specific microstructures are likely a factor, but more detailed characterization is needed to quantify their impact. Regardless, given the significant impact of geometry differences and defect structures, the effect of microstructure cannot be addressed until geometric factors have been quantified.
- Putting defects aside, beam-based models fail to capture plasticity at strut intersections, which has a profound influence on global response; capturing the spread of plasticity that initiates within nodes is critical to getting accurate responses, even in the absence of defects.
- Once nodal behavior is understood and can be simulated accurately, the impact of surface defects can be quantified by combining both in a single simulation. The coupling between nodal plasticity and surface defects likely plays a critical role in the behavior of lattices near peak loads.
- Beam-based defect elements which simulate the impact of net-section reductions and eccentricity associated with surface strut defects are effective in capturing changes in strut response due to the presence of a defect. Defect elements should be on the dimension of the defect size (due to the localized plasticity near the defect) and be used with rigid links to adjacent, intact elements to account for axial eccentricity introduced by the defect.
- The spread of plastic zones within strut intersections can be accurately captured with beam-box models, which incorporate beam elements forming a box within the node. The elements of the beam box yield in response to the forces directed to the node from the struts, with the sides of the box experiencing the greatest force yielding first. A comparison of 2D FEA and beam-box models shows good agreement across a range of strut intersection geometry and loading conditions.
- Elevated strain hardening in the nodes plays a critical role in controlling the transition from node yielding to strut collapse; this strain hardening likely results from the strain concentration of the strut intersection geometry. Accurate responses, as compared to full 2D FEA, can be obtained by calibrating the beam-box elements to have equivalent levels of stress elevation for the strain level seen in each approach. This enhanced strain hardening is typically 3-4 times that used in the strut elements (or 2D FEA), which is consistent with the level of plastic strain concentrations seen at rounded notches.

- Simulations that combine beam-box models for strut intersections, and beam-defect elements for surface strut defects, provide reasonably accurate predictions for global response. This validation provides strong evidence that an efficient low-order model of lattice response can be generated that quantifies the impact of defect location in lattices.

11.2 Future Work

Additional characterization of material structure is needed to quantify the impact of differences associated with both strut size and strut orientation. In order to isolate material effects from structural effects (such as those focused on here), primitives should be printed under a variety of build themes known to alter material structure. This characterization should include both experimental studies of grain structure, orientation and composition, as well as single crystal plasticity models of grain structures to determine their aggregate effect on strut behavior.

12. REFERENCES

- [1] Murr, L. E., Amato, K. N., Li, S. J., Tian, Y. X., Cheng, X. Y., Gaytan, S. M., ... & Wicker, R. B. (2011). Microstructure and mechanical properties of open-cellular biomaterials prototypes for total knee replacement implants fabricated by electron beam melting. *Journal of the mechanical behavior of biomedical materials*, 4(7), 1396-1411.
- [2] Li, S. J., Xu, Q. S., Wang, Z., Hou, W. T., Hao, Y. L., Yang, R., & Murr, L. E. (2014). Influence of cell shape on mechanical properties of Ti-6Al-4V meshes fabricated by electron beam melting method. *Acta biomaterialia*, 10(10), 4537-4547.
- [3] Li, S. J., Murr, L. E., Cheng, X. Y., Zhang, Z. B., Hao, Y. L., Yang, R., ... & Wicker, R. B. (2012). Compression fatigue behavior of Ti-6Al-4V mesh arrays fabricated by electron beam melting. *Acta Materialia*, 60(3), 793-802.
- [4] Gibson, L. J., & Ashby, M. F. (1999). *Cellular solids: structure and properties*. Cambridge University Press.
- [5] A.A. Antonysamy, J. Meyer, P.B. Prangnell, Effect of build geometry on the β -grain structure and texture in additive manufacture of Ti6Al4V by selective electron beam melting. *Mater. Charact.*, 84 (2013), 153168.
- [6] Dehoff, R. R., Kirka, M. M., Sames, W. J., Bilheux, H., Tremsin, A. S., Lowe, L. E., & Babu, S. S. (2015). Site specific control of crystallographic grain orientation through electron beam additive manufacturing. *Materials Science and Technology*, 31(8), 931-938.
- [7] L.E. Murr, E.V. Esquivel, S.A. Quinones, S.M. Gaytan, M.I. Lopez, E.Y. Martinez, F. Medina, D.H. Hernandez, E. Martinez, J.L. Martinez, S.W. Stafford, D.K. Brown, T. Hoppe, W. Meyers, U. Lindhe, R.B. Wicker, Microstructures and mechanical properties of electron beam-rapid manufactured Ti-6Al-4V biomedical prototypes compared to wrought Ti-6Al-4V. *Mater. Charact.*, 60 (2009), 96105.
- [8] L. Facchini, E. Magalini, P. Robotti, A. Molinari, Microstructure and mechanical properties of Ti-6Al-4V produced by electron beam melting of pre-alloyed powders. *Rapid Prototyp. J.*, 15 (2009), 171178. <https://doi.org/10.1108/13552540910960262>
- [9] R. Boyer, E.W. Collings G. Welsch, *Materials Properties Handbook: Titanium Alloys*. ASM International: Materials Park, OH (1994).
- [10] S. Zhao, S.J. Li, W.T. Hou, Y.L. Hao, R. Yang, R.D.K. Misra, The influence of cell morphology on the compressive fatigue behavior of Ti-6Al-4V meshes fabricated by electron beam melting. *J. Mech. Behav. Biomed. Mater.*, 59 (2016), 251264.
- [11] H.K. Rafi, N.V. Karthik, H. Gong, T.L. Starr, B.E. Stucker, Microstructures and mechanical properties of Ti6Al4V parts fabricated by selective laser melting and electron beam melting. *J. Mater. Eng. Perform.*, 22 (2013), 38723883.

- [12] C. de Formanoir, S. Michotte, O. Rigo, L. Germain, S. Godet. Electron beam melted Ti-6Al-4V: Microstructure, texture and mechanical behavior of the as-built and heat-treated material. *Mater. Sci. Eng. A*, 652 (2016), 105119.
- [13] M. Suard, G. Martin, P. Lhuissier, R. Dendievel, F. Vignat, J.J. Blandin, F. Villeneuve, Mechanical equivalent diameter of single struts for the stiffness prediction of lattice structures produced by Electron Beam Melting. *Additive Manufacturing*, 8 (2015), 124–131. <https://doi.org/10.1016/j.addma.2015.10.002>
- [14] A. Perez-Sanchez, A. Y'anez, A. Cuadrado, O. Martel, N. Nuo, Fatigue behaviour and equivalent diameter of single Ti-6Al-4V struts fabricated by Electron Beam Melting orientated to porous lattice structures. *Mater. Des.*, 155 (2018), 106-115. <https://doi.org/10.1016/j.matdes.2018.05.066>
- [15] O. Cansizoglu, O. Harrysson, D. Cormier, H. West, T. Mahale, Properties of Ti-6Al-4V non-stochastic lattice structures fabricated via electron beam melting. *Mater. Sci. Eng. A*, 492 (2008), 468-474. <https://doi.org/10.1016/j.msea.2008.04.002>
- [16] C.J. Smith, F. Derguti, E. Hernandez Nava, M. Thomas, S. Tammam-Williams, S. Gulizia, D. Fraser, I. Todd, Dimensional accuracy of Electron Beam Melting (EBM) additive manufacture with regard to weight optimized truss structures. *J. Mater. Process. Technol.*, 229 (2016), 128138.

LIST OF SYMBOLS, ABBREVIATIONS, AND ACRONYMS

2D	Two-dimensional
3D	Three-dimensional
AFRL	Air Force Research Laboratory
CAD	Computer-Aided Design
CT	Computed Tomography
EBM	Electron Beam Melting
EBS	Electron Backscatter Diffraction
EDM	Electrical Discharge Machining
FEA	Finite Element Analysis
HIP	Hot Isostatically Pressed
ICME	Integrated Computational Materials Engineering
RX	Material and Manufacturing Directorate
RXCM	Materials Branch, Structural Materials Division, Materials and Manufacturing Directorate
UCSB	University of California, Santa Barbara
UTS	Ultimate Tensile Strengths
WPAFB	Wright-Patterson Air Force Base